Ternary Lithium Based Compounds used for Technological Applications

Dissertation
zur Erlangung des Grades
"Doktor der Naturwissenschaften"
am Fachbereich Chemie, Pharmazie und Geowissenschaften
der Johannes Gutenberg-Universität Mainz

vorgelegt von
Andreea Beleanu
geboren in Medias (Rumänien)

Mainz, 2014

Dekan:

1. Berichterstatter:
2. Berichterstatter:

Tag der mündlichen Prüfung:

Die vorliegende Arbeit wurde in der Zeit von April 2008 bis April 2012 am Institut für Anorganische und Analytische Chemie in Fachbereich Chemie, Pharmazie und Geowissenschaften der Johannes Gutenberg-Universität, Mainz und von April 2012 bis Mai 2014 am Max-Planck-Institut für Chemische Physik fester Stoffe unter der Leitung von angefertigt.

Mainz, Juli 2014

Hiermit versichere ich, dass ich die vorliegende Dissertation selbständig verfasst und keine anderen als die angegeben Hilfsmittel benutzt habe. Alle der Literatur entnommenen Stellen sind als solche gekennzeichnet.

Mainz, Juli 2014

Contents

1 Zusammenfassung

Im Rahmen dieser Dissertation wurden ternäre Li-haltige Halb-Heusler Verbindungen sowie dazu strukturell-verwandte Verbindungen untersucht. Diese Verbindungen sind potentielle Kandidaten für optoelektronische und spintronische Anwendungen. Einige der untersuchten Verbindungen sind auch als Elektroden Materialien in Li-Batterien geeignet. Neben der Synthese und der Untersuchung der chemischen Eigenschaften wurden daher insbesondere die physikalischen Eigenschaften näher untersucht. Im speziellen wurden Halb-Heusler Verbindungen wie LiMgZ (Z = P, As, Sb) und LiZn$_{1-x}$Mn$_x$P synthetisiert und charakterisiert. Des Weiteren wurden die Verbindungen LiMnAs, LaOMnAs und LiCuS näher studiert.

Verbindungen des Typs LiMgZ (Z = P, As, Sb) sind potentielle Anode-Materialien in Li-Batterien. Im Rahmen der Arbeit gelang es diese Verbindungen einphasig zu synthetisieren. Mit Hilfe der UV-VIS Spektroskopie wurden Bandlücken im Bereich von 0.9 und 2.3 eV bestimmt. ^{7}Li NMR Spektroskopie zeigte eine ausreichende Li Mobilität, die sich mit steigender Temperatur erhöht.

Weiterhin wurde die Mischkristallserie LiZn$_{1-x}$Mn$_x$P mit x = 0.04, 0.08 und 0.10 untersucht. Ziel dieser Arbeit war es aus dem Halbleiter LiZnP durch Dotierung einen verdünnten magnetischen Halbleiter herzustellen. Diese Materialien werden insbesondere in der Spintronik benötigt. Optische Messungen zeigten, dass die Dotierung bis x = 0.10 zu einer Reduzierung der Bandlücke von 1.80 eV für LiZnP zu 1.18 eV für LiZn$_{0.90}$Mn$_{0.10}$P führt. Magnetische Untersuchungen erwiesen paramagnetisches Curie-Weiss Verhalten und negative Weiss Konstanten, die auf eine antiferromagnetische Ordnung bei tiefen Temperaturen hindeuten.

LiMnAs und LaOMnAs sind beides antiferromagnetische Halbleiter, die insbesondere für spinelektronische Anwendungen von Bedeutung sind. Die magnetische Struktur von LiMnAs wurde mit Hilfe der Neutronenbeugung näher untersucht. Die N$\acute{e}$el Temperatur wurde zu 374 K bestimmt. Bei einer Temperatur von T = 768 K kommt es zu einer Phasenumwandlung. Die tetragonale Struktur wandelt sich hier in einer kubischen Halb-Heusler Phase um. Dichte Funktional Rechnungen sind in guter Übereinstimmung mit den experimentellen Werten. Darüberhinaus wurde die Kopplung der magnetischen Momente näher bestimmt.

Eine Verbindung der Zusammensetzung LiCuS wurde in der Literatur beschrieben als eine Phase, die sich bei der Reaktion von Li mit CuS in Li/CuS Batteriesystem bildet. Diese Verbindung ist auch als Ersatz von CdS in Pufferschicht von Dünnfilm-Solarzellen von Interesse. Es gelang erstmals diese Verbindung einphasig herzustellen. Sie kristallisiert gelb mit der nicht-stöchiometrischen Zusammensetzung $Li_{1.1}Cu_{0.9}S$. Die Kristallstruktur wurde mit Hilfe von NMR, PXRD und Neutronenbeugung aufgeklärt. Die Bandlücke wurde aus den optischen Messungen von Dünnschichten bestimmt und beträgt circa 2 eV. Dieser Wert ist in guter Übereinstimmung mit DFT Ergebnissen. Wird der Li-Gehalt erhöht, erhält man ab circa $Li_{1.7}Cu_{0.3}S$ eine kubische Phase. Sie ist isotyp mit Li_2S, die im anti-CaF_2 Typ kristallisiert. Diese Verbindung ist ein direkter Halbleiter mit einer Bandlücke von 2.4 eV nach DFT Rechnungen.

2 Abstract

The aim of this thesis was twofold. Firstly to synthesize ternary Li-based Half-Heusler compounds and related materials, which are possible candidates for a wide range of technological applications. Secondly, to obtain knowledge about the chemical and physical properties of these compounds and to provide guidelines for their applications. In this doctoral thesis the synthesis and the results of the characterization methods are presented in form of a systematic investigations. The following materials have been studied: LiMgZ (Z = P, As, Sb), $\mathrm{LiZn}_{1-x}\mathrm{Mn}_x\mathrm{P}$, LiMnAs, LaOMnAs, and LiCuS.

A series of experimental investigations of the wide band gap compounds LiMgZ (Z = P, As, Sb) are reported in Chapter 6. The main objective was to study the ability of these compounds to serve as opto-electronics and anode materials for Lithium batteries. The polycrystalline samples were synthesized by reaction of the elements. LiMgZ (Z = P, As, Sb) crystallize in the cubic MgAgAs structure ($\mathrm{C1}_b$, space group $F\overline{4}3m$). X-ray measurements show homogeneous, single-phased samples. The neutron diffraction measurements show additional peaks suggesting a distortion of the structure due to the Li internal diffusion and mobility. The electronic properties were studied by resistivity measurements using the direct current (DC) method. Additionally UV-VIS diffuse reflectance spectra were recorded in order to investigate the band-gap nature. The measurements show that all compounds exhibit semiconducting behavior with direct band gaps of 1.0 eV to 2.3 eV depending on the Z element. A decrease of the peak widths in the static ^{7}Li nuclear magnetic resonance (NMR) spectra with increasing temperature was observed, which can directly be related to an increase of Li ion mobility.

In Chapter 7 the attention is turned towards the $\mathrm{LiZn}_{1-x}\mathrm{Mn}_x\mathrm{P}$ (x = 0.04, 0.08, 0.10) series. Compounds with x = 0, 0.04, 0.08, 0.10, 0.12, 0.35, were synthesized by reaction of the elements. Single phase samples were obtained for Mn contents less than x = 0.12. These compounds crystallize in the cubic $\mathrm{C1}_b$ Half-Heusler structure type and are predicted by theoretical calculations to behave like magnetically diluted semiconductors, materials which are suitable for spintronic applications.The Rietveld refinement on the powder XRD patterns exhibit that the Manganese atoms substitute the Zinc atoms by occupying the same Wyckhoff position, i.e., the 4a position with the coordinates (0,0,0). The main focus of this work was to study the influence of the crystal structure on the magnetic properties by this substitution. Optical measurements on $LiZn_{1-x}Mn_xP$ (x = 0.04, 0.08, 0.10) reveal a reduction of the band-gap from 1.80 eV for LiZnP to 1.18 eV for $LiZn_{0.90}Mn_{0.10}P$. The magnetic measurements performed for all studied samples of this class show a Curie Weiss paramagnetic behavior and negative Weiss constant.

For spintronic applications and spin valves antiferromagnetic semiconductors are new alternative materials. LiMnAs was proposed as a very suitable candidate due to its band gap and high magnetic moment per Mn atom. A detailed investigation of two antiferromagnetic semiconductors *A*MnAs (*A* = Li, LaO), which are isostructural to the well known LiFeAs and LaOFeAs superconductors is reported in Chapter 8. A comparison between the structural, magnetic, and electronic properties of LiMnAs, LaOMnAs, and related materials is elaborated. Interestingly, both LiMnAs and LaOMnAs show a variation in resistivity with more than five orders of magnitude, making them particularly suitable for use in future electronic devices. We found, in the case of LiMnAs, a variety of characterization methods exhibit a magnetic phase transition corresponding to an N*é*el temperature of 374 K and a structural transition from a tetragonal to the cubic phase at 768 K. The electronic and magnetic properties of both materials are discussed, as well as the transport properties. Ab-initio density functional theory calculations and the experimental results are combined in order to discuss the electronic and magnetic structure, commenting also on the non-Curie-Weiss-like behavior observed in LaOMnAs.

In Chapter 9 a new intermediate phase in the LiCuS system is reported, as a potential environment-friendly battery electrode and solar cell buffer layer in thin films. A yellow powder, $Li_{1.1}Cu_{0.9}S$, was obtained by the reaction of CuS with a slight excess of Li metal. The crystal structure of the single-phase polycrystalline sample was solved by a combination of neutron powder diffraction data at 4 and 293 K, X-ray diffraction data, and ^7Li solid-state NMR analysis. This compound crystallizes in a new structure type, with orthorhombic space group *Ibam* (No. 72). The orthorhombic lattice parameters are related to that of cubic Li_2S (anti-CaF_2 structure type) as follows: a_o, $c_o \approx a_c$, and $b_o \approx 2\ a_c$. An idealized crystal structure of $Li_{1.1}Cu_{0.9}S$ can be derived from the cubic Li_2S structure by moving a part of the Li chains along the *c* axis so that the Li atoms change their atomic environment from tetrahedral to linear coordination by S. All the metal sites are occupied by randomly mixed Li and Cu atoms; however, there is a strong preference for linear coordination by Cu. ^7Li solid state NMR measurements show two well-separated lines, indicating two different types of atomic environment for the Li atoms, similar with the results obtained by the Rietveld refinement. The Density functional theory calculations using the coherent potential approximation alloy theory show that $Li_{1.1}Cu_{0.9}S$ is a

direct band-gap semiconductor with an energy gap (at Γ point) of 1.95 eV, which is in very good agreement with the optical band gap measured for the radio-frequency sputter deposited LiCuS thin film [1], and the indirect energy gap in the vicinity of the R point is 2.55 eV.

The chemical reaction of Li_2S with Cu_2S has been used to study the phase stability of yellow $Li_{1.1}Cu_{0.9}S$. Mixtures withe the target composition of $Li_{2-x}Cu_xS$ (x = 0.1, 0.3, 0.5, 0.7, 0.9, 1) have been investigated using PXRD after heat treatment at 723 K for 96 h. The Rietveld refinement on the XRD patterns of $Li_{1.7}Cu_{0.3}S$ and $Li_{1.9}Cu_{0.1}S$ reveal a single homogenous phase. Both compounds crystallize in the cubic Half-Heusler structure type, space group $F\overline{4}3m$. From $Li_{1.1}Cu_{0.9}S$ to $Li_{1.7}Cu_{0.3}S$ all the measured XRD patterns reveal a mixture of the cubic phase (anti-CaF_2 structure type), the orthorhombic $Li_{1.1}Cu_{0.9}S$ (space group *Ibam*, No. 72) and a new unknown phase. The theoretical calculations reveal that $Li_{1.7}Cu_{0.3}S$ and $Li_{1.9}Cu_{0.1}S$ are both direct band-gap semiconductors with energies band-gap of 2.4 and 3 eV, respectively.

3 List of publications

1. J. Barth, G. H. Fecher, M. Schwind, A. Beleanu, C. Felser, A. Shkabko, A. Weidenkaff, J. Hanss, A. Reller, and M. Köhne
   Investigation of the thermoelectric properties of LiAlSi and LiAlGe
   J. Electronic Materials, 39, 9 **(2010)**, 1856
2. Patent DE102010004359 , D. Kieven, R. Klenk, C. Felser, T. Gruhn, C. Ludwig, S. Naghavi, A. Beleanu and A. Reller
   Optoelektronisches Funktionsmaterial, seine Herstellung und Verwendung,
   veröffentlicht am 14.07.2011

3. D. Kieven, A. Grimm, A. Beleanu, C.G.F. Blum, J. Schmidt, T. Rissom, I. Lauermann, T. Gruhn, C. Felser, R. Klenk
   Preparation and properties of RF-sputtered half-Heusler films with regard to usage in solar cell devices
   Thin Solid Films, 519, 6 **(2011)**, 1866
4. A. Beleanu, M. Mondeshki, Q. Juan, F. Casper, F. Porcher and C. Felser
   Systematical, experimental investigation on LiMgZ (Z = P, As, Sb) wide band gaps semiconductors
   J. Phys. D: Appl. Phys, 44, 47 **(2011)**, 475302
5. A. Beleanu, J. Kiss, G. Kreiner, C. Köhler, L. Müchler, W. Schnelle, U. Burkhardt, S. Chadov, S. Medvediev, D. Ebke, G. Cordier, B. Albert, A. Hoser, F. Bernardi, T. I. Larkin, D. Pröpper, A. V. Boris, B. Keimer and C. Felser
   Large resistivity change and phase transition in the antiferromagnetic semiconductors LiMnAs and LaOMnAs
   Phys. Rev. B, 88 **(2013)**, 475302
6. A. Beleanu, J. Kiss, M. Baenitz, M. Mayunder, A. Senyshyn, G. Kreiner and C. Felser
   LiCuS, an Intermediate Phase in the Electrochemical Conversion Reaction of CuS with Li
   in preparation

4 Introduction

4.1 Half-Heusler compounds

4.1.1 Crystal structure

Fritz Heusler discovered in 1903 a new intermetallic compound with the composition Cu_2MnAl [2, 3], which surprisingly behave like a ferromagnet although none of the constituent elements is ferromagnetic by itself. More than 1000 compounds have been found to crystallize isotypic with Cu_2MnAl so far. In addition a much smaller number of approximately 100 compounds crystallize closely related to Cu_2MnAl. This is the structure type of Li_2AgSb. In the cubic structure ($Fm\overline{3}m$) of Cu_2MnAl, Cu solely and the (Mn,Al) atoms form a NaCl-like partial structure, whereas in the crystal structure of Li_2AgSb ($F\overline{4}3m$) the majority element Li forms with Ag and with Sb NaCl-like partial structures. The structure type of Cu_2MnAl and Li_2AgSb are often called regular and inverse Heusler structure, respectively.

A closely related class of materials are Half-Heusler compounds. They have the general formula XYZ and can be considered as defect of the Heusler derivatives compounds with half of the X atoms replaced by vacancies. Half-Heusler compounds crystallize acentric in space group $F\overline{4}3m$, No. 216. The structure type is MgAgAs or $C1_b$ according to the Strukturberichte notation. The Half-Heusler structure is a ternary ordered variant of the CaF_2 crystal structure. Here, all F atoms are tetrahedrally coordinated by the Ca atoms and Ca atoms occupy centers of cubes with the F atoms at the vertices. In the Half-Heusler structure, half of the F atoms are replaced by a second type of metal atoms. The crystal structure can be described alternatively using three interpenetrating face-centered (fcc) sublattices of X, Y and Z atoms ($4a$ at 0,0,0; $4b$ at $\frac{1}{2}$,$\frac{1}{2}$,$\frac{1}{2}$ and $4c$ at $\frac{1}{4}$,$\frac{1}{4}$,$\frac{1}{4}$). This is shown in Figure 4.1.

Three different ordered variants are possible with respect to the general formula XYZ because the three components X, Y and Z form two different zinc-blende partial structures and one rock-salt partial structure. The first chemically different arrangement is obtained when the elements X and Y form a NaCl-like and XZ and YZ ZnS-like partial structures. The second one is obtained when XZ forms NaCl-

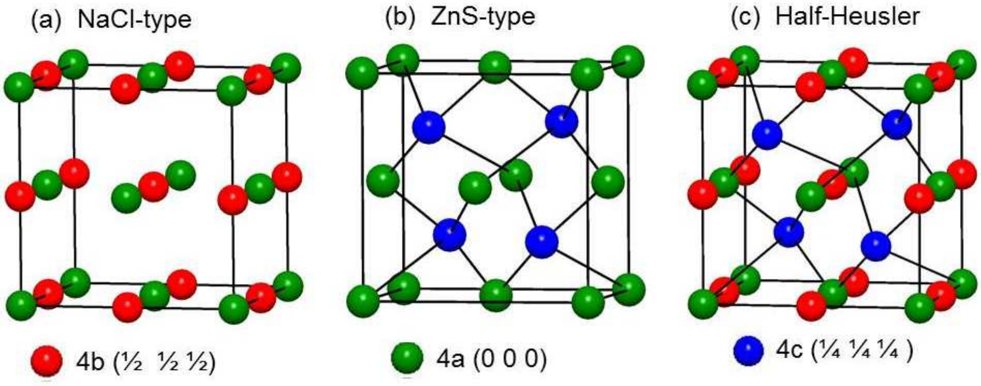

Figure 4.1: (a) The rock salt-type structure (b) the zinc blende-type structure and (c) Half-Heusler structure.

like and XY and YZ ZnS-like partial structures. Finally, YZ forms the NaCl-like and XY and XZ the ZnS-like partial structures. For instance, Mg and Ag form the NaCl-like and MgAs and AgAs the ZnS-like partial structures in the compound MgAgAs. The two other variants, i.e. with MgAs or AgAs partial rock-salt structure are unstable. In Table 4.1 some examples are listed.

Here, and in the following the electronegativity increases from X via Y to Z. The constituent Z is then always a main group element (e.g. Si, Ge, Sn, N, P, As, Sb, Bi). X and Y are often both alkali or alkali earth group metals (e.g. Li, Mg, Be). Sometimes Y is a transition metal (e.g. MgCuSb). However, more often X and Y are both transition metals (e.g. TiCoSb, YPdAs). A small number of compounds with rare-earth metals are also known.

An important subclass of the Half-Heusler compounds are semiconductors. The semiconducting compounds of MgAgAs type have always 8 or 18 valence electrons per formula unit. Especially, phases with $X^I Y^{II} Z^V$ with X^I = Li, Cu, Ag, Y^{II} = Be, Mg, Zn, Cd, and Z^V = N, P, As, Sb, Bi exhibit semiconducting behavior. These are known as Nowotny-Juza phases and are wide band gap semiconductors.

Recently, the chemical bonding situation of semiconducting Half-Heusler compounds have been studied to obtain a better understanding of the stability of the chemically three different arrangements [4]. For example, all semiconducting compounds with main group metals X and Y form XY NaCl-like partial structures. The most electronegative element Z occupies the center of the X_4Y_4 cube. This position is called the heterocubic site (HC). If X and Y are transition metals, then XZ forms the NaCl-like partial structure with Y at the heterocubic site. If X is a main group

Table 4.1: Examples of different Half-Heusler compounds. The respective NaCl-like and ZnS-like partial structures are given in column 5 and 6.

Compound	$4a$	$4b$	$4c$	NaCl-type	ZnS-type
MgAgAs	Mg	Ag	As	MgAg	AgAs, MgAs
LiMgP	Mg	Li	P	LiMg	MgP, LiP
TiCoSb	Ti	Sb	Co	TiSb	CoSb, TiCo
MgCuSb	Mg	Sb	Cu	MgSb	CuSb, MgCu

metal and Y is a transition metal, two possible arrangements have been observed experimentally. In case of MgAgAs, MgAg forms the NaCl-like partial structure with As at the heterocubic site. However, for MgCuSb, MgSb forms the NaCl-like partial structure with Cu at the heterocubic site. No structure variant with YZ forming the NaCl-like partial structure and the most electropositive element X at the heterocubic site is known so far.

It was shown in reference [4] that the arrangement with Y at the heterocubic site is determined by strong covalent interactions in the YZ ZnS-like partial structure. This bonding situation is mostly found in transition metals based semiconductors. In case of the main group metal based semiconductors ionic interaction stabilize the arrangement with the most electronegative element (Anion) at the heterocubic site.

4.1.2 Zintl concept

Zintl-phases are a special class of intermetallic compounds, which have been named after Edward Zintl to honor his pioneering work [5–7]. Classical Zintl phases contain an alkali or alkaline-earth metal and a p-block element, which is a metal, a semimetal or small-gap semiconductor [8]. The most important feature is that the electronic structure of a Zintl-phase can be described by chemical valence rules.

A typical example is the Zintl-phase NaTl, which crystallizes face-centered cubic with 16 atoms per unit cell (a = 7.469 Å [9]). Both Na and Tl atoms, respectively, form diamond type lattices. Na as a strong electropositive partner transfers electrons to the electronegative Tl. Thus NaTl can be described formally as $\mathrm{Na^{+}Tl^{-}}$. The $\mathrm{Tl^{-}}$ anion now forms a network, which is isostructural and isoelectronic with diamond. Each Tl atom in the $^{3}_{\infty}$[Tl] network is tetrahedrally coordinated by four Tl atoms at a distance of d(Tl–Tl) = 3.234 Å, i.e., forming 2c, 2e Tl–Tl bonds. The Na atoms have obtained by oxidation a close shell structure and the $[\mathrm{Tl^{-}}]$ polyanion is in agreement with the octet rule due to the reduction of Tl and by forming Tl–Tl

2c, 2e bonds. The small Na^+ cations are occupy voids in the Tl network and the Tl^- anions behave structurally similar to the isoelectronic element, which is found in the periodical table to his right. This rule was generalized and is now known as the Zintl-Klemm concept [10].

A large number of Zintl-phases have been discovered since the early work of Zintl. A book on Chemistry, Structure and Bonding of Zintl compounds have been edited by Kauzlarich in 1996 [11]. Review articles have been published by Jiang[12], by Jiang and Kauzlarich [13], Sevov [8], Miller [14] and Nesper [15].

The typical properties of Zintl-phases are [8]:

- air and moisture sensitive
- very narrow or no homogeneity range, usually they form point-like compounds
- are brittle
- are diamagnetic
- are semiconductors or poor conductors

Lithium based Zintl-phases form a special class of compounds. This is because lithium is the most electropositive element among the alkali metals. Lithium show a high electron affinity and polarizing power. In addition Li^+ is much smaller in size compared to its higher homologues. It is well known that lithium behaves similar in many compound classes to magnesium according to the diagonal relationship in the periodical table. However, Li and Mg based compounds behave usually different in Zintl compounds. An overview of Li-containing Zintl-phases is given in [15].

Examples of Li-based Zintl-phases are ternary pnictides of main groups metals of type LiMX, with M = Be, Mg, Ca, Sr and X = P, As, Sb, Bi. They are salt-like compounds $Li^+M^{2+}X^{3-}$ [15]. Ternary transition metal pnictides of the type LiTMX, with TM = Mn, Zn, Cu and X = P, As, Sb, Bi are also known. They crystallize with the structure type LiAlSi, LiMnP and LiGaGe. The distances TM–X in the corresponding framework are short. Therefore, the TMX partial structure is partially covalent bonded. Thus they can be described with the alternative notation $Li^+[TMX^-]$.

The crystal structure of LiZnP, which crystallizes in the LiAlSi (or MgAgAs, $C1_b$) structure type can be obtained from a hypothetical Zinc-blende (ZnP), structure by inserting Li atoms at interstitial sites in such a way that the Li and Zn atoms form a NaCl-like partial structure. In Figure 4.2 (a) and (b) a diagram is shown, which correlates the crystal structure and the valence electron distribution of GaAs

(ZnS-type) with that of LiMgP and LiZnP. All of them can be derived from the *fcc* structure.

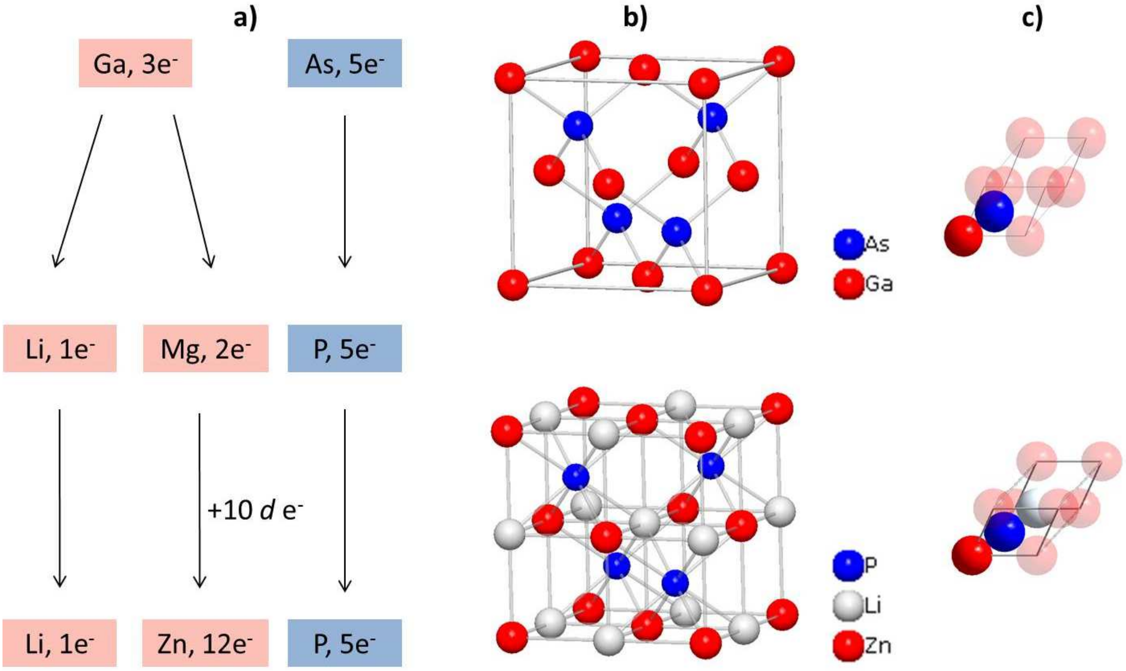

Figure 4.2: Zintl electron-couting concept in **(a)** from 8 VE (valence electrons) in GaAs to 8 VE in LiMgP and 18 VE in LiZnP. In **(b)** the transition from GaAs with Zinc-blende structure-type to LiZnP with $C1_b$ structure-type is shown, and in **(c)** the primitive cell of GaAs and LiZnP is displayed.

4.1.3 Properties and Applications

Most of the ternary Half-Heusler compounds with 8 and 18 electrons are semiconductors. Depending on the chosen anion or cation the properties of these compounds can be manipulated and adapted for the desired application.

Casper et al. [16] have shown in a detailed analysis, that for eight valence electron compounds, the gap size is larger for compounds with a large Pauli electronegativity difference of the anion and cation species [17]. It was also shown that the mechanism responsible for the band gap formation is the inter-site exchange interaction. The spin-orbit coupling splits the bands carrying the p symmetry into $p_{1/2}$ and $p_{3/2}$. It was observed that heavy constituents cause strong spin-orbit coupling within the valence and conduction bands, which in turn decrease the gap width.

For the lithium based semiconductors with low averaged atomic numbers Z the largest band-gaps are obtained. This makes them suitable for solar cell applications. By a higher Z the spin-orbit coupling becomes very strong, causing an interchange of the valence and conduction band symmetry characters. In heavy rare-earth Half-Heusler compounds (like LuPtBi, YbPtBi, LaAuPb, etc.) the strong spin-orbit coupling leads to a zero-gap system, thus they become topological insulators [16].

As mentioned above, one of the most popular uses of the ternary I-II-V semiconductors related to the II-VI compounds are in solar cells, serving as buffer layer in thin film solar cells and as potentially new light absorber layers. As an example, in the industrially mass-produced ternary Cu-based chalcopyrite semiconductors ($CuInS_2$, $CuInSe_2$, $CuGaSe_2$, etc.) a CdS buffer layer is used between the absorber material and the ZnO window layer in order to increase the performance of the device. But due to the toxicity of this buffer layer there is a strong interest in replacing CdS. For this particular purpose the I-II-V Half-Heusler compounds [18] are of special interest. They can be used as alternative buffer materials due to their related crystal structure and the feasible tunability of their band-gap. As a requirement, the band gap of the buffer materials should not be smaller than 2.0 eV and the lattice parameter of the crystal structure should be approximately 5.9 Å, in order to match the lattice parameter of the absorber materials. Compounds like LiZnP and LiCuS have been investigated in this thesis theoretically and experimentally [1, 19–23].

Another important application of the Half-Heusler compounds with 18 valence electrons is their usage as materials as thermoelectrics. Theoretical calculations show that these compounds are stable and have a band-gap in the range of 0 - 1.1 eV, which is suitable for thermoelectric applications [16, 24–28]. Several compounds like NiTiSn-based systems and CoTiSb-based systems have been investigated due to their good performance as thermoelectrics [29–33]. All these materials can easily be doped by elements, like for instance with Co, Cr, Cu, Fe on the Ni site [34, 35] or Bi, Ge, Pb and Sb on the Sn site [34, 36, 37] in the NiTiSn-system, leading to n- and p-type narrow gap semiconductors, from which one can fabricate p-n junctions. The doping can improve the thermoelectric properties of the material, minimizing for example the electrical resistivity, but keeping the thermal conductivity low, leading to a high figure of merit, which is an important requirement for good thermoelectrics.

Semiconducting Half-Heusler compounds can also be doped by magnetic impurities. This guides to the diluted magnetic semiconductors. The search for new materials for spintronics which exhibit semiconducting behavior and reveal magnetism remains a priority for solid-state chemistry [38]. It is well known, that closed-shell 18-electron compounds are non-magnetic and semiconducting. Kübler [39] has shown that the Slater-Pauling rule is applicable in order to describe the magnetic properties of Half-Heusler compounds with $C1_b$ structure. Most of these compounds contain Mn or rare-earth metals. By doping a semiconducting material with Mn, an influence of the magnetic properties can be observed. A series of various manganese doped semiconducting compounds were theoretically and experimentally examined in order to investigate the electronic and magnetic structure [40].

5 Experimental methods

All polycrystalline samples synthesized in this work were prepared by a reaction of the constituents, weighed in stochiometric or required amounts under an argon atmosphere. Most of the starting materials have a very high purity (see Table 5.1). They are mostly air and water sensitive. Therefore all handling was made under argon atmosphere using a glove-box. For the synthesis different crucible materials have been used. Usually Al_2O_3 and Tantalum crucibels were chosen. In case of Al_2O_3, all tubes were heated out at 1500 K in muffle-type furnaces before using them, and in case of the Tantalum tubes, they were baked out at 1200 K under Argon flow.

The crystal structure was investigated by powder X-ray diffraction using different radiation wavelengths depending on the material. For the materials investigated in Chapter 6 and Chapter 7 Mo K_α (λ = 0.7093 Å, Bruker, AXS D8), in reflection geometry and a Siemens D5000 diffractometer with Cu K_α radiation, wavelength (λ = 1.5418 Å), in Bragg geometry was used. This measurements were performed at the Institute for Inorganic and Analytical Chemistry, University of Mainz. The powder diffraction experiments for the materials studied in Chapter 8 and Chapter 9 have been performed using Cu $K\alpha_1$ radiation (λ = 1.5406 Å) in Debye-Scherrer geometry at the Max Planck Institute for Chemical Physics of Solids, Dresden. In addition, temperature-dependent powder XRD measurements were performed for LiMnAs (see Chapter 8.2.3) with a Stoe STADI II diffractometer with Mo $K\alpha_1$ radiation at the Institute for Inorganic Chemistry, Technical University of Darmstadt by G. Cordier. Powder neutron diffraction measurements on the series LiMgZ (Z = P, As, Sb), described in Chapter 6, were performed at the Laboratoire Leon Brillouin (LLB, Saclay, France) on the high resolution powder diffractometer $3T_2$ using a Ge(335) monochromator (λ = 1.2253 Å). All the samples were encapsulated in vanadium crucibles due to the high air and water sensitivity.

Elastic coherent neutron scattering experiments were performed on the high-resolution powder diffractometer SPODI at the neutron research reactor FRM II (Garching, Germany) [41] on LiCuS (see Chapter 9). Monochromatic neutrons (λ = 1.54832(2) Å) were obtained at a 155 ° take-off angle using the (551) reflection of a vertically-focused composite Ge monochromator. A vertical position-sensitive multidetector

Table 5.1: The used starting elements and their purity

Starting materials	Purity
Li (granulates; foil)	99%, Sigma Aldrich; 99.9%, Alfa Aesar
Mg (chips)	99.98%, Sigma Aldrich
P (powder)	99.99%, Sigma Aldrich
As (pieces)	99.999%, Sigma Aldrich
Sb (powder)	99.5%, Sigma Aldrich
Zn (granulates)	99.9999% Chempur, 99.99% Sigma Aldrich
Mn (powder; pellets)	99.99%, Sigma Aldrich
CuS (powder)	99.99%, Sigma Aldrich
Cu_2S (powder, anhydrous)	99.99% Sigma Aldrich
Li_2S (powder)	99.98% Sigma Aldrich

(300 mm effective height) consisting of 80 ^{3}He tubes and covering a 2 angular range of 160 ° was used for data collection. Measurements were performed in Debye-Scherrer geometry. The powder sample was filled into a thin-wall (thickness 0.15 mm) vanadium container of 8 mm in diameter under Ar atmosphere. The data collection was performed first at ambient temperature (300 K). After that the vanadium container with the sample was mounted in a top-loading closed-cycle refrigerator and cooled down. Helium 4.6 was used as a heat transmitter. The instantaneous temperature was measured using two thin film resistance cryogenic temperature sensors Cernox and controlled by a temperature controller from Lake Shore.

The magnetic properties were investigated by a super conducting quantum interference device (SQUID) using approximately 30 mg of the powder sample.

Differential scanning calorimetry (NETZSCH, STA 429) were performed on LiMnAs (Chapter 8.2.2) to detect the phase transitions below the melting point.

The electrical transport of the LiMgZ series, with Z = P, As, Sb (Chapter 6) was measured by the direct current (DC) method using pellets of round shape (diameter: 13 mm; thickness 1 mm) obtained by cold pressing using a hydraulic press (Perkin-Elmer) under a pressure of ca. 10 bar. The electric properties of the samples were obtained by impedance spectroscopy (IS) measurements. Li conductivity, σ DC, were determined from the DC plateau of the corresponding impedance spectra. IS was recorded as a function of temperature from -120 °C to 180 °C (Solartrin SI 1260 impedance gain phase analyzer with a high-resolution dielectric converter-Alpha high-resolution dielectric analyzer Novocontrol in the range from 10^{-1} - 10^6 Hz). The measurements were performed using stainless steel or platinum electrodes with

10 or 20 mm diameter under nitrogen flow. The resistivity of polycrystalline LiMnAs (Chapter 8.3.2) was recorded using the "Van der Pauw" method [42, 43] in the temperature range of 50 - 300 K.

The variable temperature (VT) static solid state nuclear magnetic resonance (NMR) measurements for LiMgZ (Z = P, As, Sb) (Chapter 6.3.2) were conducted using a 400 MHz Bruker Avance spectrometer at a frequency of 155.40 MHz and 8 kHz spinning at the magic angle for ^{7}Li. The measurements were recorded in the temperature range of 237 K to 390 K in 10 degree steps static and at ambient temperature. 5μs pulse length for the 90° single pulse excitation experiment and recycle delays of 120 s were used in all cases. 8 transients were averaged when acquiring the ^{7}Li NMR signal. A commercial 3-channels Bruker 4 mm probe-head, capable of fast MAS was used for all measurements. The spectra were referenced to external 3 M LiCl water solution. For the LiCuS serie (Chapter 9.5) ^{7}Li NMR (nuclear spin I = 3/2) measurements have been performed in a fixed field of 2.734 Tesla in a Janis 9 T cryostat at 4.2 K by using a commercial Tecmag pulse NMR spectrometer. The pulsed NMR spin echo 90° -180° sequence was applied. A 5 μs pulse has been used to excite the entire spectra and τ = 10 s repetition time was used to accumulate the spin echo because of the long nuclear spin lattice relaxation time of the semiconducting material at low temperatures. The Fourier transform of the spin echo in time domain gives the NMR line as a function of frequency.

The Ultraviolet-Visible (UV-VIS) diffuse reflectance spectra were acquired on a Varian UV-VIS-NiR Cary 5G spectrophotometer equipped with an integrated sphere (Ulbricht sphere) over the 200 - 800 nm. The measurements were performed at room temperature. A polytetrafluoroethylene (PTFE) plate was used as reference material.

Extended X-Ray Absorption Fine Structure (EXAFS) and X-ray Absorption Near Edge Structure (XANES) measurements on LiMnAs at the Mn edge (6539 eV) K were performed at room temperature in the transmission arrangement at the EXAFS beamline A1 of the Hamburg synchrotron radiation laboratory, HASYLAB, at DESY. Wavelength selection was realized by means of a Si(111) double-crystal monochromator. The near edge region of 6510 - 6560 eV was measured with a minimal step size of 0.25 eV, and the EXAFS regime was measured up to 7540 eV. A mass of approximately 10 mg of powdered Mn compounds with a particle size of $\leq$ 20 μm were diluted with B_4C powder and mixed with polyethylene powder.

Ellipsometric measurements (Chapter 8.3.3) covering the far-infrared to deep-ultraviolet spectral range (10 meV - 6.5 eV) were carried out at room temperature on LaOMnAs ceramic dense pellets polished to an optical grade finish. The measurements in the near-infrared to deep ultraviolet spectral range (0.75 eV - 6.5 eV) were performed with a rotating analyzer-type Woolam VASE variable-angle ellipsometer. For the infrared measurements from 0.01 eV to 1.0 eV, a home-built ellipsometers was used in combination with a Bruker Vertex 80v FT-IR spectrometer. Some of the experiments were performed at the infrared IR-1 beamline of the ANKA synchrotron light source at the Karlsruhe Institute of Technology, Germany.

6 Theoretical methods

Ab-initio calculations based on the density functional theory (DFT) with the Vienna Ab initio simulation package (VASP) [44, 45] code have been performed in order to gain further insights into the electronic structure and energetics for LiMnAs and LaOMnAs as described in Chapter 8.

For the approximate treatment of the electron exchange and correlation, we have used the Perdew, Burke, Ernzerhof funtional (PBE) [46] together with the projector-augmented wave (PAW) method with a plane-wave cutoff energy of 400 eV. In the irreducible part of the Brillouin zone, the k-point integration was performed on an 8×8×4 Monkhorst-Pack mesh.

To describe the magnetic ordering in these compounds as found from neutron diffraction measurements for the tetragonal antiferromagnetic structures, spin polarized calculations have been carried out for supercells containing four primitive unit cells.

From subsequent DFT calculations on LiMnAs and the related compound LaOMnAs, the magnetic exchange coupling constants J_{ij} of the classical Heisenberg model has been determined , $H = -\sum_{i>j} J_{ij}\hat{\mathrm{e}}_i\hat{\mathrm{e}}_j$, where $\hat{\mathrm{e}}_{i,j}$ are the unit vectors corresponding to the directions of the local magnetization at sites i and j. For this purpose, the SPR-KKR program package [47] has been employed, which is a suitable numerical tool for such computational task, not relying on pseudopotentials, where J_{ij} can be evaluated within the Green's function formalism. Based on the Mulliken analysis, the corresponding partial charges, i. e., oxidation numbers of Li, Mn, and As were computed. Due to computational limitations and difficulties from the perspective of the methodology, the implicit treatment of temperature effects in *ab-initio* calculations is not straightforward.

In Chapter 7 are shown the results obtained using the DFT calculations of the $\mathrm{LiZn}_{1-x}\mathrm{Mn}_x\mathrm{P}$ system, which have been performed using the SPR-KKR program package [47] based on the Korringa-Kohn-Rostoker (KKR) Green's function method together with the PBE [46] form of the generalized gradient approximation (GGA). In case of the Mn doped series we have employed the single-site coherent potential approximation (CPA) [48, 49] in order to take into account the random occupation between Zn and Mn. Furthermore, in order to try to describe the magnetic order from theory, we have carried out calculations to determine the magnetic exchange coupling constants J_{ij} between the Mn atoms.

DFT calculations have also been performed for the LiCuS system (Chapter 9) by employing the fully-relativistic Korringa-Kohn-Rostoker (KKR) Green's function method, as implemented in the SPR-KKR package [47]. For taking into account the random disorder due to the random occupation of atomic sites in LiCuS, we have used the single-site coherent potential approximation (CPA) [48, 49], which is a rather efficient mean-field technique. The electronic exchange and correlation was treated within the PBE [46] form of the generalized gradient approximation (GGA). In the calculations the experimental atomic structure and site occupations have been used.

7 LiMgZ (Z = P, As, Sb): Wide band gap semiconductors

7.1 Introduction

The text of this chapter is identical with the following publication:

A. Beleanu, M. Mondeshki, Q. Juan, F. Casper, F. Porcher and C. Felser
Systematical, experimental investigation on LiMgZ (Z = P, As, Sb) wide band gaps semiconductors
J. Phys. D: Appl. Phys, 44, 47 **(2011)**, 475302

The class of semiconductors commonly referred to as ”wide band gap semiconductors” hold promise for continued revolutionary improvements in the size, cost, efficiency and performance of a broad range of microelectronic and optoelectronic application [50]. Binary semiconductors can be realized from wide to low band gap (ZnO to HgTe). However very often the compounds show intrinsic defects [51, 52] or indirect band gaps [53], which makes a search for new semiconducting compounds necessary. However ternary semiconductors were not investigated systematically up to date. This contribution focus on the ternary semiconducting compounds LiMgZ (Z = P, As, Sb). The band gaps have been predicted theoretically [54] to be *direct* with a band gap of 2.43 eV for LiMgP [55–57], 2.31 eV for LiMgAs [58, 59] and 2.0 eV for LiMgSb [23].

The compounds LiMgZ (Z = P, As, Sb) belong to the, so called Nowotny-Juza compounds. Nowotny-Juza compounds $A^{I}B^{II}C^{V}$ based on three main group elements (A, B and C) exhibit the same crystal structure ($C1_b$) as the XYZ Heusler compounds, where X and Y are transitions metals and Z is a main group element. They can be viewed as zinc-blende III-V compounds in which the III column has been ”disproportionated” into A^{I}+B^{II} atoms [20].

The wide band gaps of these compounds, make them promising candidates for optoelectronics, ranging from blue lasers to cadmium free solar cell materials substituting CdS, CdSe or CdTe buffer layer materials in the chalcopyrite-based thin film solar cell devices [23, 56, 60]. This series has been synthesized by the reaction of the elements heated up at 900 ° for 12 h. The structure of these compounds was determined by X-ray and neutron diffraction measurements. ^{7}Li nuclear magnetic resonance spectroscopy was used to investigate the Li ion mobility. The band gaps were measured by optical reflectance spectrometry and electrical conductivity measurements.

7.2 Structural characterization

The crystal structure was investigated by means of X-ray powder diffraction (XRD) using a Siemens D5000 diffractometer with Cu K_α radiation, $\lambda = 1.5418$ Å, in Bragg geometry. Powder neutron diffraction measurements on the serie LiMgZ (Z = P, As, Sb) were performed at Laboratoire Leon Brillouin (LLB in Saclay, France) on the high resolution powder diffractometer $3T_2$ using a Ge (335) monochromator, to select a wavelength of 1.2253 Å. For analyzing the data, the obtained pattern were refined using the Fullprof package [61].

X-ray diffraction on LiMgZ (Z = P, As, Sb) showed a single homogeneous phase. All the patterns can be indexed based on the cubic unit cell. These compounds crystallize in the $C1_b$ structure type ($F\bar{4}3m$, $Z = 4$) according to the Rietveld analysis. The neutron diffraction measurements show additional peaks suggesting a distortion of the structure which is not observed in the X-ray powder patterns. (Figure 7.1). The Rietveld refinement on the neutron diffraction patterns confirmed the antifluorite structure. The Li atoms occupy the 4b position in ($\frac{1}{2}$,$\frac{1}{2}$,$\frac{1}{2}$) and Mg and P the 4a in (0,0,0) and 4c position in ($\frac{1}{4}$,$\frac{1}{4}$,$\frac{1}{4}$), respectively. The lattice parameters are summarized in Table 7.1.

Table 7.1: Lattice parameter a (Å) obtained by Rietveld refinement on X-ray and neutron diffraction pattern of LiMgZ with Z = P, As, Sb.

method	X-ray diffraction	neutron diffraction
LiMgP	6.010(9)	5.998(6)
LiMgAs	6.183(5)	6.176(1)
LiMgSb	6.628(5)	6.622(6)

In Figure 7.1 a), b) and c) are shown the measured powder diffraction pattern of the polycrystalline LiMgZ (Z= P, As, Sb) samples and c), d) and e) the measured neutron diffraction pattern collected at room temperature. The figures represent the fit of the diffractograms (red: observed, black: calculated by Rietveld and blue: difference plot). The lattice parameter a of LiMgZ (Z= P, As, Sb) increase from LiMgP to LiMgSb as expected with the increase of the radii of the corresponding pnictides. The lattice parameters are in good agreement with previously reported ones ([55–59]).

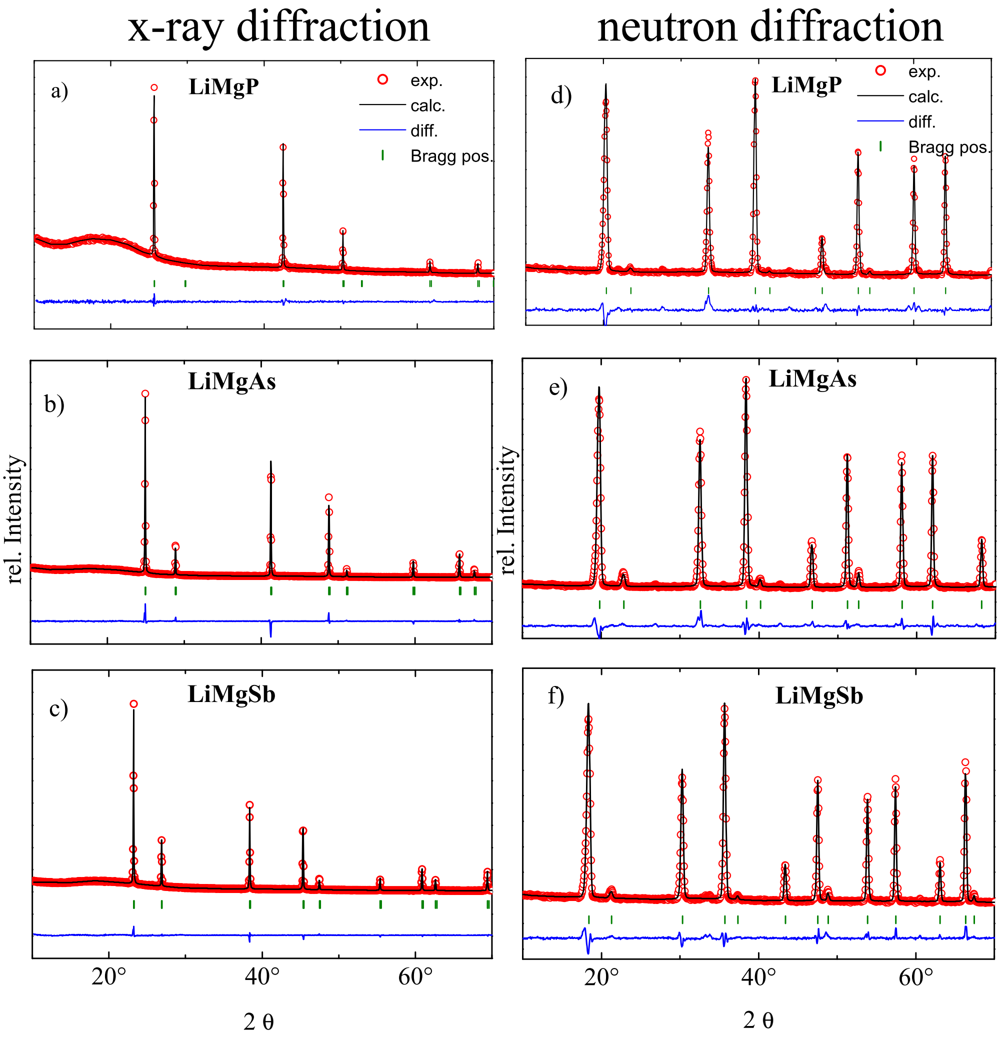

Figure 7.1: Observed powder X-ray (a, b, c) and neutron diffraction patterns (d, e, f) at room temperature of LiMgZ (Z = P, As, Sb) with the fit of the Rietveld refinement.

7.3 Experimental investigations

7.3.1 UV-VIS

For the study of the optical properties of the samples, the band gap nature was determined using a UV-VIS-NIR spectrophotometer in diffuse reflectance at room temperature over a range from 200 nm to 800 nm (6.20 eV to 1.55 eV). The optical absorption spectra of powder samples were converted from diffuse reflectance spectra using the Kubelka-Munk function [62]:

$$F(R_\infty) = \frac{K}{S} = \frac{(1-R_\infty)^2}{2R_\infty}, \tag{7.1}$$

where R_∞ is the diffuse reflectance for an infinitely thick sample, K and S are the Kubelka-Munk absorption and scattering coefficients, respectively. In most cases, S can be considered as a constant independent of wavelength. In the parabolic band structure the band gap E_g and absorption coefficient are related through the well-known Tauc equation [63]:

$$\alpha h\nu = C_1(h\nu - E_g)^\gamma, \tag{7.2}$$

where α is the linear absorption coefficient of the material, $h\nu$ is the photon energy, C_1 is a proportionality constant and γ is constant depending on the band-gap nature: $\gamma = 1/2$ for allowed direct band gap and $\gamma = 2$ for indirect band gap. Assuming the material scatters in perfectly diffuse manner, the K-M absorption coefficient K becomes equal to 2α. In this case, the Tauc equation becomes:

$$F(R_\infty)h\nu = C_2(h\nu - E_g)^\gamma, \tag{7.3}$$

Through the Tauc plot $[F(R_\infty)h\nu)]^{1/\gamma}$ the band gap E_g of a powder sample is extracted by linear extrapolating to the energy axis.

Figure 7.2 shows the Tauc plots for samples as direct band gap semiconductors. The energy gaps obtained are summarized in Table 9.4. They are 2.3 eV for LiMgP, 1.8 eV for LiMgAs and 0.9 eV for LiMgSb. The plots as indirect semiconductors (not presented) contain linear parts only in a small photon energy range. This leads to the conclusion that the converted absorption data obeys the relation of directness, which is in accord with previous reports [57–59].

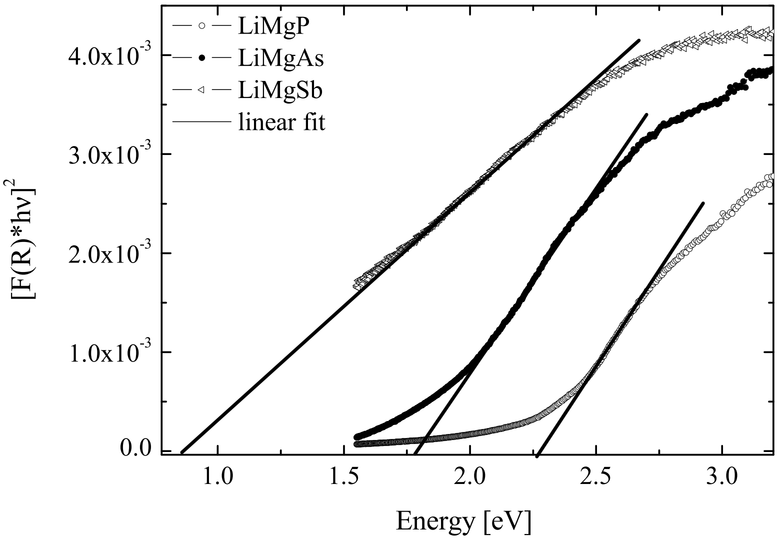

Figure 7.2: The Tauc plots for LiMgZ with Z = P, As, Sb as direct semiconductors. The lines mark the linear part used to estimate the band gap, with $\gamma = 1/2$.

7.3.2 NMR

Lineshape analysis of the ^{7}Li static resonances recorded as a function of temperature was applied to investigate the thermal behavior of the compounds. The full width at half maximum (FWHM) of the ^{7}Li signals in all compounds was determined in the temperature range 237 - 293 K and correlated with the long range Li ion transport, as measured by impedance spectroscopy.

It is well-known that in the rigid lattice regime the random distribution of lithium ions over the surplus of available sites, as well as the presence of structural defects, results in a distribution of the electric field gradients. Thus, the quadrupolar pattern, typical of a nucleus of spin $\frac{3}{2}$ looks smeared, with badly resolved satellites at the foot of the peak of the central transition. At higher temperatures above the onset of motional narrowing, the satellites disappear completely with only the single line of the central transition remaining. Further heating often results in a reappearance of the quadrupolar spectrum, however, with a smaller width [64].

As the central line is influenced predominantly by dipole-dipole interactions [65], magic angle spinning at 8 kHz was applied for the LiMg*Z* series to determine the signal maxima in separate experiments conducted at ambient conditions.

^{7}Li chemical shifts of 3.65 ppm, 3.10 ppm and 0.78 ppm were measured for the P, As and Sb analogues, respectively. The observed shift to higher fields is directly related with the changes in the electronic environment of the respective lithium nucleus which experiences higher shielding increasing the atomic number of the neighboring *Z* element.

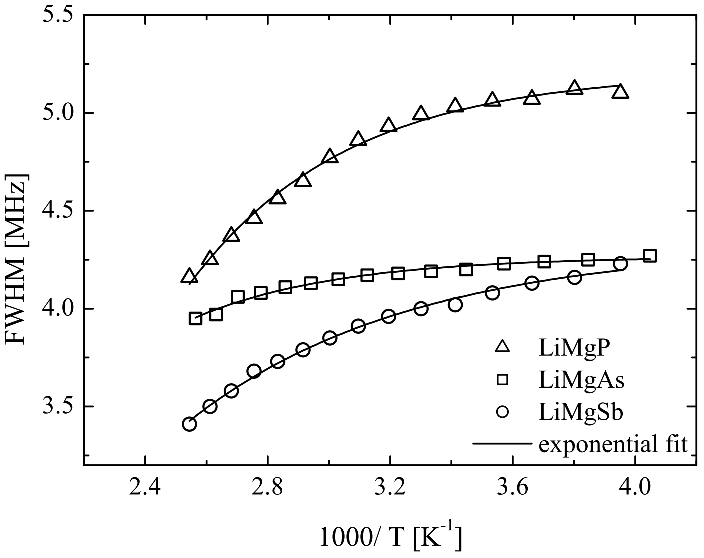

Figure 7.3: The full width at half maximum of LiMg*Z* with *Z* = P, As, Sb measured as a function of temperature. The lines mark the exponential fits.

Figure 7.3 presents the FWHM of the ^{7}Li NMR resonances in the static spectra of LiMg*Z* (*Z* = P, As, Sb) analogues with the respective exponential fits. The clear tendency of decreasing peak widths with increasing temperature is directly related to the increased Li ion mobility, that leads to motional narrowing. A correlation time of the Li ion hopping motion could not be extracted, because in the present experiments lower temperatures were not accessible to observe the onset of the narrowing.

7.3.3 DC-Conductivity

The temperature dependence of the DC electrical conductivity for LiMgZ (Z = P, As, Sb) from 153 to 473 K is shown in Figure 7.4 in which the lines correspond to linear fits to the data. The data were analyzed by an Arrhenius plot according to:

$$\sigma_{dc} \propto \exp(-\frac{E_a}{k_B T}), \tag{7.4}$$

where k_B is Boltzmann's constant, T is the temperature and E_a is the activation energy. For intrinsic semiconductors the activation energy E_a has a value about half of the band gap ($E_a = E_g/2$) [66]. The activation energy E_a is determined by the Arrhenius plot of this expression, as listed in Table 9.4. From Figure 7.4 it is clear that with the increase of atomic number of the anion from P to Sb, the samples show higher conductivity.

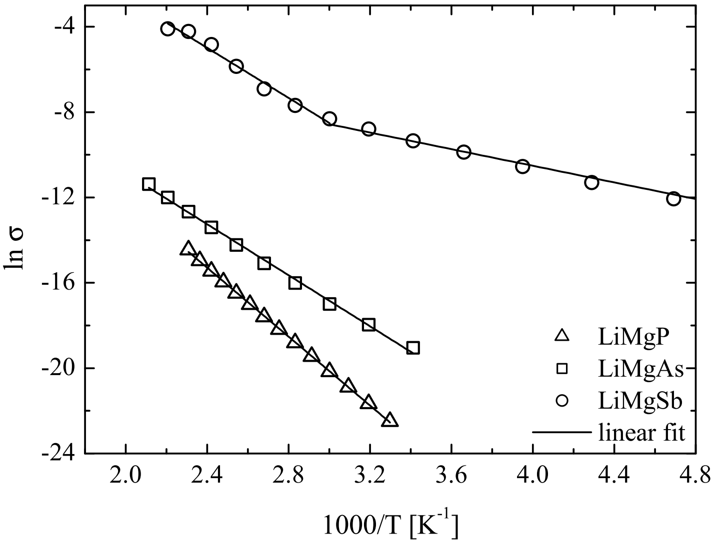

Figure 7.4: The temperature dependence of the DC conductivity of LiMgZ, with Z = P, As, Sb.

Near room temperature LiMgSb shows the highest electrical conductivity of $1.5 \cdot 10^{-4}$ S/cm while LiMgP shows the lowest of $3.2 \cdot 10^{-10}$ S/cm. Within the measured temperature range, LiMgP and LiMgAs exhibit intrinsic conducting behavior with $E_a =$ 0.74 eV and 0.52 eV, respectively. On the contrary, LiMgSb shows two sections of activated conducting with a small E_a of 0.19 eV indicating doped levels at low temperatures and a larger E_a of 0.48 eV at high temperatures. The latter value is close to $E_g/2$ for LiMgSb obtained in Fig.7.2, suggesting intrinsic conducting behavior at this temperature range.

Table 7.2: Electrical conductivity σ, activation energy E_a and optical band gap energy of LiMgZ (Z = P, As, Sb)

Z	P	As	Sb
σ [S/cm]	$3.23{\cdot}10^{-10}$	$1.58{\cdot}10^{-8}$	$1.51{\cdot}10^{-4}$
E_a [eV]	0.73	0.52	0.48
E_g [eV]	≈2.30	≈1.80	≈0.9

7.4 Conclusions

In summary it has been shown that the compounds LiMgZ (Z = P, As, Sb) crystallize in the crystal structure type C1$_b$ (space group $F\bar{4}3m$). The neutron diffraction measurements suggest a distortion of the structure which can promote the mobility. The possible modulation of the Lithium substructure will be a subject of further investigations. Optical reflectance measurements identified the direct band gap of these compounds. It has been found that LiMgZ (Z = P, As, Sb) are wide band gap semiconductors with band gaps E_g of ≈ 2.3, 1.8 and 0.9 eV, respectively. The line-shape analysis of the ^{7}Li static NMR spectra recorded as a function of temperature exhibit a clear tendency of decreasing the peak widths increasing the temperature, which is directly related with the increased Li ion mobility.

8 LiZn$_{1-x}$Mn$_x$P (x = 0.4, 0.8, 0.10): Diluted magnetic semiconductors?

8.1 Introduction

A fascinating class of novel materials are magnetic semiconductors. An example is Ga$_{1-x}Mn_x$As [67], which has so far the highest reported Curie temperature. The III-V semiconductors such as GaAs are already frequently used in many electronic and optoelectronic devices. The state of the technique to obtain magnetic III-V semiconductors is to dope them with a high concentration of magnetic ions. LiZnMnAs [68, 69] was later discussed as ferromagnetic semiconductor, feature which was obtained by increase of the Lithium concentration.

LiZnP is a so called Nowotny-Juza compound. This compounds have the general composition A^{I}B^{II}C^{V} with A, B and C as main group elements. They are isotypic to XYZ Half-Heusler compounds (C1$_b$) with X and Y usually transition metals and Z a main group element [70, 71]. LiZnP has been investigated experimentally several times [20–23] and its electronic structure and properties have been studied using DFT calculations (LDA) [19]. The crystal structure and the band structure are related to that of GaAs. They can be understood based on the Zintl-Klemm concept. The strong electropositive Li transfers charge to the Zn and P partial structure. The polyanion [ZnP$^-$] in Li$^+$[ZnP$^-$] forms a Zinc-blende partial structure according to the Zintl-Klemm concept. In this work, the electronic structure of pure and Mn doped LiZnP has been examined to obtain an insight into its electronic and magnetic properties.

All samples of the series LiZn$_{1-x}$Mn$_x$P (with $0 < x < 0.35$) were prepared by the reaction of the pure elements. Stoichiometric amounts of the constituents were weighed and filled into corundum crucibles under Ar atmosphere. Subsequently, the crucibles were sealed in evacuated quarz tubes and heated at 900 °C for 96 h. Powder X-ray diffraction measurements were carried out using Cu K$_\alpha$ radiation (λ = 1.540598 Å). The diffraction patterns were refined using the Fullprof suite of programs [61].

The magnetic properties were investigated by a superconducting quantum interference device using approximately 20 - 50 mg of the sample.

UV-VIS diffuse reflectance spectra were acquired by means of a Varian UV-VIS-NIR Cary 5G spectrophotometer equipped with an integrated sphere (Ulbricht sphere). The measurements were performed at room temperature from 200 to 800 nm. A PTFE (polytetrafluoroethylene) plate was used as reference material.

8.2 Structural characterization

Powder X-ray diffraction measurements were carried out to ensure phase purity of the polycrystalline samples. As shown in Figure 8.1, single phase samples were obtained for Mn contents x = < 0.12. For higher Mn concentrations additional phases were observed (marked with *) which can be attributed to metallic Mn and to tetragonal LiMnP. For the single phase compounds all the patterns could be indexed with a cubic unit cell. It is possible to fit the lattice parameters as a function of x linearly in this range, which is in agreement with Vegard's rule [72]. Rietveld refinement of the PXRD data revealed that the compounds crystallize in space group

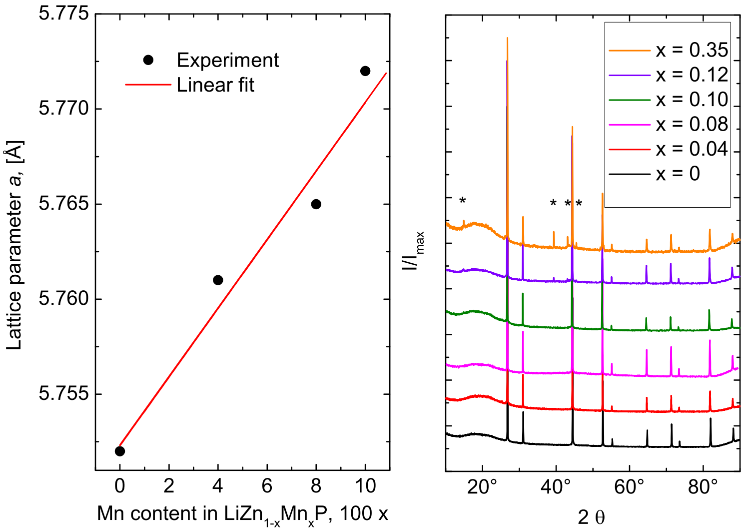

Figure 8.1: **(a)** The lattice parameter for $LiZn_{1-x}Mn_xP$ (x = 0, 0.04, 0.08, 0.10) and in **(b)** Powder X-ray diffraction patterns for $LiZn_{1-x}Mn_xP$ (x = 0, 0.04, 0.08, 0.10, 0.12, 0.35) recorded at room temperature. The Bragg peaks of the additional phases Mn and LiMnP are marked by *.

$F\bar{4}3m$, as explained below. Li occupies the $4b$ position $(\frac{1}{2},\frac{1}{2},\frac{1}{2})$, Zn occupies the $4a$ position (0,0,0) and P occupies the $4c$ position $(\frac{1}{4},\frac{1}{4},\frac{1}{4})$. By the substitution of Mn with Zn, the Mn atoms occupy the same Wyckhoff position like Zn, namely the $4a$ position. Furthermore, the lattice parameter increases with increasing Mn content from 5.752(4) Å for undoped LiZnP to 5.772(8) Å for 10% Mn content as expected (Figure 8.1 **a**). A linear fit results in $a = a_0 + b_0 x$, with $a_0 = 5.75 \pm 0.8 * 10^{-3}$ and $b_0 = 0.0022$. Figure 8.1 **b)** shows the typical X-ray powder diffraction pattern of polycrystalline $\mathrm{LiZn}_{1-x}\mathrm{Mn}_x\mathrm{P}$ samples.

8.3 Optical properties

For the study of the optical properties of the samples, the band gap nature was determined using a UV-VIS-NIR spectrophotometer in diffuse reflectance at room temperature from 200 nm to 800 nm (6.20 eV to 1.55 eV). The optical absorption spectra of the powder samples were converted from the diffuse reflectance spectra using the Kubelka-Munk function [62]:

$$F(R_\infty) = \frac{K}{S} = \frac{(1 - R_\infty)^2}{2R_\infty}, \tag{8.1}$$

where R_∞ is the diffuse reflectance for an infinitely thick sample, K and S are the Kubelka-Munk absorption and scattering coefficients, respectively. In most cases, S can be considered as a constant independent of wavelength. In the parabolic band structure the band gap E_g and absorption coefficient are related through the well-known Tauc equation [63]:

$$\alpha h\nu = C_1(h\nu - E_g)^\gamma, \tag{8.2}$$

where α is the linear absorption coefficient of the material, $h\nu$ is the photon energy, C_1 is a proportionality constant and γ is constant depending on the band-gap nature: $\gamma = \frac{1}{2}$ for allowed direct band gap and $\gamma = 2$ for indirect band gap. Assuming the material scatters in perfectly diffuse manner, the K-M absorption coefficient K becomes equal to 2α. In this case, the Tauc equation becomes:

$$F(R_\infty)h\nu = C_2(h\nu - E_g)^\gamma, \tag{8.3}$$

Using the Tauc plot $[F(R_\infty)h\nu)]^{1/\gamma}$ the band gap E_g of a powder sample was obtained by linear extrapolating to the energy axis.

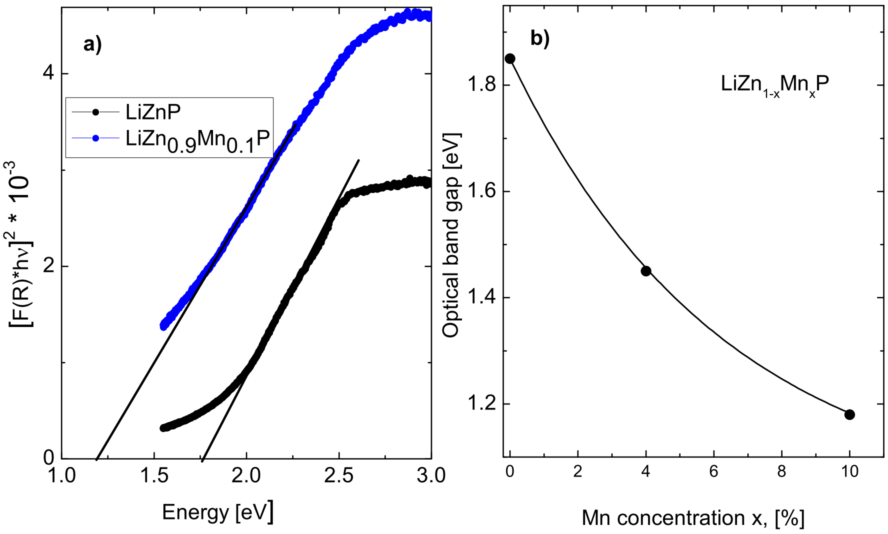

Figure 8.2: a) $F(R) * h\nu^2$ versus photon energy plot at x = 0.1 and LiZnP; b) Optical band gap as a function of Mn content for polycrystalline LiZn$_{1-x}$Mn$_x$P (x = 0, 0.04, 0.10). The line fit corresponds to an exponential function ($\gamma = 1/2$).

Figure 8.2 shows the Tauc plots assuming a direct band gap semiconductors. The reduction of the band gap from LiZnP (1.80 ev) to the doped LiZn$_{0.90}$Mn$_{0.10}$P (1.18 eV) is attributed to the formation of an impurity band above the valence band. Band structure calculation also indicate a reduction of the band gap due to the impurity band formation.

8.4 Magnetic properties

The magnetic properties of LiZn$_{1-x}$Mn$_x$P, with x = 0.04, 0.08, 0.10, were investigated using a superconducting quantum interference device in the temperature range of 5 to 300 K. Samples of approximately 25 - 50 mg were used for the analysis. In all the magnetically diluted compounds a Curie Weiss paramagnetic behavior is observed.

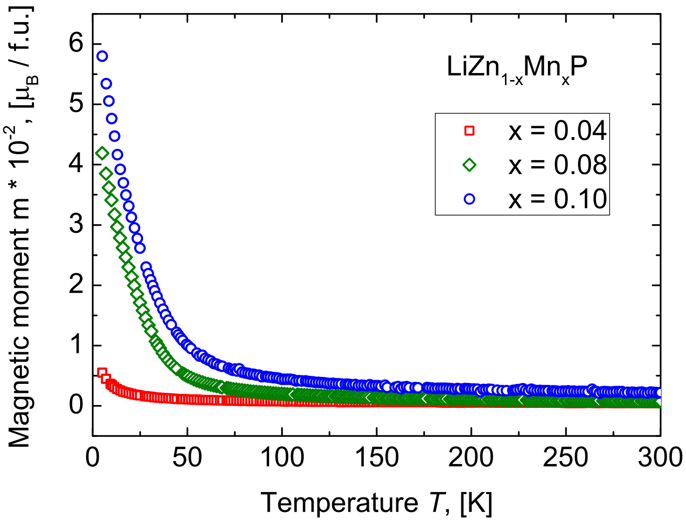

Figure 8.3: The temperature dependent magnetization curves (M vs T) for $\mathrm{LiZn}_{1-x}\mathrm{Mn}_x\mathrm{P}$, with x = 0.04, 0.08, 0.10, measured during heating in an induction field of 1 Tesla.

Temperature dependent magnetic measurements were performed. Figure 8.4 shows the temperature dependent inverse susceptibility measured at 1 Tesla magnetic field of $\mathrm{LiZn}_{1-x}\mathrm{Mn}_x\mathrm{P}$, with x = 0.04, 0.08, 0.10.

In the high temperature region, above 160 K, a Curie Weiss Fit was applied using the Curie-Weiss Law,

$$\chi = \frac{C}{T-\theta} \longrightarrow \frac{1}{\chi} = \frac{1}{C}T - \frac{\theta}{C} \tag{8.4}$$

For all samples a negative Weiss constant was obtained, θ = -239.95 K for x = 0.04 Mn containing sample and θ = -51.735 K for the 8% Mn containing sample, which indicates an anti-parallel alignment of the spins characteristic for antiferromagnetic interactions. For $\mathrm{LiZn}_{0.96}\mathrm{Mn}_{0.04}\mathrm{P}$ and $\mathrm{LiZn}_{0.92}\mathrm{Mn}_{0.08}\mathrm{P}$ a Curie Constant of 0.0013 and 0.0015 respectively was obtained. For $\mathrm{LiZn}_{0.90}\mathrm{Mn}_{0.10}\mathrm{P}$ a small deviation from the observed trend was obtained. By increasing the Mn content a Curie constant of 0.5613 and θ=-164.57 K has been obtained.

The field dependent magnetization measurements performed at 5 K exhibit very narrow hysteresis loops with almost zero coercive field. This behavior is typical for soft magnetic materials. The magnetic moment m (5 Tesla) increases with increasing the Mn content as shown in the Figure 8.5. Unfortunately, the saturation magnetization was not reached for induction fields up to 5 Tesla (Figure 8.5).

The shape of the magnetization curve can be corrected applying a loop correction. The paramagnetic loop correction to a Langevin function $L(H)$ is given by,

$$M(H) = \chi_{lin} H + M_0 L(H), \tag{8.5}$$

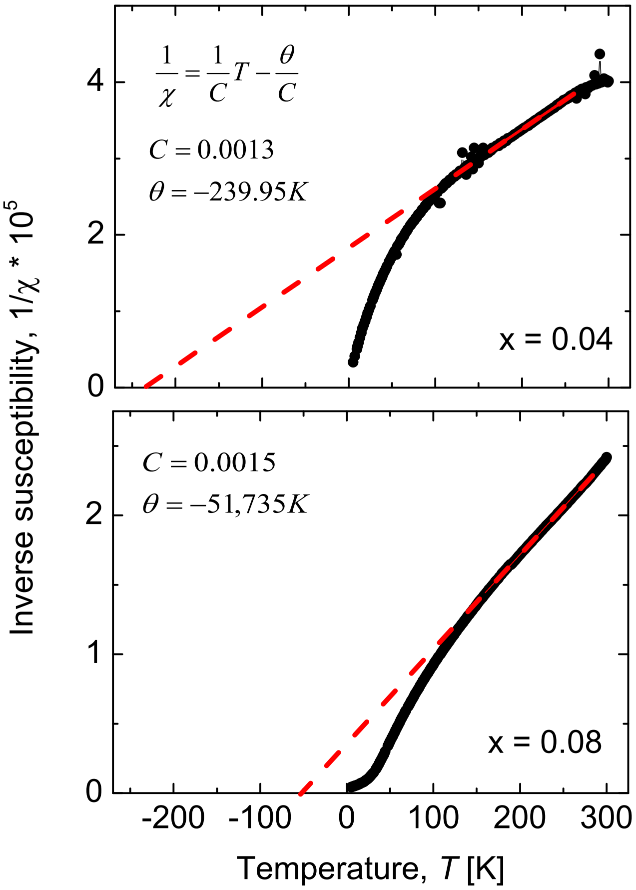

Figure 8.4: The inverse susceptibility as a function of temperature of $LiZn_{1-x}Mn_xP$, with x = 0.04 and 0.08. The red dashed line show the Curie Weiss Fit above 160 K.

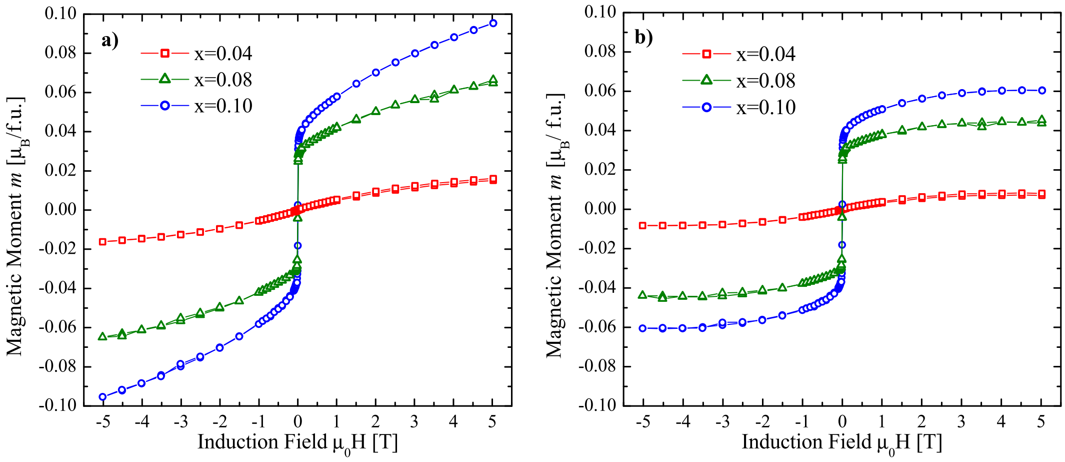

Figure 8.5: Magnetic field dependent hysteresis loop of $\mathrm{LiZn_{1-x}Mn_xP}$, x = 0.04, 0.08, 0.10, measured at 5 K; (a) before and (b) after the paramagnetic loop correction.

where χ_{lin} is the field independent paramagnetic susceptibility and the M_0 is the saturation moment. A saturation magnetic moment of ca. 0.6 μ_B/Mn atom is obtained after this correction as seen in Figure 8.5 for x = 0.08 and x = 0.10 Mn doped LiZnP. For the x = 0.04 Mn doped LiZnP sample a very small saturation magnetic moment is observed.

Using the Curie Law for the high temperature regions,

$$\frac{M}{H} = \chi = \frac{C}{T-\theta} = \frac{N \cdot \mu_0 \cdot m^2}{3 \cdot k_B} \cdot \frac{1}{T-\theta} \tag{8.6}$$

the magnetic moment can be also obtained by plotting the inverse susceptibility, $1/\chi$, versus the temperature, T. In the equation 8.6., M is the magnetization in A/m, H is the magnetic field A/m, χ is the magnetic susceptibility, C is the Curie constant, T is the temperature in K, θ is the Curie temperature in K, N is the number of the magnetic atoms per unit volume (1/m^3), k$_B$ is the Boltzmann constant ($1.38062 \cdot 10^{-23}$ J/K, J = V·A·s), μ_0 is the vacuum permeability ($1.2566 \cdot 10^{-6}$ V·s/A·m). Using this formula a magnetic moment per unit cell, m = 0.78 μ_B for $\mathrm{LiZn_{0.96}Mn_{0.04}P}$ and m = 0.57 μ_B for $LiZn_{0.92}Mn_{0.08}P$ has been obtained, which is in agreement with the values obtained above.

8.5 Theoretical calculations

For LiZnP and Mn doped $LiZn_{1-x}Mn_xP$ (x = 0.04, 0.08, 0.10) density functional theory (DFT) calculations have been performed using the SPR-KKR program package [47] based on the Korringa-Kohn-Rostoker (KKR) Green's function method together with the PBE [46] form of the generalized gradient approximation (GGA). In case of the Mn doped series we have employed the single-site coherent potential approximation (CPA) [48, 49] in order to take into account the random occupation between Zn and Mn.

The band structure calculated using this methodology for LiZnP, $LiZn_{0.96}Mn_{0.04}P$ and $LiZn_{0.90}Mn_{0.10}P$, where we have assumed a ferromagnetic ordering of the Mn moments are presented in Figure 8.6. For LiZnP we have computed with the PBE functional a value for the direct band gap of 1.36 eV, which is lower than the experimentally measured 1.80 eV. Due to the fact that both the local density approximation (LDA) and generalized gradient approximation (GGA) tend to underestimate the band gap of semiconducting materials

For the Mn doped compound, our calculations show, that the Mn impurities will act as magnetic dopants, giving rise to new states in the semiconducting gap of LiZnP, thereby reducing the gap to 0.79 and 0.52 eV for the $LiZn_{0.96}Mn_{0.04}P$ and $LiZn_{0.90}Mn_{0.10}P$, respectively.

Although these theoretically computed band gaps are smaller than the 1.18 eV measured for the $LiZn_{0.90}Mn_{0.10}P$, our trends from the theory are in good agreement with the experiment, especially considering that the theoretical gap for the pure compound was already underestimated.
Since the theoretical treatment of paramagnetic materials within ab-initio calculations is rather difficult, we have carried out instead three calculations, where we have compared the various properties of spin-degenerate calculations to collinear spin-polarized solutions. As expected for a paramagnetic material, we found, that the ferromagnetic and antiferromagnetic solution is energetically nearly degenerate with the ferromagnetic solution being 8 - 12 meV/f.u. more stable than the antiferromagnet for the range of x = 0.04 - 0.10 Mn concentration. Furthermore, both spin-polarized solutions are considerably lower in energy compared to the spin-degenerate result, which is more than 90 meV/f.u. higher in energy compared to the ferromagnetic solution.

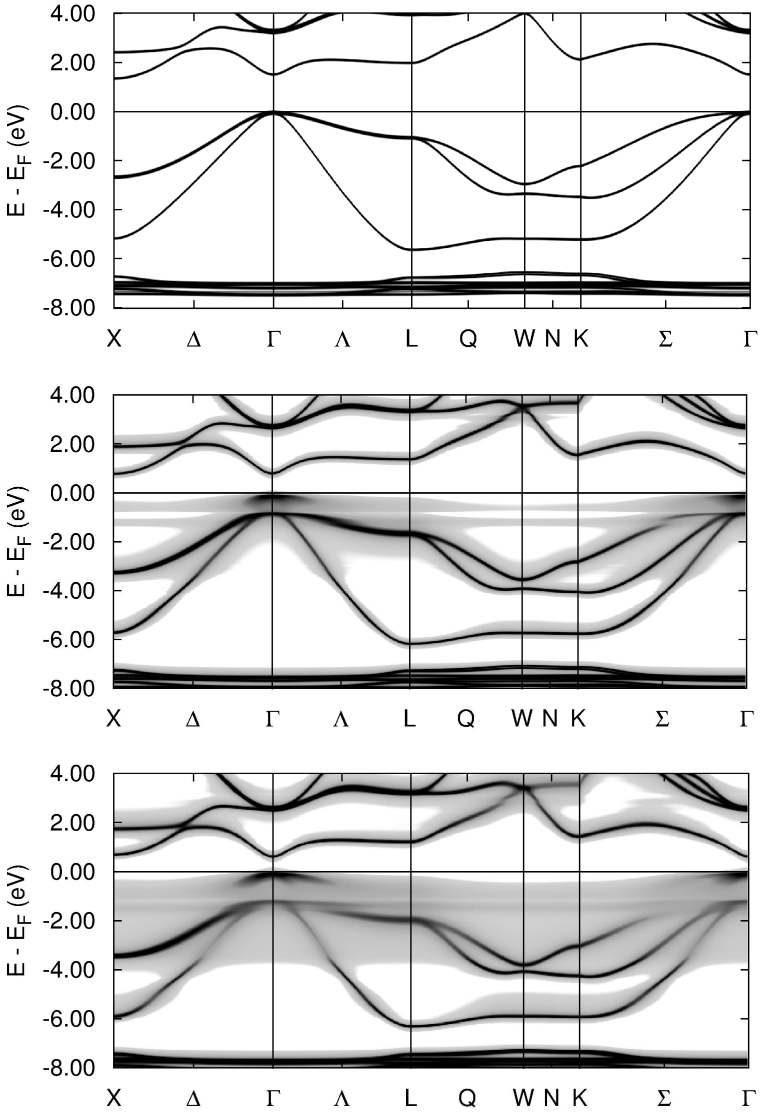

Figure 8.6: Band structure calculated for the pure LiZnP (top panel) compared to the Bloch spectral function of the Mn doped $\mathrm{LiZn_{0.96}Mn_{0.04}P}$ (middle panel) and $\mathrm{LiZn_{0.90}Mn_{0.10}P}$ (bottom panel) computed for the ferromagnetic ordering of the Mn moments.

We found, that from the perspective of the band gap there is no mentionable quantitative difference between the ferromagnetic and antiferromagnetic order. In both cases magnetic dopants lead to the appearance of a new state in the gap, making the gap smaller compared to the pure LiZnP.

The calculated local moments on the Mn atoms were 3.68, 3.70, 3.72 and 3.76 μ_B for the x = 0.04, 0.06, 0.08 and 0.10 Mn dopant concentrations, respectively, which agrees rather well with the measured values presented in the previous section. Assuming a ferromagnetic order, the calculated total magnetic moments per unit cell were 0.19, 0.23, 0.31 and 0.33 μ_B, respectively, which are only about half of the values measured for the paramagnetic compound.

In order to try to describe the magnetic order from theory, we have carried out calculations to determine the magnetic exchange coupling constants J_{ij} between the Mn atoms. We found, that DFT predict, that for the low x = 0.04 Mn concentration a weak antiferromagnetic, wheres for the x = 0.10 Mn doped compound a ferromagnetic ordering should be present. In the plane of the Zn atoms substituted by Mn the Mn moments are always coupled antiferromagnetic, but the next nearest neighbors are coupled ferromagnetic, leading to a frustrated magnetic system at 0 K in the ground state.

Still, the computed J_{ij} exchange coupling values are rather small, being in the range of 0.2 − 3.2 meV, which are more than an order of magnitude lower than in other related compounds showing ferro- or antiferromagnetic ordering. Thus, it is not surprising that in the experiment such weak exchange coupling interactions at T > 0 will result in a paramagnetic behavior.

8.6 Summary

Mn doped samples, LiZn$_{1-x}$Mn$_x$P with $0 < x < 0.35$ have been prepared by the reaction of the elements. Mn substituts Zn atoms according to the Rietveld refinement of powder X-Ray pattern. The lattice parameter increase linearly according to the Vegard's rule by increasing the Mn content. The magnetic properties are not influenced by this substitution and there is no indication of ferromagnetism, as expected. A possible explanation is a lack a free carriers, which are not induced like in LiZnMnAs system, where the ferromagnetic behavior is influenced by a higher concentration of the Li atoms. [68]. Unfortunately, these compounds cannot be used as magnetic diluted semiconductors showing a paramagnetic behavior at room temperature. All the samples exhibit a Curie Weiss behavior at higher temperature and negative Weiss constant, which leads to antiferromagnetic interactions.

All investigated samples have a direct band gap, according to optical measurements. The reduction of the band gap from LiZnP (1.80 eV) to doped LiZn$_{0.90}$Mn$_{0.10}$P (1.18

eV) is attributed to the formation of an impurity band above the valence band. Band structure calculation also indicate a reduction of the band gap due this impurity band formation.

9 LiMnAs: A possible candidate for spintronics

9.1 Introduction

The text of this chapter is identical with the following publication:

A. Beleanu, J. Kiss, G. Kreiner, C. Köhler, L. Müchler, W. Schnelle, U. Burkhardt, S. Chadov, S. Medvediev, D. Ebke, G. Cordier, B. Albert, A. Hoser, F. Bernardi, T. I. Larkin, D. Pröpper, A. V. Boris, B. Keimer and C. Felser
Large resistivity change and phase transition in the antiferromagnetic semiconductors LiMnAs and LaOMnAs
Phys. Rev. B, 88, **(2013)**, 475302

The idea of using semiconductors in spintronic devices has stimulated a new field of research. This is because by using not only the charge of the electron, but also its spin to store and manipulate information has led to a new paradigm in condensed matter research to overcome the limitations set by Moore's law [73]. Unfortunately, semiconductivity and ferromagnetism above room temperature are not compatible. Presently, to circumvent this issue, diluted magnetic semiconductors such as GaMnAs [74, 75] and LiZnMnAs [68, 69] are used. Recently, the use of antiferromagnetic (AFM) semiconductors has been proposed, because they have a higher magnetic ordering temperature compared to diluted magnetic semiconductors.

One promising candidate material for new spintronic applications is LiMnAs, given its suitable band gap and high magnetic moment per Mn atom [76]. It was demonstrated that epitaxially grown LiMnAs thin films also show semiconducting behavior [76], and their AFM ordering has been confirmed [76–78] as well.

Thus, LiMnAs, LaOMnAs, and related materials allow for the study and development of new AFM semiconductors, and the compounds are also interesting from a purely academic viewpoint.

CuMnAs [79] has also been suggested as an alternative semiconducting AFM material; however, this compound shows semimetallic behavior in contrast to the desired semiconducting properties. Still, the compounds with the general formula AMnX, where A = Li, Ni, Cu, or LaO and X = As or Sb offer a good starting point for the development of novel semiconducting magnetic materials for applications in devices such as single-electron transistors [80].

In the ground state, both LiMnAs and LaOMnAs show AFM insulating behavior. Chemically, LiMnAs consists of ionic Li^+ and tetrahedral [$MnAs^-$] layers (see Fig. 9.1), with Mn^{2+} in a d^5 and As^{3-} in a nominal s^2p^6 closed shell configuration. LiMnAs is isostructural to LiFeAs superconductor [81]. Structurally, LaOMnAs is closely related to LiMnAs (see Figure 9.1) and to the LaOFeAs layered superconductor. In comparison to LiMnAs, where the Mn moments are ordered antiferromagnetically both in the *ab* Mn planes and between the Mn planes stacked along the *c* axis [82], in the case of LaOMnAs, the moments are aligned antiferromagnetically in the *ab* plane but ferromagnetically along *c* [83].

Interestingly, in contrast to the expected 5 μ_B of the $S = \frac{5}{2}$ Mn^{2+} ion, neutron scattering data on LiMnAs and LaOMnAs suggests a magnetic moment of approximately 3.4 to 3.8 μ_B, which is close to the magnetic moment of 4 μ_B for an $S = 2$ Mn^{3+} ion. This closely resembles the simple rules and general observation made regarding Heusler compounds [84], stating that Mn tends to have a large localized magnetic moment with an oxidation state of 3 (in the literature referred to as the Kübler's rule [85]) in a nominal d^4 configuration. The magnetism then stems from the nonbonding *d* electrons, as can be best observed in Half-Heusler compounds, where only Mn or rare-earth-containing compounds form stable magnetic phases [17, 38].

The aim of this work is multifold: we elaborate on the synthesis and bulk characterization of polycrystalline LiMnAs and LaOMnAs, and compare their properties to other related compounds based on a short review from the literature on the AMnX family. We show that LiMnAs can undergo a first-order phase transition from the tetragonal to a cubic phase. In addition, we discuss the electronic and magnetic properties of LiMnAs and LaOMnAs, including their transport properties. By combining *ab-initio* density functional theory (DFT) calculations with our experiments, we discuss the electronic structure and magnetic exchange coupling of the Mn atoms, further commenting on the non-Curie-Weiss-like behavior experimentally reported for related compounds [86].

We also address an open question arising from a previous work [83], regarding the weak ferromagnetic behavior observed in LaOMnAs, which so far has been attributed to a small spin canting.

However, thus far, it was not taken into consideration that the formation of small amounts of MnAs as impurities during synthesis ($\leq$1%) cannot be excluded com-

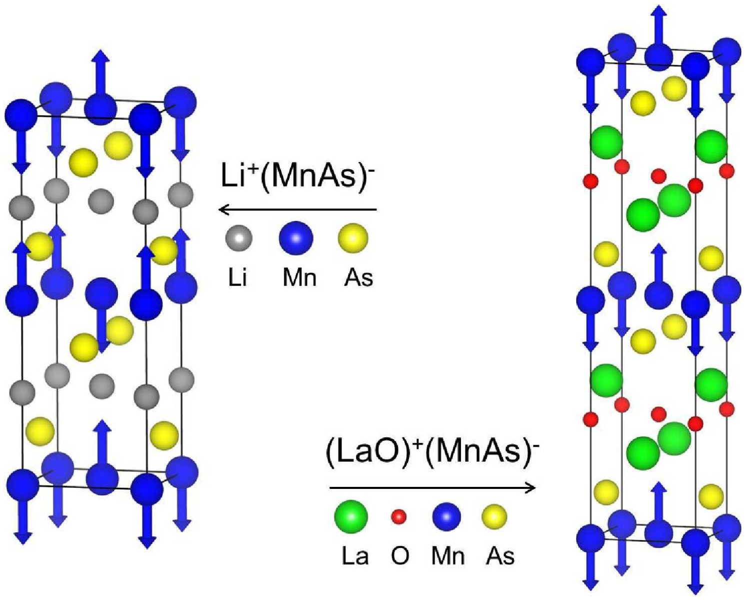

Figure 9.1: Crystal and magnetic structure of LiMnAs and LaOMnAs. The blue arrows indicate the direction of the magnetic moments of the Mn atoms.

pletely, and this could explain the weak ferromagnetic behavior.

In Ref. [87] it was already noted, that in the $A\mathrm{Mn}X$ series, where A is an alkali metal, and X is an element from the 15^{th} group of the periodic table, there is a correlation between the local moments of Mn and the Mn–Mn distances ($d_{\mathrm{Mn-Mn}}$). That is, a shorter $d_{\mathrm{Mn-Mn}}$ results in lower moment of Mn. The $d_{\mathrm{Mn-Mn}}$ distance plays a major role in the magnetism of these compounds, whose behavior is transferable to LiMnAs [82], LaOMnAs, and other materials. The structural and magnetic data for the AMnAs series derived from neutron diffraction measurements is collected from the literature in Table 9.1.

Before turning to the presentation of our results, in Table 9.2 first we provide a general overview of the most important characteristics and material properties of various compounds for the aforementioned $A\mathrm{Mn}X$ class, with $A = \mathrm{Li}$, LaO. Table 9.2 serves as a set of reference values, providing a solid basis of comparison with our measured data for LiMnAs and LaOMnAs, using which we can derive more general conclusions that are applicable to the entire family. As the data in Table 9.2 show, the materials in the $A\mathrm{Mn}X$ family can be classified into two main categories: those that are semiconducting or semi-metallic with AFM ordering, and those which are metallic or half-metallic and ferromagnetic (FM). There is a correlation between

Table 9.1: Short overview from the literature on the results obtained with neutron diffraction measurements on *A*MnAs compounds, where *A* is an alkali metal.

Compound	T [K]	a [Å]	c [Å]	$d_{\mathrm{Mn-Mn}}$ [Å]	m [μ_{B}]
LiMnAs*	10	4.262(1)	12.338(1)	3.008(3)	3.67(3)
NaMnAs [82]	14	4.199(1)	14.164(1)	2.969(1)	4.01(5)
KMnAs [82]	14	4.382(1)	15.558(1)	3.099(1)	4.03(5)
RbMnAs [86]	10.6	4.400(5)	16.128(5)	3.111(1)	4.05(4)
CsMnAs [87]	10	4.417(1)	17.370(1)	3.123(1)	4.07(2)

*results from this work

Table 9.2: Structural, electronic and magnetic properties of various *A*Mn*X* based compounds, where A = Li, Ni, Cu, or LaO and X = As or Sb, and the binary MnAs compound. The shortest Mn–Mn distance is given by $d_{\mathrm{Mn-Mn}}$.

Compound	Electronic structure	Magnetic order	Mn magnetic moment [μ_{B}]	$d_{\mathrm{Mn-Mn}}$ [Å]	Space group
LiMnAs [82]	semiconductor	AFM	3.8	3.008	$P4/nmm$ (tetragonal)
CuMnAs [79]	semimetal	AFM	no data	3.452	$Pnma$ (orthorh.)
CuMnSb [79, 88]	semimetal	AFM	3.9	4.301	$F\bar{4}3m$ (cubic)
LaOMnAs [83, 89]	semiconductor	AFM	3.34	2.914	$P4/nmm$ (tetragonal)
NiMnAs [90]	half metallic-ferromagnet	FM	4.0	4.051	$F\bar{4}3m$ (cubic)
NiMnSb [88, 91]	half metallic ferromagnet	FM	4.0	4.186	$F\bar{4}3m$ (cubic)
MnAs [92, 93]	metallic	FM	3.4	3.730	$P6_3/mmc$ (hexagonal)

$d_{\mathrm{Mn-Mn}}$ distances, and the magnetic and electronic properties of these materials.

In other words, those compounds that have $d_{\mathrm{Mn-Mn}} \leq 3.1$ Å tend to be AFM semiconductors. In the range of $3.1 \leq d_{\mathrm{Mn-Mn}} \leq 3.5$ Å they are semimetallic and AFM (except CuMnSb which has $d_{\mathrm{Mn-Mn}}$ of 4.301 $\AA$), and those with $d_{\mathrm{Mn-Mn}} \geq 3.5$ are metallic and FM. As a general trend, this indicates that the further apart the Mn atoms are from each other, the more likely it is that they develop high moments, leading to a FM metal. Hence, by adjusting the lattice parameters, the magnetic and electronic properties of the AMnX compounds can be tuned over a wide range. Indeed, as an example, for LaOMnP (isostructural to LaOFeAs), it was shown very recently that upon doping and external pressure, the system can undergo a phase transition from an AFM insulator to a metallic antiferromagnet [94].

9.2 Experimental details

9.2.1 Synthesis

LiMnAs was synthesized and characterized as bulk material in the 1980s [82, 95] by a high-temperature reaction of the elements lithium, manganese, and arsenic.

It was found that this compound is AFM-ordered, where the Néel temperature is approximately 400 K, but the exact Néel temperature is not known.

Using a similar synthesis route, our preliminary experiments revealed a number of small Bragg reflections in powder X-ray diffraction (XRD) patterns of the target compound caused by impurities. These Bragg peaks become significantly stronger with increasing temperature and reaction time and stem from an attack of the tantalum ampoule by arsenic. Therefore, LiMnAs was prepared as follows: mixtures of stoichiometric amounts of Li (foil), Mn (chips) and As (pieces) (all 99.999% purity) were placed in Al_2O_3 crucibles. The total mass was approximately 2 g per sample. Each crucible was enclosed in an arc-sealed tantalum ampoule at 300 mbar Ar, which in turn was jacketed by an evacuated fused silica ampoule.

A grey powder was obtained after heating the mixtures to 1423 K with a low heating rate of 1 K/min in a muffle furnace. This temperature was maintained for 2 h and then reduced to 1173 K. After 24 h, the ampoules were quenched in water. All of the handling was performed in a glove-box under Ar ($p(O_2, H_2O) \leq 1$ ppm).

LaOMnAs was synthesized from the starting materials LaAs, Mn, and MnO_2 in stoichiometric amounts at 1423 K for 42 h in an Al_2O_3 crucible, which was in turn enclosed in an evacuated and fused silica tube.

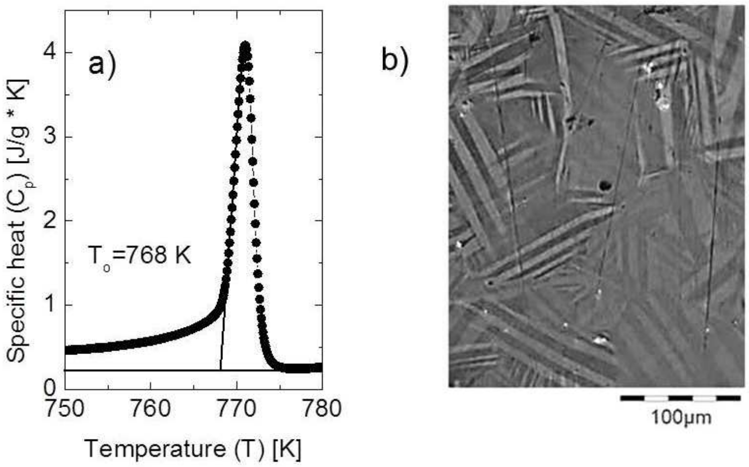

Figure 9.2: (a) The DSC peak at 771 K with an onset temperature of $T_\mathrm{o} = 768$ K corresponds to the phase transformation to the cubic high temperature phase. (b) Optical bright field image at room temperature showing the domain structure of LiMnAs induced by the phase transformation.

9.2.2 Chemical properties

Chemical analysis for non-metal impurities were carried out using the carrier gas hot extraction or the combustion technique (LECO[6]). For all samples the impurities were below the limit of detection (LOD in ppm): N(20), O(100), C(150), H(10). The 1:1:1 target composition was checked by atomic emission spectrometry with plasma excitation resulting in Li:Mn:As = 1.03(1):0.98(1):0.99(1).

A specimen for metallographic examination was prepared from one sample. Due to the moisture and air sensitivity this was done in a glovebox using paraffin oil as lubricant. A bright field image of the microstructure is shown in Figure 9.2b which reveals a domain structure. This is a typical signature for a tetragonal phase formed from a high temperature cubic phase.

Specific heat measurements of LiMnAs in the temperature range of 240–780 K revealed only one DSC peak (see Figure 9.2a) corresponding to a reversible phase transition with onset temperature $T_\mathrm{o} = 768$ K.

9.2.3 Crystal and magnetic structure

Powder X-ray diffraction (PXRD) of the final product showed single-phase LiMnAs. The powder diffraction experiment was performed with Cu $K\alpha_1$ radiation ($\lambda = 1.5406$ Å) in Debye-Scherrer geometry. The sample was sealed in a glass capillary with a 0.3 mm diameter.

Representative XRD pattern obtained in the temperature range of 273 – 873 K are shown in Figure 9.3 with a Rietveld refinement carried out using Jana 2006 [96]. LiMnAs has a tetragonal unit cell with $a = 4.2555(1)$ Å and $c = 6.1641(2)$ Å ($P4/nmm$, $Z = 2$, Li on $2b$, Mn on $2a$, As on $2c$ and $z(\text{As}) = 0.7575(2)$) in agreement with the older reports.

To identify the nature of the phase transition, temperature-dependent powder XRD was performed with a Stoe STADI II diffractometer with Mo $K\alpha_1$ radiation at the Zintl Institute, Technical University Darmstadt. The powder (20–50 μm) was sealed in a 0.5 mm quartz glass capillary. The measurements were carried out in the range from 323 K to 873 K in steps of 50 K. The observed powder patterns are shown in the range of $14° \leq 2\theta \leq 25°$ in Figure 9.3. All powder patterns up to 723 K can be indexed based on a tetragonal unit cell, whereas the powder patterns at 823 K and 873 K are indexed based on a cubic unit cell with $a_{\text{cub}} \approx c_{\text{tet}} \approx a_{\text{tet}}\sqrt{2}$.

The high-temperature phase, HT-LiMnAs, crystallizes in MgAgAs structure type ($F\bar{4}3m$, $Z = 4$, Li on $4b$, Mn on $4a$ and As on $4c$) according to the Rietveld analysis. The temperature dependence of the lattice parameters a_{cub}, c_{tet} and $a_{\text{tet}}\sqrt{2}$ as well as the unit cell volume in a pseudo-cubic setting are plotted versus the temperature in Figure 9.4. Both parameters a and c increase nearly linearly with $\alpha_{a\sqrt{2}} = 1.57 \cdot 10^{-4} \pm 4 \cdot 10^{-6}$ Å/K and $\alpha_c = 1.35 \cdot 10^{-3} \pm 4 \cdot 10^{-6}$ Å/K up to 600 K. Above 650 K, a increases and c decreases until they match at 768 K, where $a \approx 6.101$ Å. The volume increases linearly with the temperature expansion coefficient of $\alpha_{\text{V}} = 0.00832 \pm 1 \cdot 10^{-6}$ Å^3/K.

The structural relationship between tetragonal LiMnAs and the high-temperature cubic form is shown in Figure 9.5 with the tetragonal structure given in the pseudo-cubic setting. The crystal structure at room temperature form can be described as an alternate stacking of slabs composed of edge connected slightly distorted MnAs_4 and LiAs_4 tetrahedra. The MnAs_4 tetrahedra are slightly smaller than the LiAs_4 tetrahedra. At higher temperatures the c/a ratio in pseudo-cubic setting approaches one. At 768 K, all tetrahedra become regular and half of the Li and Mn atoms of each layer exchange positions with each other in such a way that a Half-Heusler structure

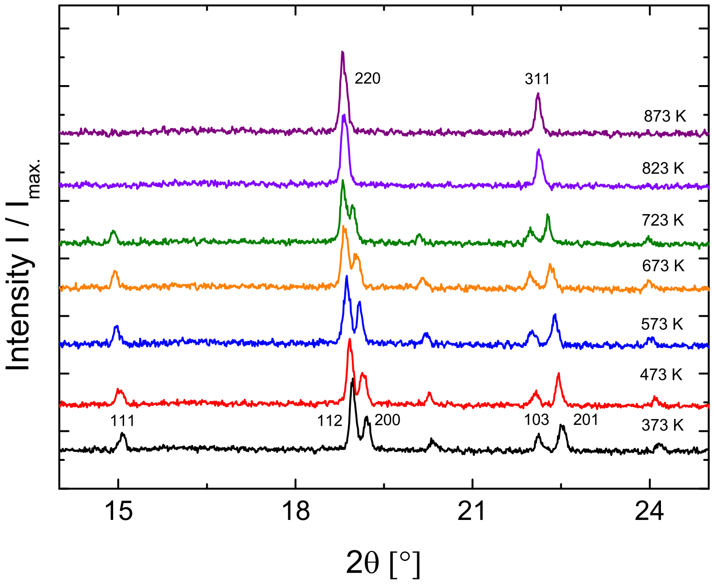

Figure 9.3: Observed X-ray powder patterns in the range $14° \leq 2\theta \leq 25°$ of LiMnAs for various temperatures from 373 K to 873 K. The patterns up to 723 K can be indexed primitive tetragonal. At 823 K and above, LiMnAs crystallizes in a face-centered cubic structure.

is obtained. The diffusion of the Li atoms to the Mn sites and vice versa likely occurs via the empty Li_4As_4 cubes, showing that Li is rather mobile in LiMnAs. There is no perceptible discontinuity in the volume curve at the temperature of the phase transition, and c/a transits smoothly to one. Although this fulfills the requirements for a second-order phase transition, the fast exchange of Li and Mn cannot be described by a continuous process. This can therefore be only a first-order phase transition. The measured change in the entropy and the enthalpy at the phase transition temperature is $\Delta H_{\text{trans}} = 2.19$ J/(Kmol) (≈ 23 meV/f.u.) and $\Delta S_{\text{trans}} = 2.85$ J/(Kmol).

For the magnetic characterization of LiMnAs, neutron powder diffraction patterns were recorded on the E6 Focusing Powder Diffractometer at Helmholtz-Zentrum Berlin, Germany, using the wavelength $\lambda = 2.448$ Å. The measurements were performed at seven different temperatures in the range from 1.6 K to 873 K. Five diffraction patterns in the range of 1.6 K to 300 K correspond to tetragonal and

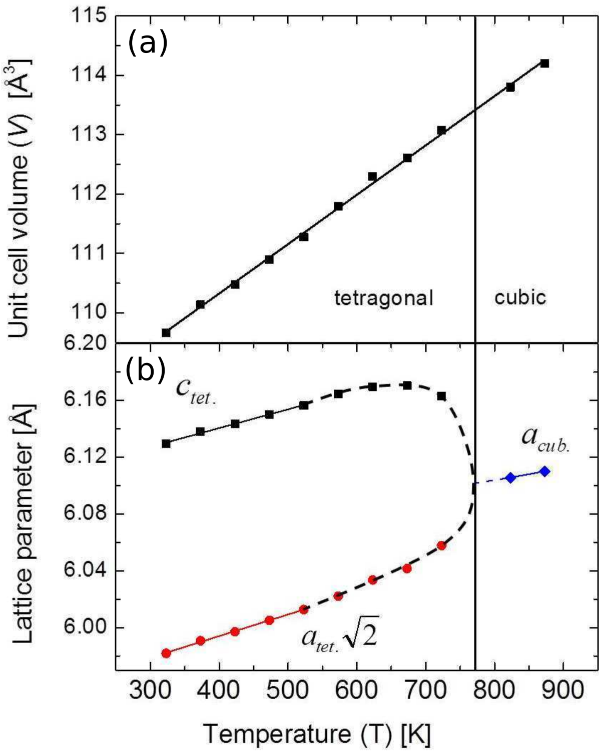

Figure 9.4: (a) The unit cell volume of LiMnAs ($Z = 4$) increases linearly from 373 K to 873 K. There is no perceptible volume jump at the phase transition temperature. (b) Lattice parameter (from the XRD measurements on LiMnAs) versus temperature for the tetragonal and cubic phases. Below 600 K, the curves are fitted by a linear function. The dashed line at a higher temperature serves as a guide to the eye.

antiferromagnetically ordered LiMnAs. To protect the sample against moisture and oxidation, a 10 mm fused silica tube was filled and sealed under vacuum. A representative neutron powder diffraction pattern obtained at 1.6 K is shown in Figure 9.6 along with the fit from the Rietveld refinement using the nuclear and magnetic structures.

Table 9.3 lists crystallographic data obtained from the Rietveld refinements of the crystal structures based on neutron powder patterns at various temperatures. The powder patterns below the ordering temperature reveal Bragg peaks of magnetic order that can be indexed with the modulation vector $\vec{k} = (0, 0, 1/2)$. This cor-

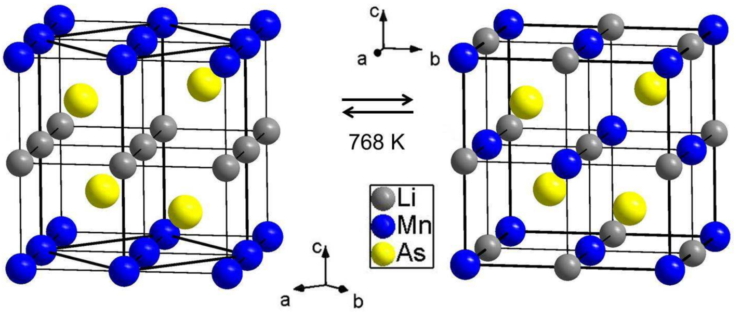

Figure 9.5: Crystal structures of LiMnAs: (a) tetragonal primitive and (b) face-centered.

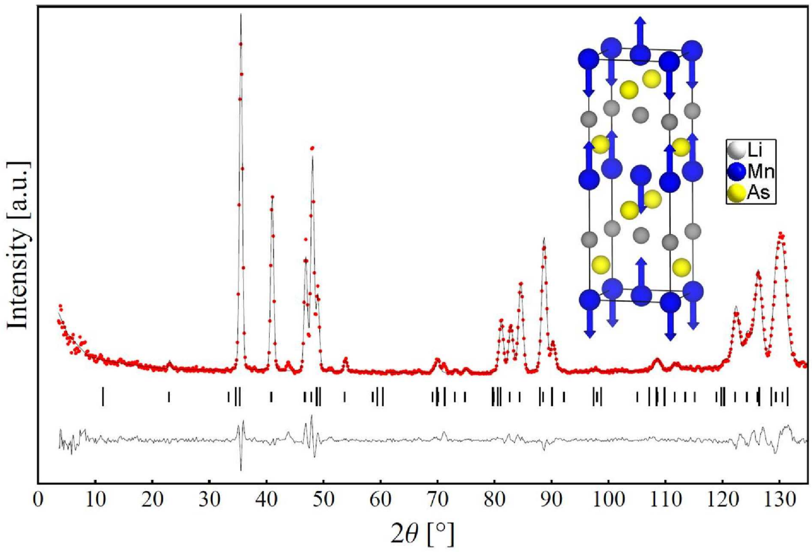

Figure 9.6: Observed neutron powder pattern (points) for LiMnAs at 1.6 K with the fit of the Rietveld refinement of the nuclear and magnetic structure. The markers of the Bragg reflections for the nuclear reflections (short lines), magnetic reflections (long lines), along with the difference curve are shown at the bottom. The inset shows the alignment of the magnetic moments along the *c* axis.

responds to an antiferromagnetically ordered structure doubling the *c*-axis of the nuclear structure. The refinement in the magnetic space group P_C4_2/ncm (Belov

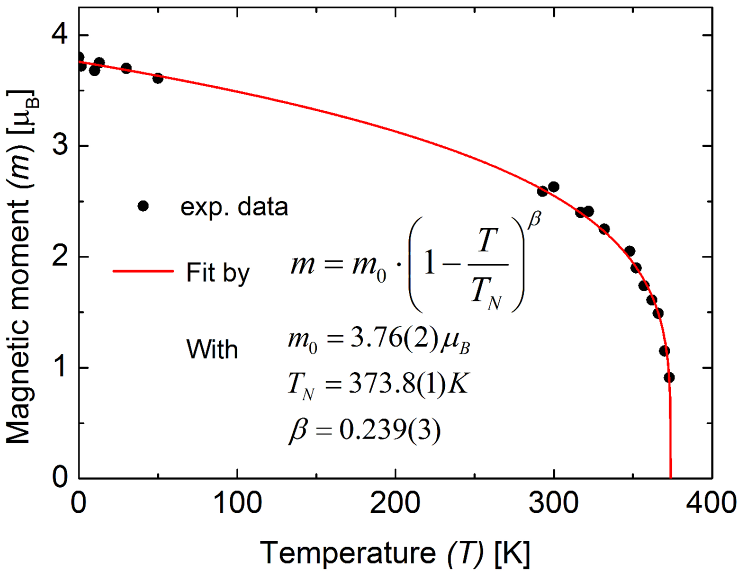

Figure 9.7: Ordered Mn magnetic moment m of LiMnAs as a function of temperature T. The solid curve through the data is fitted to a power-law function with critical exponent β.

notation) reveals that the magnetic moments at the Mn sites with 3.7 μ_B at 1.6 K are aligned parallel to the c axis. These observations are in good agreement with the previously reported data, except that the magnetic space group was wrongly assigned in Ref. [82]. The low temperature magnetic moment of 3.7 μ_B is smaller than the value of 5 μ_B expected for the high-spin ($S=\frac{5}{2}$) state of Mn^{2+}, assuming a g-factor of 2 ($\mu = g \cdot S \cdot \mu_B$).

Figure 9.7 shows the temperature dependence of the magnetic moment m obtained from the refinement of the neutron diffraction data. All data below 380 K were fitted by the power law of $m(T) = m_0(1 - T/T_N)^{\beta}$ with Néel temperature, $T_N = 373.77$ K and the critical exponent $\beta = 0.239$.

Regarding the magnetism of LaOMnAs, in Ref. [83], it was found that it is antiferromagnetically ordered in the ab plane, similar to LiMnAs, according to neutron diffraction analysis at lower temperatures. The small increase in the magnetic moments was explained [83] by a weak ferromagnetic behavior as a result of a small spin canting. Such canting could be caused by broken inversion symmetry, giving rise to the Dzyaloshinskii-Moriya [97, 98] interaction modifying the magnetic ground state, which ceases to remain collinear. However, in LiMnAs and LaOMnAs, the

Table 9.3: Crystallographic data for tetragonal antiferromagnetically ordered and tetragonal paramagnetic LiMnAs and for the high temperature cubic phase of LiMnAs. The z parameter for As in the antiferromagnetically ordered structure is half of that of the paramagnetic structure. In a cubic setup it is defined as $1 - z = 1/4$. For comparison, the magnetic moment of Mn^{2+} determined from neutron diffraction measurements is also given together with data from Ref. [82]. The residual factors, R_B, for the magnetic and nuclear parts are not provided because they are nearly equal for each measurement (approximately 6%).

T[K]	a [Å]	c [Å]	V[Å^3]	z	$m[\mu_B]$
1.6	4.262(1)	12.338(1)	224.12	0.3787(5)	3.72(3)
10	4.262(1)	12.338(1)	224.12	0.3795(5)	3.68(3)
13 [82]	4.253(1)	12.310(1)	222.66	0.3800(1)	3.75(3)
30	4.262(1)	12.338(1)	224.12	0.3796(5)	3.70(3)
50	4.261(5)	12.337(9)	224.00	0.3789(1)	3.61(3)
293 [82]	4.267(1)	12.356(1)	224.97	0.3800(1)	2.59(2)
300	4.259(2)	12.333(4)	223.70	0.3813(1)	2.63(3)
317	4.269(2)	12.363(4)	225.20	0.3792(1)	2.40(3)
322	4.269(2)	12.366(4)	225.40	0.3796(1)	2.41(3)
332	4.270(2)	12.372(4)	225.60	0.3778(1)	2.25(3)
348	4.272(2)	12.374(4)	225.80	0.3771(1)	2.05(3)
352	4.273(2)	12.373(4)	225.80	0.3800(1)	1.90(3)
357	4.274(2)	12.377(4)	226.00	0.3783(1)	1.74(3)
362	4.273(2)	12.380(4)	226.00	0.3799(1)	1.61(3)
366	4.276(2)	12.380(3)	226.40	0.3802(4)	1.49(3)
370	4.275(3)	12.383(3)	226.20	0.3783(4)	1.15(3)
373	4.275(2)	12.382(3)	226.20	0.3814(3)	0.91(3)
393* [82]	4.273(1)	12.370(1)	225.86	0.3800(1)	1.59(3)
423 [82]	4.279(1)	6.193(1)	113.39	0.7610(2)	-
573	4.289(5)	6.203(0)	114.11	0.7582(1)	-
873	6.155(4)	-	233.18	1/4	-

*magnetic moment not compatible with our data

inversion symmetry break occurs anyway at their surfaces or interfaces. Thus, in bulk LaOMnAs we would expect, that canting plays a negligible role. Instead of canting, we explain the small remanent total moment of these compounds with the formation of MnAs as an impurity phase. This is because during synthesis, independent of the method used, tiny amounts of MnAs ($\leq 1\%$) can easily be formed, which cannot be detected by techniques such as XRD or energy-dispersive X-ray spectroscopy (EDX). As shown by the data in Table 9.2, MnAs is an ordered FM material. It has a Curie temperature of approximately 320 K [99] exactly coinciding with the magnetic transition temperature in our measurements. Thus, the presence of MnAs impurities in the samples offer a more straightforward explanation for the small remanent total moments reported in Ref. [83], rather than spin canting.

Regarding the non-Curie-Weiss-like behavior of the magnetization as a function of temperature reported for related AMnX compounds [86], our DFT calculations (see below) have shown that within the layers, the Mn moments are very strongly coupled relative to the weak interlayer couplings. Additionally, in LiMnAs between the layers, the Mn atoms are actually coupled ferromagnetically with their next nearest neighbors and antiferromagnetically with their second nearest neighbors. Because of this complex interaction between Mn moments, even above the Néel temperature, a short-range local order is present, causing the non-Curie-Weiss-like behavior described above.

9.3 Physical properties

9.3.1 EXAFS, XANES

The environment and the valence state of the Mn atoms in LiMnAs have been investigated by means of extended X-ray absorption fine-structure (EXAFS) and (XANES) measurements.

The 10 mg powdered Mn compounds were diluted with B_4C powder and mixed with polyethylene powder. The mixture was pressed to form a pellet with a diameter of 10 mm. All of the handling was performed under an argon atmosphere in a glovebox. Reference data were measured simultaneously with a Mn-foil. This spectrum serves as an external reference for energy calibration and Mn valency.

Figure 9.8 shows the EXAFS signal, $\chi(k)$, and the corresponding Fourier transform. The EXAFS data were analyzed in accordance with the standard procedure for data reduction,[100] using IFFEFIT [101]. The FEFF program was used to obtain the phase shift and amplitudes [102]. The EXAFS signal $\chi(k)$ was extracted and Fourier-transformed (FT) using a Kaiser-Bessel window with a $\Delta(k)$ range of 7.0 Å^{-1}. The $\chi(k)$ curve shows the characteristic pattern for this compound. The FT pattern shows one broad peak at approximately 2.2 Å (uncorrected for the phase shift), which corresponds to the Mn–As and Mn–Mn scattering contributions. The Mn–Li scattering contribution is also included in this region; however, it does not have a

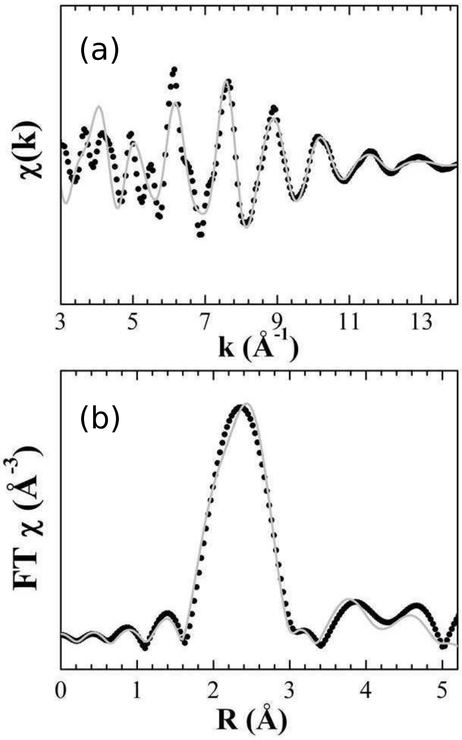

Figure 9.8: (a) 293 K Mn EXAFS (points) and the corresponding best fit (solid line) of LiMnAs. (b) Fourier transform of the 293 K Mn EXAFS (points) and the corresponding best fit (solid line) of LiMnAs.

strong influence on the main peak. The grey line in Figure 9.8 represents the best fitting curve of the data. The structural parameters obtained from the Rietveld refinement were used as the input data to generate the cluster of atoms used.

Only single scattering events were considered in the fitting procedure. The excellent agreement between the data and the theoretical structure was accomplished by the low R factors($\leq 0.6\%$). A quantitative analysis extracted from the EXAFS data is summarized in Table 9.4. The amplitude-reduction term $(S_0)^2$ used was 0.75. The Mn–As and Mn–Mn distances are slightly contracted by $\leq 2\%$ and the Mn–Li by $\approx 7\%$ compared to the crystallographic data.

In Table 9.4, the distances obtained by the neutron-diffraction refinement are com-

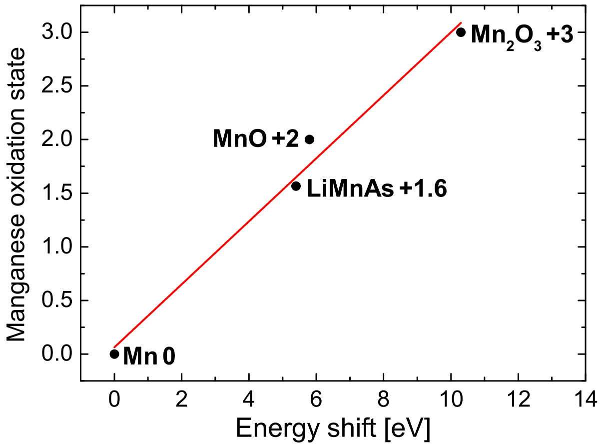

Figure 9.9: Plot of the oxidation state of Mn in elemental manganese and in various compounds versus the energy shift obtained from XANES measurements.

pared with the EXAFS data. The oxidation state of Mn in LiMnAs was obtained by using the XANES analysis with a widely used method as described by Wong *et al* [103]. This method considers the determination of the edge shift in relation to the Mn^0 edge energy for a given compound.

In this case, there is a linear relation between this energy shift and the oxidation state. Using the oxidation state and energy shift of some standard oxides (Mn_2O_3 and MnO in this case), it is possible to find a linear relation, and obtain the oxidation state for the compound (Figure 9.9). This method reveals an oxidation state of Mn in LiMnAs of 1.6. Such a decrease in the oxidation state can be expected from weak homonuclear Mn–Mn interactions in the *ab* plane. This is supported by DFT

Table 9.4: Quantitative results for LiMnAs from the EXAFS data analysis for the Mn K edge, considering the coordination numbers (CN) of the crystal structure. The best fitting exhibits the next-neighbor distances (R), mean square displacement in R σ^2, and R-factor for the whole fit.

Shell	Element	CN	d [Å]	R_{EXAFS} [Å]	σ^2 [Å^2]	R [%]
1st	As	4	2.601	2.550	0.006	0.6
2nd	Mn	4	3.012	2.953	0.006	
3rd	Li	2	3.085	2.870	0.006	

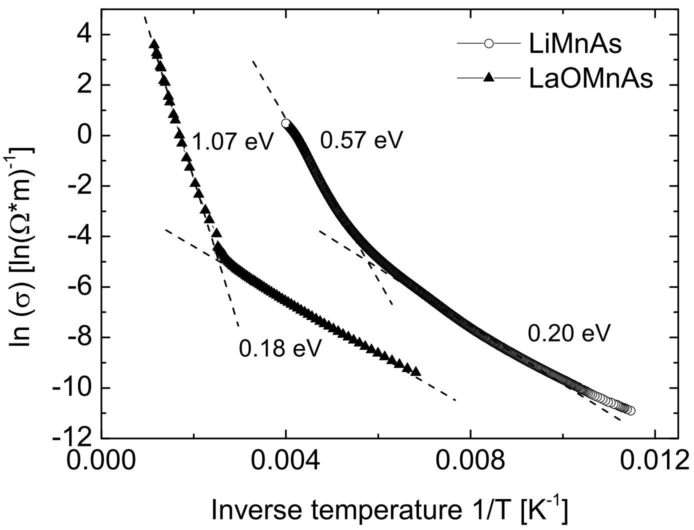

Figure 9.10: Arrhenius plot of the electrical conductivity for LiMnAs and LaOMnAs. At low temperatures, the curves correspond to the extrinsic regime, and at high temperature, (low $1/T$), to the intrinsic regime.

calculations (see below), which show a considerable interaction in the planes of Mn atoms, affecting their hybridization.

9.3.2 DC-Resisitvity

The resistivity of polycrystalline LiMnAs was recorded using the "Van der Pauw" method [43] in the temperature range of 50-300 K. For LaOMnAs, the electrical resistivities ρ(T) from 100-400 K were obtained by a standard linear four-point contact method. The measurement was performed by means of a physical property measurements system (PPMS, Quantum design model 6000, supported by LOT Germany). Bars of LaOMnAs $2 \times 2 \times 8$ mm^3 were cut from pellets obtained by a spark plasma sintering (SPS) process.

Both LiMnAs and LaOMnAs show very high resistivity below ca. 100 K. The resistivity measurements suggest a semiconducting behavior. The Arrhenius equation and an Arrhenius plot were used in order to obtain the activation energy, which has

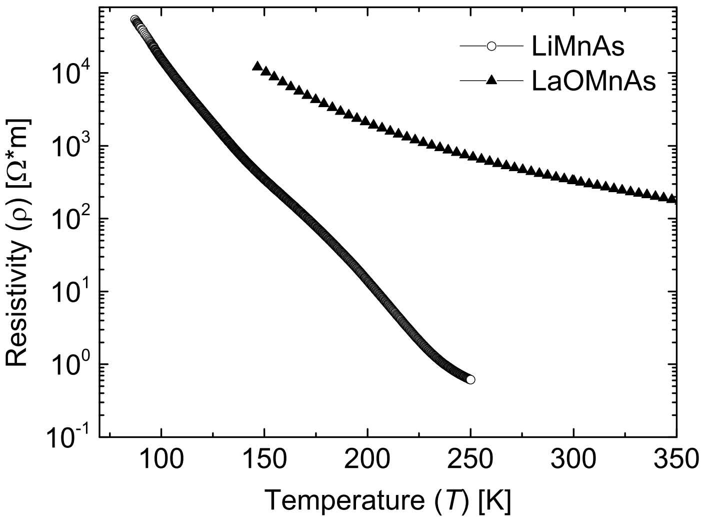

Figure 9.11: Temperature dependence of the electrical resistivity, $\rho(T)$, on a logarithmic scale for LiMnAs and LaOMnAs.

a value of approximately half of the band gap energy E_g for intrinsic semiconductors [66] according to the relation:

$$\sigma_{\mathrm{dc}} \propto \exp(-\frac{E_{\mathrm{g}}}{2k_{\mathrm{B}}T}), \tag{9.1}$$

where k_{B} = Boltzmann constant ($8.617332{\cdot}10^{-5}$ eV/K), T is the absolute temperature, and E_{g} is the band gap width. Figure 9.10 shows the Arrhenius plot and the temperature dependence of the conductivity measurements for LiMnAs and LaOMnAs.

In the resistivity measurements both samples show the same behavior, namely, two distinct sections of activated conduction with a small E_{g} of 0.20 eV for LiMnAs and an E_{g} of 0.18 eV for LaOMnAs, which indicate doped levels at lower temperatures and a larger E_{g} of 0.57 eV for LiMnAs and an E_{g} of 1.07 eV for LaOMnAs respectively, at higher temperatures. Figure 9.11 shows the resistivity as a function of temperature on a logarithmic scale. We note in particular, that the electrical resistivity changes by more than five orders of magnitude for LiMnAs in the temperature range of 100–250 K and by about two orders of magnitude for LaOMnAs from 150–350 K.

9.3.3 Dielectric permittivity

Ellipsometric measurements covering the far-infrared to deep-ultraviolet spectral range (10 meV–6.5 eV) were carried out at room temperature on LaOMnAs ceramic dense pellets polished to an optical grade finish. The complex dielectric function, $\tilde{\varepsilon}(\omega) = \varepsilon_1(\omega) + i\varepsilon_2(\omega)$ was directly determined from ellipsometric angles $\Psi(\omega)$ and $\Delta(\omega)$ [104]. The inversion of the ellipsometric data was performed within the framework of an effective medium approximation, which in the case of polycrystalline samples corresponds to the volume average of the anisotropic dielectric tensor projections. We did not take into account the surface roughness grain texturing effects on $\tilde{\varepsilon}(\omega)$, which is estimated to be less than 10% over the measured spectral range. Because of the air sensitivity, it was not possible to obtain ceramics of LiMnAs sufficiently dense for optical measurements.

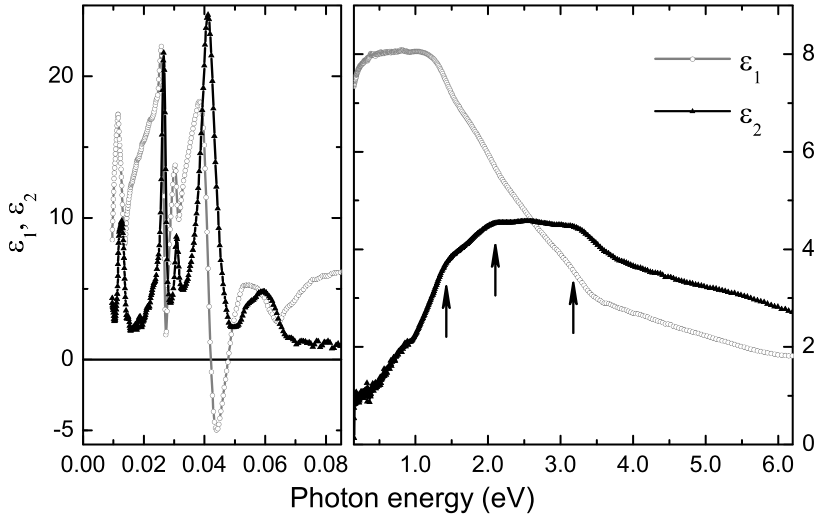

Figure 9.12: (Left) Phonon and (right) interband electronic contribution to the real and imaginary parts of the dielectric function $\tilde{\varepsilon}(\omega) = \varepsilon_1(\omega) + i\varepsilon_2(\omega)$ of LaOMnAs measured at $T = 294$ K. Arrows mark the peak positions of the main absorption bands.

Figure 9.12 shows the complex dielectric function of the LaOMnAs sample at $T = 294$ K. In the far-infrared range, there are six strong phonon modes. The lowest interband transition in this material lies above 0.4 eV. One can clearly distinguish three optical bands peaked at ~ 1.4, ~ 2.1, and ~ 3.2 eV.[105]. These transitions provide the main contribution to the static permittivity and form the direct absorption edge, below which the real part of the dielectric permittivity becomes nearly constant down to the phonon frequencies, $\varepsilon_1(0.2 \text{ eV} \lesssim \omega \lesssim 1.2 \text{ eV}) \approx 8$. We note that the main features resemble those that characterize the interband electronic contribution to the dielectric function of polycrystalline LaOFeAs, while shifted by ~ 0.7 eV to higher energy [105]. The rise of $\varepsilon_2(\omega)$ above 0.4 eV can be attributed to indirect interband transitions.

9.3.4 LiMnAs versus LaOMnAs

Regarding the magnetism of LaOMnAs, in Ref. [83], it was found that it is antiferromagnetically ordered in the *ab* plane, similar to LiMnAs, according to neutron diffraction analysis at lower temperatures. The small increase in the magnetic moments was explained [83] by a weak ferromagnetic behavior as a result of a small spin canting. Such canting could be caused by broken inversion symmetry, giving rise to the Dzyaloshinskii-Moriya [97, 98] interaction modifying the magnetic ground state, which ceases to remain collinear. However, in LiMnAs and LaOMnAs, the inversion symmetry break occurs anyway at their surfaces or interfaces.

Thus, in bulk LaOMnAs we would expect, that canting plays a negligible role. Instead of canting, we explain the small remanent total moment of these compounds with the formation of MnAs as an impurity phase. This is because during synthesis, independent of the method used, tiny amounts of MnAs ($\leq 1\%$) can easily be formed, which cannot be detected by techniques such as XRD or energy-dispersive X-ray spectroscopy (EDX).

As shown by the data in Table 9.2, MnAs is an ordered FM material. It has a Curie temperature of approximately 320 K [99] exactly coinciding with the magnetic transition temperature in our measurements. Thus, the presence of MnAs impurities in the samples offer a more straightforward explanation for the small remanent total moments reported in Ref. [83], rather than spin canting.
Regarding the non-Curie-Weiss-like behavior of the magnetization as a function of temperature reported for related $A\text{Mn}X$ compounds [86], our DFT calculations (see below) have shown that within the layers, the Mn moments are very strongly coupled relative to the weak interlayer couplings. Additionally, in LiMnAs between the layers, the Mn atoms are actually coupled ferromagnetically with their next nearest neighbors and antiferromagnetically with their second nearest neighbors. Because of this complex interaction between Mn moments, even above the Néel temperature, a short-range local order is present, causing the non-Curie-Weiss-like behavior described above.

9.4 DFT calculations

In order to gain further insights into the electronic structure and energetics of LiMnAs and LaOMnAs, we have performed *ab-initio* calculations based on the density functional theory (DFT) with the VASP [44, 45] code. For the approximate treatment of the electron exchange and correlation, we have used the Perdew, Burke, Ernzerhof (PBE) functional [46] together with the projector-augmented wave (PAW) method with a plane-wave cutoff energy of 400 eV. In the irreducible part of the Brillouin zone, the k-point integration was performed on an 8×8×4 Monkhorst-Pack mesh.

To describe the magnetic ordering in the compounds as found from neutron diffraction for the tetragonal antiferromagnetic structures, spin polarized calculations have been carried out for supercells containing four primitive unit cells (see Fig. 9.1).
In the case of LiMnAs, the calculated local Mn moments of 3.82 μ_B for the ground state are in excellent agreement with the value of 3.72 μ_B measured at 1.6 K, which is the most representative temperature for a comparison between experiment and theory. As already mentioned in the introduction, the magnetic moment of the Mn atoms is well localized in this class of materials. Based on a fully ionic picture of LiMnAs, i. e. Li^{+}, Mn^{2+}, As^{3-}, one would expect that the oxidation state of Mn to be 2^{+}.

The experimentally obtained value of 1.6^{+} from XANES measurements are somewhat lower than this 2^{+} expected value. Therefore, we have looked into the real-space density of LiMnAs, and apart from the expected sp^3 hybridization between Mn and As (see left panel in Fig. 9.13), we found that there is also a feature present that corresponds to a mixture between Mn–Mn bonds and Mn–As bonds (see right panel in Fig. 9.13).

From subsequent DFT calculations, we have determined the magnetic exchange coupling constants J_{ij} of the classical Heisenberg model, $H = -\sum_{i>j} J_{ij}\hat{\mathrm{e}}_i\hat{\mathrm{e}}_j$, where $\hat{\mathrm{e}}_{i,j}$ are the unit vectors corresponding to the directions of the local magnetization at sites i and j. For this purpose, we have employed the SPR-KKR program package [47] which is a suitable numerical tool for such computational task, not relying on pseudopotentials, where J_{ij} can be evaluated within the Green's function formalism. As it follows from analysis of the exchange coupling scheme (see Fig. 9.14), within each Mn plane, the magnetic moments of the nearest neighbors are coupled antiparallel (with $J_1 \approx -60$ meV, shown in red), and this strong antiparallel coupling cannot be perturbed by the competing but smaller next-nearest neighbor antiparallel interaction ($J_2 \approx -14.7$ meV, shown in dark-red). Thus, within each plane the nearest Mn magnetic moments are ordered antiferromagnetically. Further, to understand

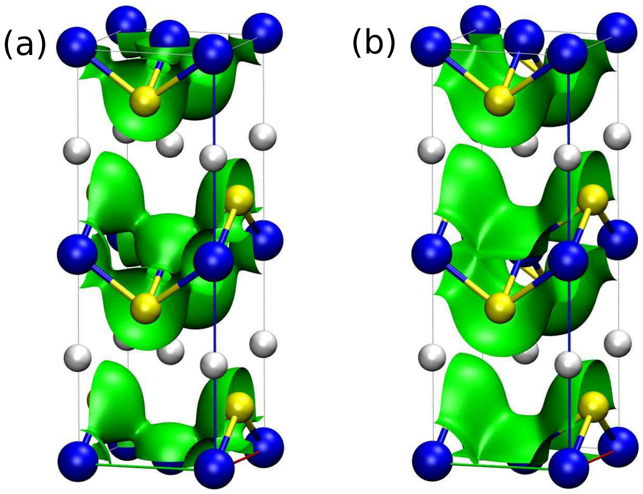

Figure 9.13: Real space electronic density of LiMnAs. The density as green surfaces superimposed on top of the atomic structure at isovalues of $5.96 \cdot 10^{-3}$ and $3.58 \cdot 10^{-3}$ $e/\text{Å}^3$, corresponding (a) to sp^3 hybridization and (b) to a mixture between Mn–As and Mn–Mn bonding.

how the nearest planes are magnetically oriented to one another, we consider the inter-plane exchange coupling. Both leading constants of the inter-plane exchange are positive, $j_{1,2} \approx 0.6$ and 0.24 meV, which correspond to the nearest and next-nearest inter-plane interactions, respectively. It is easy to see that for an already fixed in-plane magnetic order, these two interactions are also competing. Despite the fact that $j_1 > j_2$, each Mn atom (for simplicity we consider one in the center of Fig. 9.14) has only 2, but 8 next-nearest inter-plane neighbors, which leads to an overall domination of the next-nearest inter-plane coupling ($8j_2 > 2j_1$); thus, the next-nearest Mn planes are coupled antiferromagnetically.
Based on the Mulliken analysis, the corresponding partial charges, i. e., oxidation numbers of Li, Mn, and As were computed as +0.8, +1.5, and −2.3, respectively. This is again in good agreement with the XANES measurement presented above, where an oxidation state of 1.6 was determined for the Mn atom in LiMnAs.

For LiMnAs, in our calculations we found an indirect band gap of 0.55 eV (see Fig. 9.15 (a)), which is very close to the 0.57 eV gap estimated from the higher temperature range of the Arrhenius plot of the conductivity measurements given in the previous sections. These results are also in a good agreement with the recent full potential calculations for bulk LiMnAs, where within the local density approximation (LDA) a Γ-M indirect gap of approximately 0.5 eV [76] was computed.
As already shown, at 768 K LiMnAs undergoes a phase transition to the cubic crystal

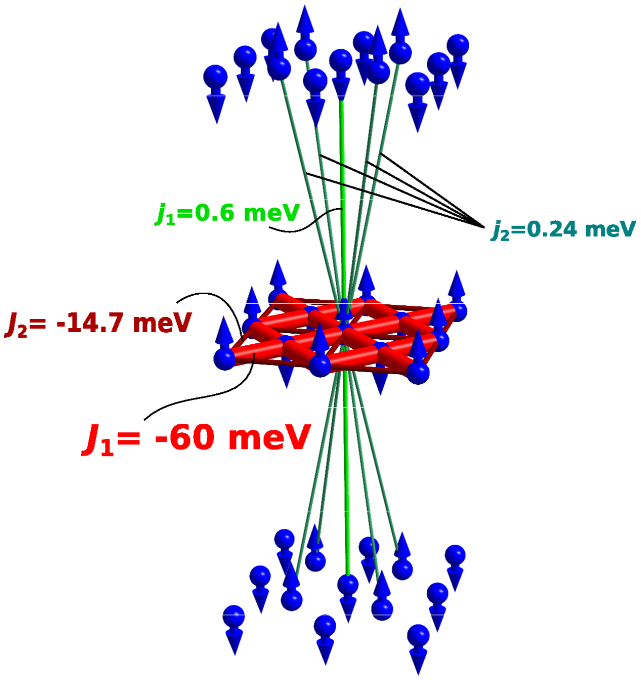

Figure 9.14: The scheme of the leading magnetic exchange interactions within the Mn atomic planes and between the nearest Mn atomic planes of LiMnAs. For clarity, only Mn atoms are shown (blue spheres) and the orientations of the magnetic moments are depicted with arrows. The thickness of the bonds connecting interacting atoms are roughly proportional to the strength of the corresponding exchange interactions, where antiferromagnetic and ferromagnetic coupling is represented by red ($J_{1,2}$) and green ($j_{1,2}$) colors, respectively.

system. Due to computational limitations and difficulties from the perspective of the methodology, the implicit treatment of temperature effects in *ab-initio* calculations is not straightforward.

Therefore, for the study of the cubic phase we have assumed, that the Mn atoms are ordered antiferromagnetically as in the tetragonal phase. Using this model, our calculations indicate, that in contrast to the tetragonal phase, the cubic structure has a direct band gap of 0.84 eV. By comparing the computed total energies of the tetragonal and cubic phases, we found that the cubic phase is only 24 meV higher in energy per formula unit than the tetragonal phase. Thus, although the tetragonal structure is the ground state, the tetragonal-to-cubic phase transition can easily

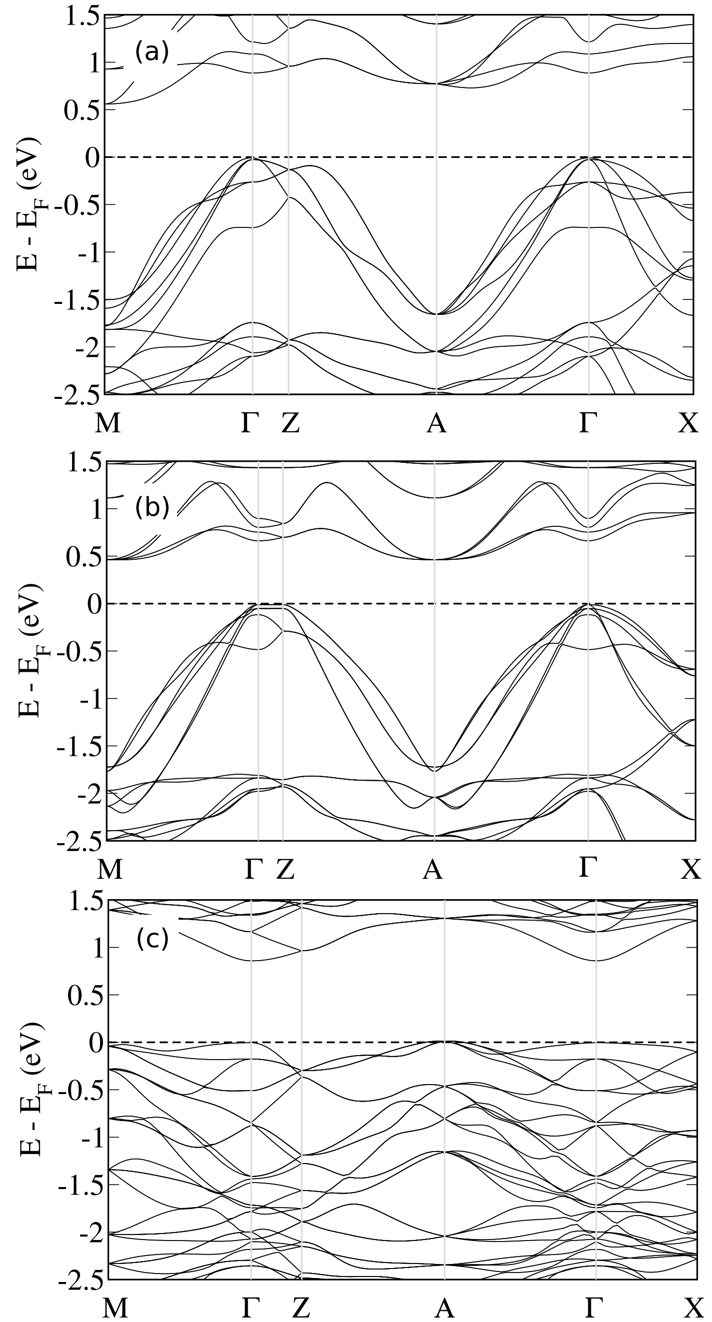

Figure 9.15: Electronic band structure of tetragonal antiferromagnetic LiMnAs (a) and LaOMnAs (b). In (c) the band structure of the cubic phase of LiMnAs is shown. Spin-orbit coupling was not accounted.

take place. This is because the two phases are rather close in energy, and the energy difference of 24 meV is lower than the 75 meV thermal energy of the system at 768 K, which means that the system can easily surmount the energy difference of 24 meV.

Hence, there is good agreement between the theoretically estimated energy difference and the experimentally measured 23 meV/f.u. change in enthalpy, which justifies the use of the simplified theoretical model. Our calculations suggest that AFM ordering dominates in LiMnAs so strongly, to the extent that even if LiMnAs could be synthesized in the cubic phase, the pure undoped compound would still be an AFM semiconductor.

In the case of LaOMnAs, the theoretical local moments as obtained with the PBE functional for the Mn atoms are 3.54 μ_B. In contrast to these results, via neutron diffraction measurements performed at 290 K, the refined magnetic moment of Mn was 2.43 μ_B, which is more than one μ_B lower compared to our theoretical result. In a later experiment [89] however, it was shown that the moments at 2 K are 3.34 μ_B, which is in good agreement with our calculations. In the case of LiMnAs, our neutron-diffraction data also show a similar trend as a function of temperature, where at 300 K the Mn moments are reduced from 3.72 to 2.62 μ_B (see Table 1). Furthermore, in case of the structurally closely related $\mathrm{BaMn_2As_2}$ the Mn local moments were determined [106] to be 3.88 μ_B at 10 K. Hence, the magnetic properties and magnetic moments are rather similar in the whole family of the AMnAs (A = Li, LaO, Ba, etc.) layered structure type.

The computed oxidation state of the La, O, Mn, and As atoms are +2.4, -0.8, +1.4, and -3.1, respectively, i. e., the oxidation state of O is underestimated, and that of As is overestimated. Regarding the electronic structure, we found that LaOMnAs is also an indirect band-gap semiconductor with an E_g of 0.46 eV (see Fig. 9.15 (b)), which is considerably lower than the value of 1.07 eV derived from the Arrhenius plot.

9.5 Summary

In summary, it has been presented, a broad overview of the synthesis, atomic and electronic structure, and magnetic properties of LiMnAs, LaOMnAs, and other related compounds in the AMnX family. Thus, with this work, we respond to several important questions raised concerning this important class of materials. In general, the compounds in the AMnX family can be classified in two main categories: AFM semiconductors and FM metals. The nature of the magnetic coupling and of the semiconducting or metallic behavior is mainly determined by the shortest Mn–Mn distances ($d_\mathrm{Mn-Mn}$), which seems to be a general property of the compounds containing MnAs layered networks.

For LiMnAs and LaOMnAs, our data are in good agreement with the literature, showing that both are antiferromagnetic semiconductors, with a magnetic moment of ca. 4 μ_B per Mn atom at low temperatures. Interestingly, by combining thermal analysis and temperature dependent XRD measurements, a phase transition to the cubic Half-Heusler phase has been discovered. Theoretical calculations suggest that even if cubic LiMnAs could be stabilized, the ideal undoped cubic counterpart would still be an AFM semiconductor, similar to the tetragonal compound. EXAFS and XANES measurements indicate the oxidation state of Mn to be 1.6. This is in agreement with the concept of localized moments on Mn and explains the close relationship between the cubic and tetragonal phase and the connection between Mn and rare earth ions in tetragonally coordinated structures. Regarding the weak ferromagnetism, in contrast to Refs. [83, 89], due to symmetry considerations, we expect that canting takes place at the surfaces and interfaces of LiMnAs and LaOMnAs, but in the bulk it is unlikely.

Resistivity measurements on LiMnAs and LaOMnAs show two distinct regions of activated transport behavior, and a large change in resistivity by more than five and two orders of magnitude, respectively. Furthermore, we have shown that LaOMnAs is also a promising material for the realization of spin valves [107] and our findings suggest that compounds such as $BaMn_2As_2$ and related compounds are promising candidates as well.

10 LiCuS: A potential environment-friendly battery and solar cell material

10.1 Introduction

The text of this chapter contain text passages identical with the following submitted publication:

A. Beleanu, J. Kiss, M. Baenitz, M. Mayunder, A. Senyshyn, G. Kreiner and C. Felser *LiCuS, an Intermediate Phase in the Electrochemical Conversion Reaction of CuS with Li,: a Potential Environment-friendly Battery and Solar Cell Material*
in preparation

Nowadays lithium batteries are playing a major role in mobile electronics applications, being mass produced in an industrial scale for mobile phones, laptops and other gadgets. In the near future it is expected, that electric cars will run with lithium batteries instead of fossil fuels, and large capacity lithium-ion accumulators will provide temporary storage for renewable energy applications like solar cells and wind turbines. Hence, lithium based compounds have widely been investigated in order to obtain new electrode materials for all the batteries systems: primary, secondary or rechargeable batteries [108–113].

The Li-S battery system has been investigated for several decades because its high theoretical specific energy density is much greater than those of the conventional lithium batteries [114]. An alternate class of cathode materials are 3d-transition metal sulfides because they combine high capacities and reversibility even after prolonged charge-discharge cycling. Although there are a large number of compounds which are now studied, there is an immense interest to develop alternative materials with higher energy densities at lower costs [115, 116]. Cu_2S for example is not only a promising cathode material but it is also very attractive for various applications like optoelectronic devices [115, 116], solar cells [117, 118] and other types of batteries [119]. CuS is specifically interesting due to its high specific capacity and its good electronic conductivity [120–122] .

The latter compound and the corresponding conversion reaction mechanism CuS + 2Li = Li_2S + Cu has been investigated several times in the past [123–130] and recently by X-ray diffraction and solid-state NMR spectroscopy [123]. It has been found that the conversion reaction of CuS and Li is rather complex and involves the formation of an intermediate phase Li_xCuS with x close to 1. CuS inserts in the first step of the process a small amount of Li forming the terminal solid solution phase Li_xCuS with x = 0.16. The latter reacts then with more Li to the intermediate phase $Li_{\backsim 1}CuS$. Li_2S has been observed to form in significant quantities together with small Cu particles starting from x = 0.85. Therefore, the second step of lithiation is given by the reaction LiCuS + Li = Li_2S + Cu. A small amount of $Cu_{1.96}S$ has been found in fully discharged samples, which was explained by a decomposition of $Li_{\sim 1}CuS$ [123].

Recently, it was suggested that LiCuS is a suitable substitute for the CdS buffer layer in conventional chalcopyrite-based thin film solar cells [18]. CdS is harmful to the environment and costly, so there is a strong demand for alternative buffer layer materials [1]. Thin films of LiCuS have been prepared by radio-frequency sputtering using a target with a 1:1:1 ratio of Li, Cu, and S. A target with a brownish surface has been obtained by hot sintering fine powders of Cu_2S and Li_2S at about 870 K and 22 MPa. The sputtered films on glass turned out to be transparent with a yellow color corresponding to a band gap between 2.0 and 2.5 eV. Unfortunately, it was not possible to analyze the exact composition of the film, but one can assume a composition close to the intermediate phase of the CuS/Li conversion process.

The main objective of this work is the bulk synthesis of the yellow phase, close to the composition LiCuS, and the determination of its composition and crystal structure by powder diffraction techniques and ^7Li solid-state NMR.

10.2 Experimental details

10.2.1 Synthesis of LiCuS, based on Li and CuS

Polycrystalline $Li_{\backsim 1}CuS$ was synthesized by the reaction of Lithium foil (99.999%) and CuS powder (anhydrous, 99.999%), both from Sigma Aldrich, close to the 1:1:1 stochiometry, but with a small amount of Li in excess. A mixture of the starting materials was pressed into pellets and placed in Al_2O_3 tubes (Φ = 14 mm, Al23, Friatec). The total mass was approximately 1 g per sample. Each crucible was

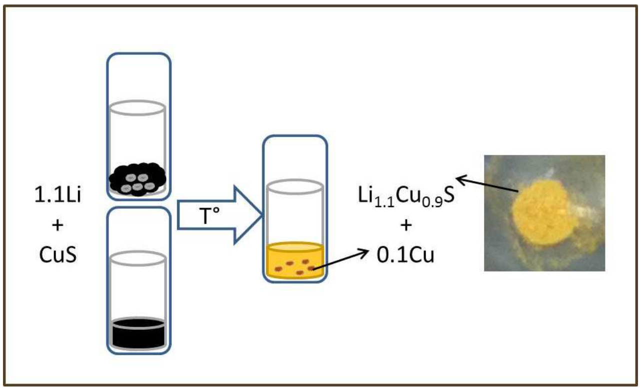

Figure 10.1: Synthesis of LiCuS from Lithium foil and CuS powder. The mixture of the starting materials was weighed and placed in Al_2O_3 tubes. After heating the mixture a yellow polycristalline powder and metallic Cu was obtained.

jacketed by an evacuated fused silica ampoule. All handling has been performed in a glove-box using Ar (p (O_2, H_2O) $\leq$ 1 ppm) as protecting atmosphere. The heat treatment used was as follows. After increasing the temperature of the mixture to 723 K with a heating rate of 1 K/min, the temperature was hold at 723 K for 96 h and then reduced to room temperature with a cooling rate of 1 K/min. After the reaction, a yellow, air and moisture sensitive powder was obtained. Optical microscopy revealed small Cu particles as a second phase.

The chemical reaction is given by the following equation:

$$CuS + 1.1Li = Li_{1.1}Cu_{0.9}S + 0.1Cu \tag{10.1}$$

The synthesis has been several times repeated in order to clear the reproducibility of the products. A very important observation is that the heating temperature has to be very precise, because any change can influence the product. The same observation has also been made if the Lithium amount deviates from the inital weight. In addition, the obtained yellow powder is extremely air and water sensitive. After a short time in the glovebox the yellow powder becomes brownish at the surface.

10.2.2 Synthesis of LiCuS based on Li_2S and Cu_2S

Another method to synthesize LiCuS is based on the chemical reaction of Li_2S with Cu_2S, namely:

$$0.5Li_2S + 0.5Cu_2S = LiCuS \tag{10.2}$$

Polycrystalline samples of $Li_{2-x}Cu_xS$ (with x = 0.1, 0.3, 0.5, 0.7, 0.9, 1) were obtained by solid state reaction, weighing in stoichiometric amounts Li_2S (99.999%, Sigma Aldrich) and Cu_2S (99.999%, Sigma Aldrich) both in powder form. The mixed powders were filled into Al_2O_3 tubes (cleaned before at ca. 1500 K). The total mass was approximately 1 g per sample. Each crucible was jacketed by an evacuated fused silica ampoule and was placed in an muffle-type furnace at 773 K for 96 h. The heating and cooling rate were fixed at 1 K/min. After the heating, and depending of the chosen target stoichiometry, colored powders were obtained. All of the handling was performed in a glove-box under Ar ($p(O_2,H_2O) \leq$ 1ppm).

10.3 Structural characterization

10.3.1 Discussion on the Li-Cu-S intermediate phase

The sample has been characterized by powder X-ray diffraction (Huber Gunier G670, flat sample holder using Kapton foils, Cu $K\alpha_1$) and powder neutron diffraction measurements. Two dimensional powder diffraction data were collected at 4 K and 300 K and then corrected for geometrical aberrations and curvature of the Debye-Scherrer rings as described in [41]. The measurements performed at different temperatures reveal that the sample remained isostructural in the temperature range from 4 - 300 K. The powder patterns have been indexed using Werner's algorithm [131]. The crystal structure has been solved with Expo2013 [132] and refined with Jana2006 [96]. Intensity versus 2θ plots of the observed and calculated neutron powder pattern are shown in Fig. 10.2. It was possible to observe the elemental Cu as small particles using an optical microscope. Moreover, the Bragg reflections of Cu are clearly distinguished from that of the main phase in the X-ray and neutron powder diffraction patterns. The refined phase fraction (5 wt % Cu) is also in good agreement with the fraction (7 wt %) calculated from the refined composition. Finally, the formation of Li_2S according to the chemical reaction, LiCuS + Li = Li_2S + Cu, was not observed. One Bragg reflection of low intensity (see the first Bragg reflection of the powder patterns in Fig. 10.2 could not be assigned to either the title compound or elemental Cu. This peak originates from a new phase ($\leq$ 1 wt %) with dark gray or black color and probably forms in the CuS/Li electrochemical conversion process with slightly less Li content than the title compound.

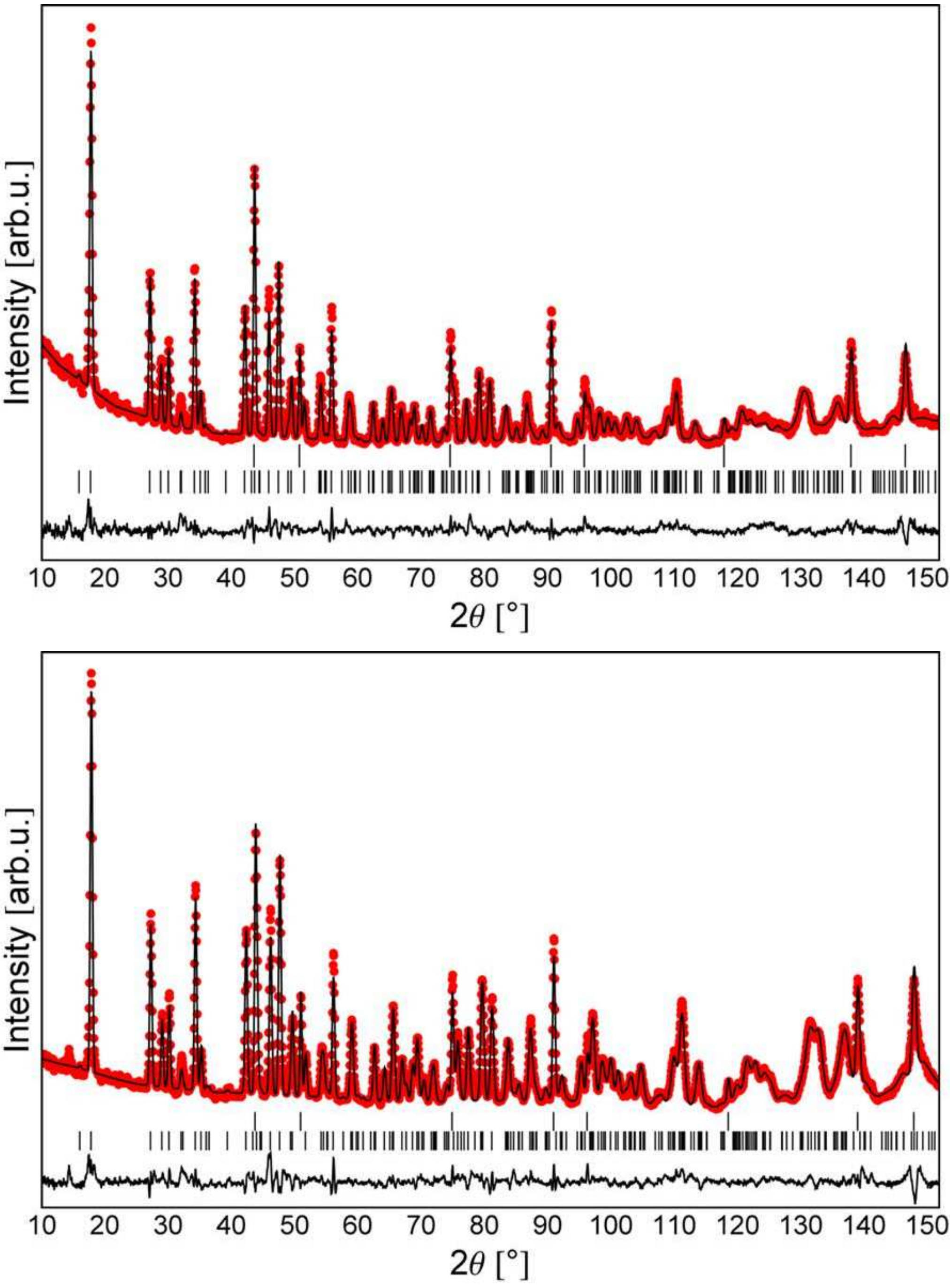

Figure 10.2: Intensity versus 2θ plot of observed and calculated neutron powder pattern, Bragg reflection marker and plot of difference curve at 293 K (top panel) and at 4 K (bottom panel) for $Li_{1.1}Cu_{0.9}S$.

Table 10.1: Crystal data and Rietveld refinement results for Li$_{1.1}$Cu$_{0.9}$S and Cu.[1] For the measurement at room temperature the lattice parameters and errors of Guinier data calibrated with LaB$_6$ has been used and the wavelength has been refined. For the measurement at 4 K the wavelength obtained from the refinement at 293 K has been used and the lattice parameters have been refined. the errors at 4K are estimated using Berar's formula.

Sample composition	1.12(2)Li + 1.07(2) Cu + 1S	
Sample colour	yellow	
Phases in sample	95 wt.% Li$_{1.1}$Cu$_{0.9}$S + 5 wt.% Cu	
Probe[1], wavelength, λ (Å)	neutron	
Neutron scattering length (10^{12} cm)	b(Li) = -1.900, b(Cu) = 7.718, b(S) = 2.847	
Container type, size	vanadium can, Ø 10 mm, 1 = 60 mm	
Absorption correction, μr	cylindrical sample, 1	
Background	Manual back.- 10 Legendre polynomials	
Profil function	gaussian	
Temperature, T (K)	293	4
R_p, R_wp, R_wp expected	0.0279, 0.0364, 0.0159	0.0309, 0.390, 0.0144
Goodness of fit, S	2.29	2.71
Li$_{1.1}$Cu$_{0.9}$S		
Chemical formula, Z	Li$_{1.1}$Cu$_{0.9}$S, 8	
Formula weight, M (g/mol)	96.89	
Crystal system	orthorhombic	
Space group, No.	*Ibam*, 72	
Unit cell dimensions[1] (Å)	$a = 5.632(1)$	$a = 5.6150(7)$
	$b = 11.209(3)$	$b = 11.1325(14)$
	$c = 5.982(2)$	$c = 5.9644(8)$
Unit cell volume, V ($\mathring{A}^3$)	377.6(2)	372.8(1)
Calculated density, D_{cal} (gcm^{-3})	3.4051	3.4571
Absorption coefficien, μ (mm-1)	0.15	
2θ range (°), step size	10 - 151.9, 0.05	
RF_{all}, RF_{wall}	0.0644, 0.0667	0.0391, 0.0443
Number of parameter / constraints	33 / 4 / sigma	
Weighting, Shift / sigma in last cycle	sigma, < 0.01	
Cu		
Chemical formula, Z	Cu, 4	
Crystal system	cubic	
Space group, No.	*Fm*-3*m*, 225	
Unit cell dimensions[1] (Å)	$a = 3.6154$	$a = 3.6026(2)$
RF_{all}, RF_{wall}	0.0606, 0.0667	0.0391, 0.0443

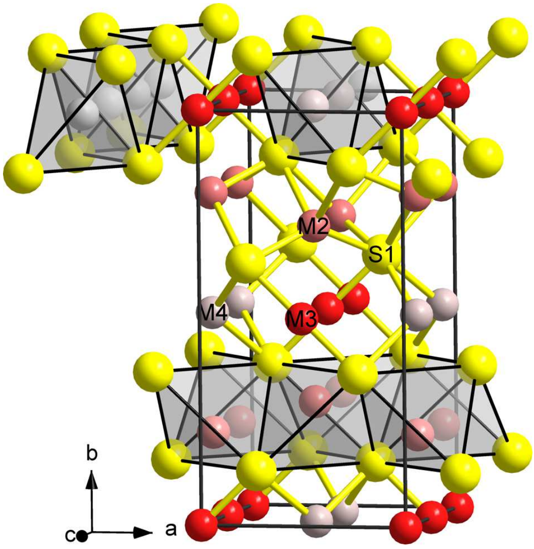

Figure 10.3: Crystal structure of $Li_{1.1}Cu_{0.9}S$. The metal sites, M, are occupied by randomly mixed Li and Cu atoms. The $M2$ site shows a slight site-occupation preference for Li atoms ($Cu_{0.41}$,$Li_{0.59}$). The $M3$ ($Cu_{0.88}$,$Li_{0.12}$) and $M4$ site ($Cu_{0.09}$,$Li_{0.91}$) a strong preferential site occupation for Cu and Li atoms, respectively.

The compound crystallizes orthorhombic with a new crystal structure type in space group *Ibam* (No. 72) with a = 5.632(1) Å, b = 11.216(2) Å and c = 5.9982(2) Å. Crystal data and Rietveld refinements results for $Li_{1.1}Cu_{0.9}S$ and Cu are given in Table 10.1. The atomic coordinates and isotropic displacement parameters at 293 K are listed in Table 10.2 and the interatomic distances in Table 10.4. The crystal structure is shown in Fig. 10.3 and the coordination-type polyhedron are shown Figure Fig. 10.4. There are 24 atoms per unit cell, occupying four different crystallographic sites. S occupies $8j$ ($S1$), and the remaining metals, Li and Cu $8g$ ($M2$), $4c$ ($M3$) and $4b$ ($M4$). All the metals sites are occupied by randomly mixed Li and Cu atoms. The $M2$ site shows a slight site-occupation preference for Li atoms ($Cu_{0.41}$,$Li_{0.59}$), whereas $M3$ ($Cu_{0.88}$,$Li_{0.12}$) and $M4$ ($Cu_{0.09}$,$Li_{0.91}$) sites show a strong preference for Cu and Li atoms, respectively. The S atoms are surrounded by seven metal atoms ($SLi_{2.7}Cu_{4.3}$). Its coordination-type polyhedron can be derived from a distorted cube. Herein, one edge of the cube was omitted, and the two corresponding metal atoms were replaced by an atom ($M3$) located at the midpoint of the former cube edge. The distances S-M, range from 2.129 Å to 2.641 Å. The coordination-type polyhedron of $M2$ is a distorted $M2S4$ tetrahedron with the $M2$-S distances, 2.315 Å and 2.641 Å. The $M3$ site forms a dipole, i.e., it is linearly

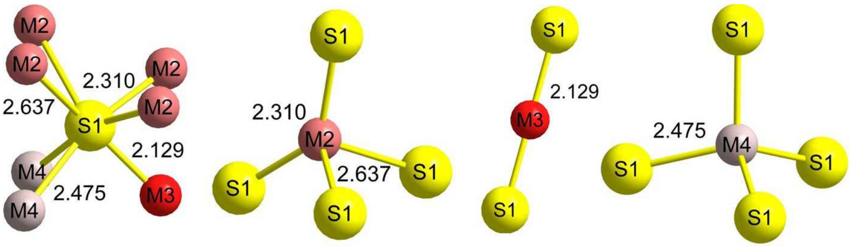

Figure 10.4: Atomic environments for the four different crystallographic sites of $Li_{1.1}Cu_{0.9}S$ at 293 K with distances.

coordinated by two S atoms (M3S2) and the distance $M3$-S is 2.129 Å. Such a distance is rather short but, still physically reasonable. Distances in the range from 2.1 to 2.2 Å have been reported for several phases with fully occupied sites for Li-S as well as for Cu-S in Pearsons Crystal Data Bank [133]. The unit cell volume of $Li_{1.1}Cu_{0.9}S$ is contracted by about 1.4% at 4 K compared to room temperature. However, the short distance, $M3$-S, remains constant within error margins in this temperature range, while longer distances become significant smaller (Table 10.4). This indicates that a distance between 2.1 Å and 2.2 Å is a lower limit for the contacts between Cu, Li and S. The coordination polyhedron of the $M4$ site is a nearly regular $M4S_4$ tetrahedron with d($M4$-S) = 2.470 Å.

The crystal structure can be described as an alternate stacking of two different types of layers along the b axis as shown in Fig. 10.3. The first layer is composed of $M2S_{4/4}$ tetrahedra, which are joined via four of their edges. The resulting composition of this layer is $(Cu_{0.41},Li_{0.59})S$. This type of edge-sharing layer is known from the structure of red PbO with oxygen at the tetrahedron centers and Pb at the vertices. The Li_2S structure with anti-CaF_2 structure type is a three-dimensional network of edge-sharing LiS_4 tetrahedra, i.e., the structure was obtained by stacking $LiS_{4/4}$ layers along the remaining direction. The second type of layer was obtained by connecting the linear chains of composition $(Cu_{0.09},Li_{0.91})S_{4/2}$ via linearly coordinated $M3$ $(Cu_{0.88},Li_{0.12})$. The chains were formed by $M4S_4$ tetrahedra, which are linked via opposite edges. These tetrahedra share edges with the tetrahedra of the $M2S_{4/4}$ layers. In total, the $M2S_{4/4}$ share edges with five neighboring and the $M4S_{4/2}$ with four neighboring tetrahedra. The maximum number of six edge-sharing tetrahedra is found in the CaF_2 structure type.

An idealized crystal structure of $Li_{1.1}Cu_{0.9}S$ can be derived from the cubic Li_2S structure with a = 5.716 Å as shown in Fig. 10.5. On the left side a unit cell of the Li_2S structure with anti-CaF_2 structure type is shown in an unconventional setting, highlighting the arrangement of the SLi_8 cubes. Lowering the symmetry

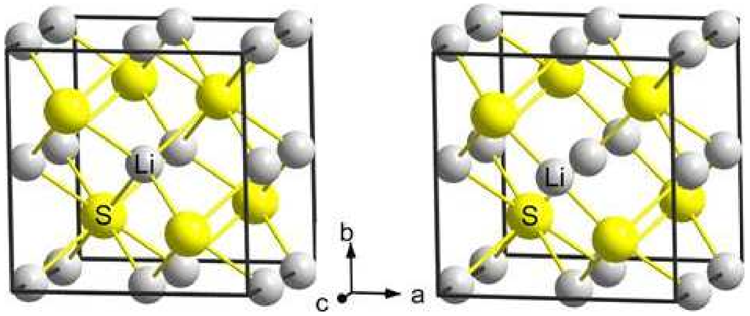

Figure 10.5: (left) Crystal structure of Li_2S (a = 5.716 Å, $Fm-3m$, anti-CaF_2 structure type) in unconventional setting emphasizing the atomic environment of S. (right) Hypothetical crystal structure of Li_2S ($P4_2/mcm$), showing the same structural features of $Li_{1.1}Cu_{0.9}S$. The structure was obtained by moving Li from sites $\frac{1}{2}$, $\frac{1}{2}$, $\frac{1}{4}$ to $\frac{1}{2}$, $\frac{1}{2}$, 0.

Table 10.2: Atomic coordinates and isotropic displacement parameters for $Li_{1.1}Cu_{0.9}S$ at 293 K.

Atom	Wyckoff symbol	S.O.F.	x	y	z	U_{iso} ($Å^2$)
S1	$8j$	1	0.2703(5)	0.1328(3)	0	0.019(3)
Cu2	$8g$	0.417(4)	0	0.2116(4)	$\frac{1}{4}$	0.041(2)
Li2	$8g$	0.583	0	0.2116	$\frac{1}{4}$	0.041
Cu3	$4c$	0.873(8)	0	0	0	0 0.026(7)
Li3	$4c$	0.127	0	0	0	0.026
Li4	$4b$	0.911(4)	$\frac{1}{2}$	0	$\frac{1}{4}$	0.018(3)
Cu4	$4b$	0.089	$\frac{1}{2}$	0	$\frac{1}{4}$	0.018

from $Fm\overline{3}m$ to $P4_2/mcm$ allows moving the central chain of Li atoms by 1/4 c, i.e., the Li atom at the crystallographic site $\frac{1}{2}$,$\frac{1}{2}$,$\frac{1}{4}$ moves to $\frac{1}{2}$,$\frac{1}{2}$,0. This idealized structure shows already all the important features of the structure of $Li_{1.1}Cu_{0.9}S$. The S atoms have coordination number 7. Two Li atoms per unit cell are linearly coordinated by S such as $M3$, and the two remaining Li positions are tetrahedrally coordinated by S, comparable to $M2$ and $M4$. Then, the doubling of the b axis to $2b$ and a body-centered arrangement allow the distances of the structure to be optimized with respect to the chemical composition. This was achieved by puckering the metal atoms ($M2$) in the a - c plane and by a slight change of the unit cell parameters.

Selected interatomic distances are given in Table 10.4.

Table 10.3: Atomic coordinates and isotropic displacement parameters for $Li_{1.1}Cu_{0.9}S$ at 4 K.

Atom	Wyckoff symbol	S.O.F.	x	y	z	U_{iso} (Å^2)
S1	$8j$	1	0.2736(14)	0.1328(8)	0	0.012(2)
Cu2	$8g$	0.424(10)	0	0.2137(7)	$\frac{1}{4}$	0.008(3)
Li2	$8g$	0.576	0	0.2137	$\frac{1}{4}$	0.0008
Cu3	$4c$	0.87(2)	0	0	0	0 0.0103(15)
Li3	$4c$	0.13	0	0	0	0.0103
Li4	$4b$	0.911(10)	$\frac{1}{2}$	0	$\frac{1}{4}$	0.002(7)
Cu4	$4b$	0.089	$\frac{1}{2}$	0	$\frac{1}{4}$	0.002

Table 10.4: Selected interatomic distances for $Li_{1.1}Cu_{0.9}S$ at 293 K and 4 K.

Atom 1	Atom 2	Number	distance (Å) at 293 K	distance (Å) at4 K
S1	M3	1 x	2.129(3)	2.133(8)
S1	M2	2 x	2.310(3)	2.322(7)
S1	M4	2 x	2.475(3)	2.455(7)
S1	M2	2 x	2.637(4)	2.600(9)
M2	S1	2 x	2.310(10)	2.322(7)
M2	S1	2 x	2.637(4)	2.600(9)
M3	S1	2 x	2.129(3)	2.133(8)
M4	S1	4 x	2.475(3)	2.455(7)

10.3.2 Chemical reaction of Li_2S and Cu_2S

The yellow phase $Li_{1.1}Cu_{0.9}S$ has been obtained by reducing CuS with elemental Li. Due to the off-stoichiometry a mixture of Cu and $Li_{1.1}Cu_{0.9}S$ is the final product. Because Cu_2S is a stable compound, it should be possible to obtain a mixture of the black, unknown phase of approximate composition $Li_{\approx 0.5}CuS$ and the yellow phase $Li_{1.1}Cu_{0.9}S$ at the general composition LiCuS. This would prove that a compound at the composition LiCuS is not stable against decomposition into the black and the yellow phase at elevated temperatures.

For the reaction of Li_2S and Cu_2S a fine mixture has been obtained by grinding Li_2S and Cu_2S in an agate mortar. Table 10.6 lists the starting composition of various mixstures, the elemental content from the ICP results and the type of phase after the reaction at 723 K for 96 h. Chemical analysis for non-metal impurities were carried out using the carrier gas hot extraction or the combustion technique (TCH 600, C 200 (LECO ®)). For all samples, the impurities were below the limit of detection (LOD in ppm): H(100), N(200), O(1000) and C(1500) based on 50 mg initial weight. The target composition was checked by Inductively-Coupled-Plasma-Optical Emission Spectrometry (ICP-OES; Vista RL, Varian). Results of phase analysis are listed in Table 10.6. The samples obtained by this synthesis route have different colors. The yellow phase, $Li_{1.9}Cu_{0.1}S$, has been also detected but also a black unknown phase so far. Each compound from this series was investigated by mean of PXRD using Cu $K\alpha_1$ radiation of $\lambda = 1.5406$ Å in Debye-Scherrer geometry. Mixtures of the yellow and the black phase and some $(Li,Cu)_2S$ could be obtained after heat treatment at 500 °C for 96 h from Cu_2S and Li_2S mixtures in various ratios. Thus, all the experimental data support the off-stoichiometric formation of the yellow phase without perceptible homogeneity range. However, it was not possible to obtain two-phased samples of yellow phase with $(Li, Cu)_2S$ or with the black unknown phase. From $Li_{1.1}Cu_{0.9}S_{\approx 1}$ to $Li_{1.7}Cu_{0.3}S_{\approx 1}$ the PXRD measurements show a mixture of three phases: the orthorhombic yellow phase, $Li_{1.1}Cu_{0.9}S$, a cubic phase, a derivation of the cubic Li_2S structure and an unknown phase, for which the structure could not be solved until now. From $Li_{1.7}Cu_{0.3}S_{\approx 1}$ to Li_2S the Bragg reflexes in the XRD pattern can easily be indexed. This compounds crystallize in the cubic crystal system, $F\bar{4}3m$ (No. 216) similar to the Half-Heusler compounds. All the crystallographic data obtained after the Rietveld refinement on the XRD powder patterns are summarized in Table 10.5. Figure 10.6 displays on the left side, the PXRD pattern of $Li_{1.7}Cu_{0.3}S_{\approx 1}$, $Li_{1.9}Cu_{0.1}S_{\approx 1}$ and Li_2S, and on the right side the temperature dependence of the lattice parameter a.

The atomic parameters for $Li_{2-x}Cu_xS$, for x = 1.7, 1.9 are shown in Table 10.7.

Table 10.5: Crystallografic data and Rietveld refinement results for $Li_{1.7}Cu_{0.3}S$ and $Li_{1.9}Cu_{0.1}S$

Formula	$Li_{1.7}Cu_{0.3}S$	$Li_{1.9}Cu_{0.1}S$
a	5.676(3) Å	5.695(3) Å
V	182.89 Å^3	184.77 Å^3
Z	4	4
Space group	$F-43m$ (no.216)	$F-43m$ (no.216)
d_{calc}	2.285 g/cm^3	1.855 g/cm^3
Radiation	1.5406 Å	1.5406 Å

Table 10.6: Atomic procent of the studied elements obtained by chemical analysis

Starting compound	Elemental content (ICP)	Type of phase
$Li_1Cu_1S_1$	$Li_{1.00}Cu_{0.99}S_{1.00}$	Mixture of yellow orthorhombic phase $Li_{1.1}Cu_{0.9}S_1$ black unknown $Li_{2-x}Cu_xS$ and cubic phase Li_2S
$Li_{1.1}Cu_{0.9}S_1$	$Li_{0.98}Cu_{1.03}S_{0.98}$	
$Li_{1.3}Cu_{0.7}S_1$	$Li_{1.29}Cu_{0.73}S_{0.98}$	
$Li_{1.5}Cu_{0.5}S_1$	$Li_{1.46}Cu_{0.57}S_{0.96}$	
$Li_{1.7}Cu_{0.3}S_1$	$Li_{1.73}Cu_{0.30}S_{0.96}$	Cubic $Li_{2-x}Cu_xS$
$Li_{1.9}Cu_{0.1}S_1$	$Li_{1.94}Cu_{0.10}S_{0.96}$	Cubic $Li_{2-x}Cu_xS$

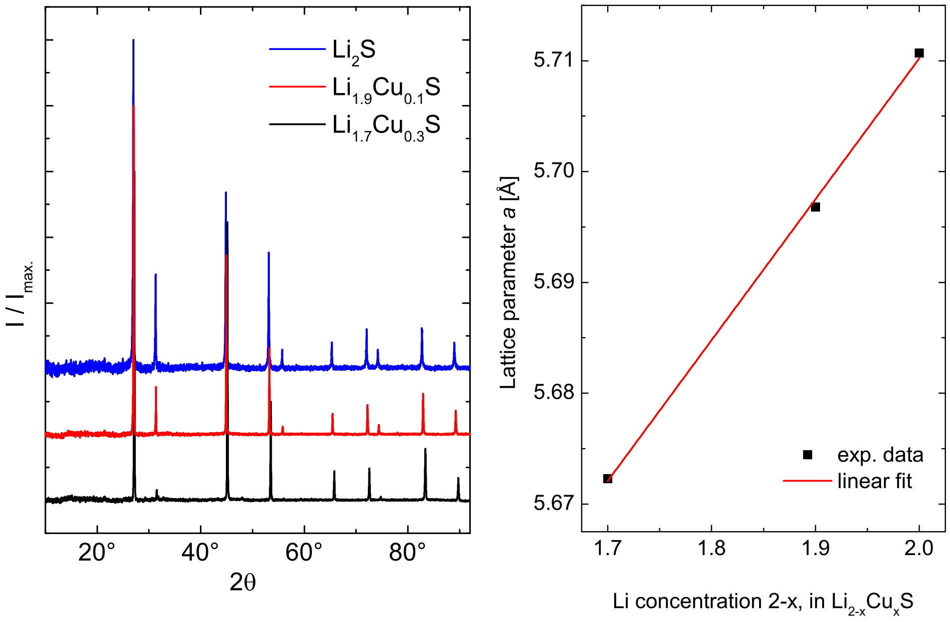

Figure 10.6: The left panels show the XRD pattern of $Li_{1.7}Cu_{0.3}S$, $Li_{1.9}Cu_{0.1}S$ and Li_2S. The right panel depicts the lattice constant a versus the Lithium content in $Li_{2-x}Cu_xS$.

Table 10.7: Atomic coordinates for $Li_{2-x}Cu_xS$ with the occupation factor: (a) of 0.3 for Cu in $Li_{1.7}Cu_{0.3}S_{\approx 1}$ and 0.1 in $Li_{1.9}Cu_{0.1}S_{\approx 1}$, respectively and (b) of 0.7 for Li in $Li_{1.7}Cu_{0.3}S_{\approx 1}$ and 0.9 in $Li_{1.9}Cu_{0.1}S_{\approx 1}$, respectively.

Atom	Wyckoff symbol	S.O.F.	x	y	z
Li1	$4b$	1	1/2	1/2	1/2
Cu2	$4a$	0.3, 0.1	0	0	0
Li2	$4a$	0.7, 0.9	0	0	0
S3	$4c$	1	1/4	1/4	1/4

10.4 Theoretical calculations

In order to gain more insight into the electronic structure of $Li_{1.1}Cu_{0.9}S$ and cubic $Li_{1.7}Cu_{0.3}S$ and $Li_{1.9}Cu_{0.1}S$, we have carried out density functional theory (DFT) calculations by employing the fully-relativistic Korringa-Kohn-Rostoker (KKR) Green's function method, as implemented in the SPR-KKR package [47]. For considering the disorder due to the random occupation of the atomic sites in $Li_{1.1}Cu_{0.9}S$, we have used the single-site coherent potential approximation (CPA) [48, 49], which is a rather efficient mean-field technique. The electronic exchange and correlation was treated within the PBE [46] version of the generalized-gradient approximation (GGA). In the calculations we used the experimental atomic structure and site occupations. Using this setup, we computed the Bloch-spectral function (BSF) of $Li_{1.1}Cu_{0.9}S$ shown in Figure 10.7. The data obtained show that $Li_{1.1}Cu_{0.9}S$ is a direct band-gap semiconductor with an energy band gap (at Γ point) of 1.95 eV, and the indirect energy band gap in the vicinity of the R point is 2.55 eV. This is in very good agreement with the 2.0 and 2.5 eV optical direct and indirect band gaps measured for the radio-frequency sputter deposited $Li_{\sim 1}CuS$ thin film on quartz glass [1]. The calculated BSF indicates that because of the (Li,Cu) disorder in $Li_{1.1}Cu_{0.9}S$, the bands close to the top of the valence band were rather flat, showing little dispersion. In the case of $Li_{1.7}Cu_{0.3}S$ and $Li_{1.9}Cu_{0.1}S$, both are direct band-gaps semiconductors. The energy band-gap increase at Γ point from 2.4 eV to 3 eV (see Figure 10.7).

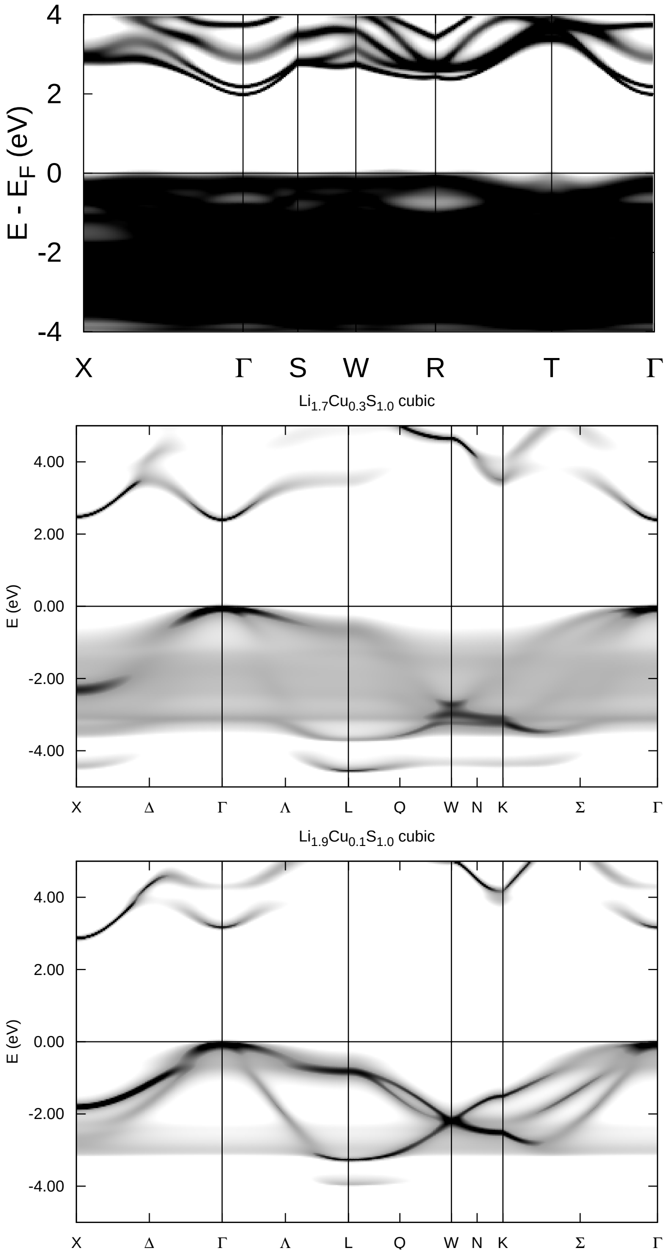

Figure 10.7: Top, middle and bottom panels show the band structure of $Li_{1.1}Cu_{0.9}S$, $Li_{1.7}Cu_{0.3}S$, and $Li_{1.9}Cu_{0.1}S$ respectively.

10.5 NMR measurements

The atomic environment of the Lithium atoms of yellow $Li_{1.1}Cu_{0.9}S$ was investigated by means of ^{7}Li NMR using powder samples. As a standard compound Li_2S was chosen. The crystal structure and also the Li environment for Li_2S is well known. The compound crystallizes in a cubic crystal system, $Fm\overline{3}m$ (No. 225). The Lithium atoms occupy the $8c$ position in ($\frac{1}{4}$,$\frac{1}{4}$,$\frac{1}{4}$) and the S atoms occupy the $4a$ position in (0,0,0). The Li environment has been elsewhere also investigated by NMR measurements. The spectra show the existence of one peak, which is in very good agreement with the crystallographic data, where Lithium is occupying just one crystallographic site [134].

The NMR line itself provides information about i) the anisotropy of the nuclear site and ii) the number of possible NMR active sites in the structure.

The ^{7}Li solid-state NMR spectrum of polycrystalline $Li_{1.1}Cu_{0.9}S$, as shown in Figure 10.8, can be fitted by two well-separated lines with a sizeable chemical shift anisotropy, typical for a tetragonal symmetry. The two lines indicate two different types of atomic environment for the Li atoms. The peak with a lower intensity can be assigned to the linearly coordinated Li3 species, and the large peak can be assigned to Li2 and Li4, which are both tetrahedrally surrounded by S. This assignment is based on the NMR intensity ratio, which should be equal to the ratio of Li atoms in linear and tetrahedral coordination modes. The intensity ratio, 17, was slightly larger than the number ratio, 10. However, one should keep in mind that the error of the intensity ratio is expected to be large due to the small intensity contribution of the Li3 line. Notably, ^{7}Li has nuclear spin $\frac{3}{2}$ which can result in a quadrupolar interaction if the crystal structure is noncubic. However, no satellites were detected, which is probably caused by too small a quadrupolar interaction, forcing the satellites to merge with the central transition.

Figure 10.8 shows spectra for Li_2S and $Li_{1.1}Cu_{0.9}S$. The x-axis represents the normalized frequency (ν is divided by ν_{max}). ν_{max} varies slightly because of a different residual NMR shift component for the different compounds. The advantage of such a plotting is that line width and line analyze is easier to perform.

The spectrum for Li_2S can be fitted by one symmetric Gaussian line which indicates that the local field is isotropic in nature, which is expected for a cubic crystal structure and with one Li site.

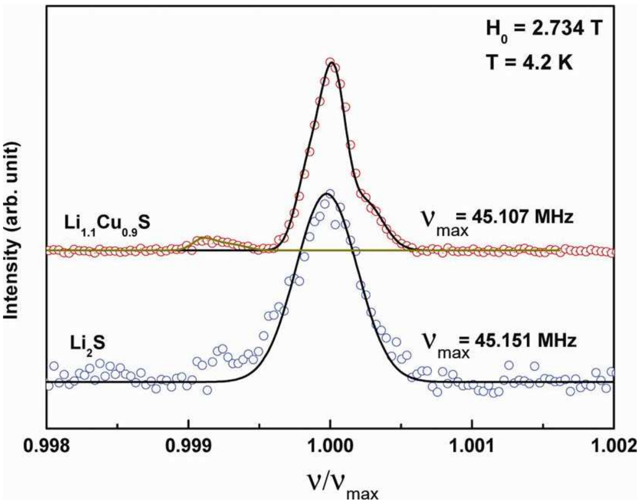

Figure 10.8: ^{7}Li-NMR spectra $Li_{1.1}Cu_{0.9}S$ and Li_2S.

10.6 Applications of LiCuS and LiZnP

The text of this chapter contain original text passages identical with the following publication:

D. Kieven, A. Grimm, A. Beleanu, C.G.F. Blum, J. Schmidt, T. Rissom, I. Lauermann, T. Gruhn, C. Felser, R. Klenk
Preparation and properties of RF-sputtered half-Heusler films with regard to usage in solar cell devices
Thin Solid Films, 519, 6, **(2011)**, 1866

During the last years, there has been a clear trend toward multinary compounds, providing a wider range of electrical, optical, and chemical properties. So, the development and optimization of optoelectronic devices depends on the availability of suitable semiconductor materials. Starting from silicon and binary semiconductors to ternary or higher multinary materials, the number of possible compounds grows strongly, providing a great variety of material properties together with a growing difficulty to choose the right one for the respective application [23, 56].

A very suitable class of ternary materials are half-Heusler compounds with composition XYZ. The cationic X^{n+} fills the gaps of a covalently bound (YZ)$^{n-}$ sublattice. If the elements X, Y, and Z have o total number of eight valence electrons they form a stable ground-state structure and are likely to be semiconductors. Therefore, the class of eight-electron half-Heusler compounds includes a large number of semiconductors, whose band gaps vary in a wide range [23, 135]. Recent a set of half-Heusler compounds were investigated with the help of all-electron density-functional theory [23, 136]. One of the reason of these investigations is to preselect compounds as candidate materials for specific optoelectronic applications like for finding new buffer layer materials for thin film solar cells based on chalcopyrite absorber layer such as Cu(InGa)S_2.

Copper indium gallium diselenide (CIGS)-based solar cells are presently one of the best candidates for a new generation of large-scale and low-cost photovoltaic devices. Highly efficient cells (18.8%) are obtained [137] and they start to be produced at the industrial level. The basic constitution of the solar cell [138](Figure 10.9) is given by a frontal electrode layer, a light-absorbing layer (ZnO), a buffer layer (usually CdS), a absorber layer (the CIGS materials), a back layer (Molybden) on a substrate (glass). The photoelectric conversion (p-n junction) is formed between the buffer layer (n-type semiconductor) and the absorber layer (p-type semiconductor).

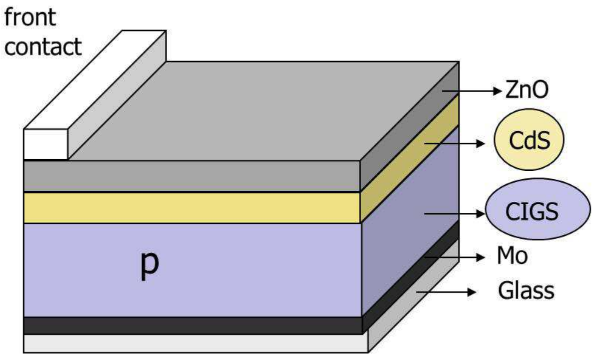

Figure 10.9: The basic constitution of the chalcopyrite-based solar cell with the light-absorbing layer of ZnO, the buffer layer (CdS), the absorber layer (the CIGS materials), the back layer (Molybden) and the glass substrate.

The demand for new buffer layer material in this case is necessary because CdS, which is used in conventional chalcopyrite-based thin film solar cells, is very toxic and harmful for the environment. The role of the buffer layer is to increase the performance of the device. A suitable buffer layer material must fulfill some criteria: its crystal structure has to match the structure of the absorber layer, the band gap must be suitably large (more than 2 eV) and the absorber and the Fermi-level at the interface should be close to the conduction band in order to minimize the interface recombination [139].

This chapter reports on the synthesis of Li-Cu-S and Li-Zn-P polycrystalline starting materials, which will be used for the preparation of LiCuS and LiZnP thin films by radio-frequency (RF) sputterig deposition method. The stability of these films under vacuum and atmospheric conditions has been investigated by photon electron spectroscopy. The optical band gap of these films has been analyzed. The valence band offset at the LiCuS, LiZnP/Cu(In,Ga)Se_2 has been estimated. The Lithium diffusion at a LiCuS/Zn(Mg)O interface have been investigated.

All the mentioned investigations performed on these materials, have been carried out by Davied Kieven, at the Helmholtz Center in Berlin as a collaboration of the CIGS Projekt, BMU (0327665[A-E]).

In order to obain thin films of LiCuS and LiZnP, a three inch target of these materials has to be hot sintered. The method used for the deposition of these compounds is the radio-frequency method. For the preparation of these two compounds, 200 g of material was needed.

The ternary polycrystalline LiCuS samples were prepared by ball milling, using stochiometric amounts of Li_2S and Cu_2S. The cylindrical capped containers were filled under inert gas atmosphere in order to avoid any oxygen contamination. For a better grinding and homogeneity ceramic grinding media was used. After 10 h grinding, ocher brownish powder was obtained. Eight quarz tubes were evacuated at 10^{-3} mbar and cleaned at 600°C. Each tube was filled with 25 g powder and sealed under vacuum. The obtained 200g powder sample was hot sintered using the spark plasma sintering (SPS) method under high pressure at a nominal temperature of 870 K and under 22 MPa. Yellow ocher thin films were obtained by radio frequency sputtering deposition at room temperature in ultra high vacuum sputter chamber into square inch quartz glass(Figure 10.10).

LiZnP was synthesized by solid state reaction using stoichiometric amounts of lithium ingots, zinc and red phosphorus, both in powder form. Tantalum crucibles sealed by arc melting under argon atmosphere were used as containers for the preparation of LiZnP. Each tantalum crucible contained 10 g of stoichiometric weighed LiZnP. The charged crucibles were sealed in quartz tubes (25 mm diameter, Figure 10.11). Dark-red powder was obtained after heating the samples at 900 °C for 96 h in a muffle type furnace, with a heat rate of 1 °C/min. All the samples were investigated by X-ray diffraction, which reveals single homogenous phase (not shown here).

The ternary polycrystalline LiZnP samples were hot sintered by a spark plasma sintering method at 870 K and 22 MPa. Red thin films (Figure 10.12) were prepared by the radio frequency deposition method in the same conditions like the LiCuS thin films.

Figure 10.10: LiCuS thin film obtained by RF sputtering method

Figure 10.11: Sealed tantalum tube in quartz tube used for the synthesis of LiZnP.

LiZnP (described in Chapter 7) belong to the so called Nowotny-Juza compounds. Nowotny-Juza compounds $A^{I}B^{II}C^{V}$ are based on three main group elements (A, B and C) and exhibit the same crystalline structure ($C1_b$) as the XYZ Heusler compounds, where X and Y are usually transitions metals and Z is a main group element. They can be viewed as zinc-blende III-V compounds in which the III

Figure 10.12: LiZnP thin films obtained by the RF sputtering method

column has been "disproportionated" into A^{I}+B^{II} atoms [6].

The structure of LiCuS was at that time unknown so far. The teoretical calculations made by Gruhn et al. [56] were performed assuming that LiCuS crystallizes similar to LiZnP in the Half-Heusler structure type. The XRD powder pattern of LiCuS shows however that LiCuS does not crystallize in the cubic structure, but in the orthorhombic one, described in Chapter 9.3.1.

The correct stoichiometry of the deposited thin-films, LiCuS and LiZnP, was investigated by means of X-ray and ultraviolet photo-electron spectroscopy. For optical analysis, transmission and reflection as a function of the wavelength has been measured. The absorption coefficient α was obtained in first approximation from the Bougouer-Lambert Law using the measured transmission, reflection and the film thickness [1]. Due to the high positive conduction band offset to Cu(In,Ga)Se_2 and the low chemical stability under atmospheric conditions the investigated compounds cannot serve as a buffer layer material in chalcopyrite-based thin film solar cell. However, with adequate encapsulations these compounds could be interesting for other optoelectronic devices.

10.7 Summary

An intermediate phase with the composition $Li_{1.1}Cu_{0.9}S$ in the Li-Cu-S system was discovered and its crystal structure was solved. The crystal structure of the yellow polycrystalline $Li_{1.1}Cu_{0.9}S$ forms off-stoichiometric with no perceptible homogeneity range. Cu and Li atoms occupy mixed randomly all metal sites, which are linear and tetrahedral coordinated by S atoms. The crystal structure is closely related to that of Li_2S. The main features of the crystal structure may be derived by moving part of the Li chains in such a way that the atoms change their environment form tetrahedral to linear coordination by S. These sites show a strong site occupation preference for Cu. $Li_{1.1}Cu_{0.9}S$ is extremely moisture and air sensitive. It is direct band gap semiconductor with a band gap of 1.95 eV, thus causing the yellow color. There is strong evidence that at slightly lower Li content a further intermediate phase of black color forms in the CuS/Li conversion process making the process even more complex.

Samples of $Li_{2-x}Cu_xS$ compositions, with x = 0.1, 0.3, 0.5, 0.7, 0.9 and 1, have been synthesized. Powder XRD measurements on this series with x = 1, 0.9, 0.7 and 0.5 reveal mixtures of three different phases: orthorhombic (belonging to yellow $Li_{1.1}Cu_{0.9}S$), cubic and a unknown phase, which was not identified until now. At the composition with x = 0.3 and x = 0.1, $Li_{2-x}Cu_xS$ crystallize in the cubic CaF_2-

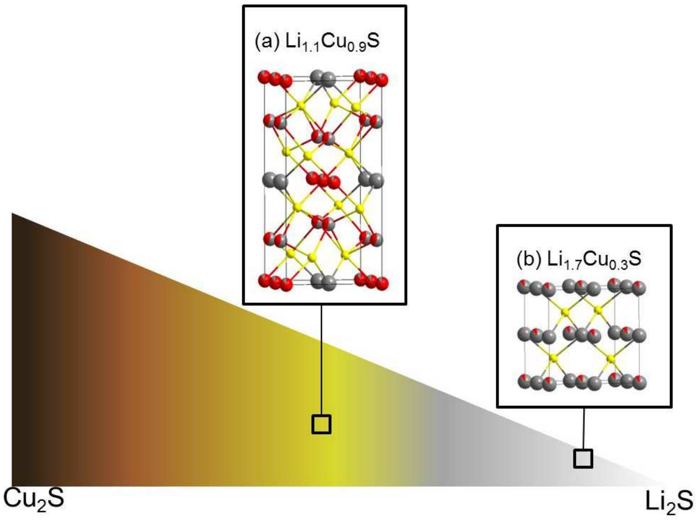

Figure 10.13: The color of mixtures with $Li_{2-x}Cu_xS$ composition. Cu_2S is black, the unknown $Li_{0.8}Cu_{1.2}S$ is black, $Li_{1.1}Cu_{0.9}S$ is yellow, $Li_{2-x}Cu_xS$ ($0 < x < 0.3$) is grey and Li_2S is white.

structure type, similar to Li_2S structure. Figure 10.13 displays a color diagram for mixtures of Cu_2S with the black unknown phase, mixtures of the black unknown phase with yellow $Li_{1.1}Cu_{0.9}$ and mixtures of $Li_{1.1}Cu_{0.9}$ and $Li_{2-x}Cu_x$.

11 Conclusion

One of the main goals of this thesis was the synthesis of Li-based ternary Half-Heusler compounds and other related Li-based materials, to serve as materials for use in technological applications, such as optoelectronics, spintronics and anode materials. Therefore, a very wide range of characterization methods have been used in order to learn about their chemical and physical properties and to acknowledge their potential for various applications.

In Chapter 4 all the experimental methods used in order to characterize and to investigate the samples synthesized in this work are described in detail. In order to gain further insights into the electronic structure and magnetism, density functional theory calculations have been performed and the results have been compared to optical, ellipsometry and magnetic measurements. Chapter 5 reports the theoretical methods and the underlying approximations applied in the calculations used as theoretical support in combination with the experimental data.

Polycrystalline samples of LiMgZ (Z = P, As, Sb) have been synthesized and systematically investigated in Chapter 6 in order to study their potential as opto-electronics and anode materials for lithium batteries. All samples crystallize in a cubic structure with $C1_b$ structure type, space group $F\overline{4}3m$ (No. 216). The Li mobility, an important requirement for these kind of applications was proved by neutron diffraction measurements and ^{7}Li static NMR measurements. Based on this study we have arrived to two major conclusions. First, a distortion of the structure was discovered caused by a possible modulation of the Li substructure. Secondly, a clear trend of the ^{7}Li NMR spectra was found. The peak widths decrease with increasing temperature, this feature be directly related with the increased Li ion mobility. UV-VIS measurements on LiMgZ (Z = P, As, Sb) indicate a wide direct band-gap of these compounds, with E_g of $\approx$ 2.3, 1.8 and 0.9 eV, respectively. In accordance with optical measurements, the resistivity measurements using the direct current method show also that all materials in this series exhibit a semiconducting behavior.

In Chapter 7 the $\mathrm{LiZn}_{1-x}\mathrm{Mn}_x\mathrm{P}$ (with $0 < x < 0.35$) series was investigated, to study if these materials are suitable materials for spintronic applications with respect as diluted magnetic semiconductors. Samples belonging to this class with $0 < x < 0.35$ have been synthesized and structurally characterized by means of

PXRD measurements. Samples with a Mn-content below x = 0.12 crystallize in the cubic Half-Heusler structure. Optical measurements show that all samples with a Mn-content below x = 0.10 show a semiconducting behavior. A decrease of the band gap depending on the Mn concentration, i.e. , from LiZnP (1.80 eV) to the doped $LiZn_{0.90}Mn_{0.10}P$ (1.18 eV), is observed. Magnetic measurements exhibit a paramagnetic Curie Weiss behavior with negative Weiss constant, which leads to antiferromagnetic interaction.The investigated compounds $LiZn_{1-x}Mn_xP$ with x = 0.04, 0.08 and 0.10, are not suitable as diluted magnetic semiconductors based on these results.

LiMnAs and LaOMnAs have been investigated in Chapter 8 in detail, as possible candidates for spintronics, due to their band gap and high magnetic moment per Mn atom. These compounds were synthesized and structurally characterized by different powder diffraction techniques. Both materials crystallize in a tetragonal crystal structure. In the case of LiMnAs, a phase transition from the tetragonal to the cubic Half-Heusler structure was discovered. LiMnAs exhibits a magnetic phase transition with a Néel temperature of 374 K, and a structural transition from the tetragonal to the cubic phase at 768 K. Resistivity measurements reveal, that both LiMnAs and LaOMnAs show a variation in resistivity with more than five orders of magnitude, this makes them particularly suitable for use in future electronic devices. In order to investigate the environment and the valence state of the Mn atoms, EXAFS and XANES measurements have been performed. These indicate the oxidation state of Mn to be 1.6. This is in agreement with the concept of localized moments on Mn and explains the close relationship between the cubic and tetragonal phase and the connection between Mn and rare-earth ions in tetrahedrally coordinated structures. Ab-initio density functional theory calculations were combined with the experimental results in order to discuss the electronic and magnetic structure.

In Chapter 9 a new intermediate phase $Li_{1.1}Cu_{0.9}S$ is reported, which forms in the electrochemical conversion reaction of CuS with Li. This is a potential environment-friendly battery and solar cell material. A yellow polycrystalline material was obtained by reducing CuS with Li metal according to the following chemical reaction: $CuS + 1.1\ Li = Li_{1.10(5)}Cu_{0.90}S + 0.1\ Cu$. The inductively coupled plasma optical emission spectrometry chemical analysis show a composition of $Li_{1.17(3)}Cu_{1.07(3)}S$ for the bulk sample. The compound crystallizes in a orthorhombic crystal structure with a new crystal structure type in the space group *Ibam* (No. 72) with a = 5.632(1) Å, b = 11.216(2) Å, and c = 5.9982(1) Å at room temperature. The crystal structure of the sample was solved by a combination of neutron powder diffraction data at 4 and 293 K, X-ray diffraction data, and ^7Li solid-state NMR analysis. Cu and Li atoms are randomly mixed on all metal sites, which are linear and tetrahedral coordinated by S atoms. The crystal structure is closely related to that of Li_2S.

The main feature of the crystal structure may be derived by moving part of the Li chains in such a way that the atoms change their environment from tetrahedral to linear coordination by S. These sites show a strong site occupation preference towards Cu. Density functional theory calculations reveal that this compound is a direct band-gap semiconductor with a band-gap of 1.95 eV, thus causing the yellow color. It has also been observed that there is strong evidence that at slightly lower Li content a new intermediate phase of black color forms in the CuS/Li conversion process making the process even more complex. Samples of $Li_{2-x}Cu_xS$ composition, with x = 0.1, 0.3, 0.5, 0.7, 0.9 and 1, has been synthesized, and by powder XRD measurements structurally investigated. The samples with x = 1, 0.9, 0.7 and 0.5 reveal a mixture of three different phases: orthorhombic (belonging to the yellow $Li_{1.1}Cu_{0.9}S$), cubic (like Li_2S) and a unknown phase, which was not identified so far. $Li_{1.7}Cu_{0.3}S$ and $Li_{1.9}Cu_{0.1}S$ crystallize in the anti-CaF_2 structure. Thus, it was shown that pure Li_2S can dissolve up to x ≈0.3 by replacing Cu. Theoretical calculations reveal that both are semiconductors with a band-gap of 2.4 and 3.0 eV, respectively.

12 List of abbreviations

a	Lattice Parameter
α	Linear absorption coefficient
C	Curie constant
χ	Magnetic susceptibility
χ_{lin}	Field independent paramagnetic susceptibility
CPA	Coherent Potential Approximation
DC	Direct current
DFT	Density functional theory
DOS	Density of States
E_a	Activation energy
E_g	Band gap energy
$\hat{\mathrm{e}}_{i,j}$	Unit vectors (directions of the local magnetization at sites i and j)
EXAFS	Extended X-Ray Absorption Fine Structure
fcc	Face-entered Cubic
FWHM	The full width at half maximum
H	Magnetic field
j	Total Angular Momentum
J_{ij}	Magnetic exchange coupling constants
GGA	Generalized Gradient Approximation
K	Kubelka-Munk absorption coefficient
KKR	Korringa-Kohn-Rostoker
k_B	Boltzmann's constant ($1.38062 \cdot 10^{-23}$ J/K, J = V·A·s)
λ	Wavelength
$L(H)$	Langevin function
M	Magnetization
μ_0	Permeability of the free space ($1.2566 \cdot 10^{-6}$ V·s/A·m)
N	Number of the magnetic atoms per unit volume
NMR	nuclear magnetic resonance spectroscopy
PAW	Projector-augmented wave
PBE	Perdew-Burke-Enzerhof
PTFE	Polytetrafluoroethylene
R_∞	Diffuse reflectance for an infinitely thick sample
RT	Room Temperature
S	Kubelka-Munk scattering coefficient
SQUID	Superconducting Quantum Interference Device

SPR-KKR	Spin Polarized Korringa-Kohn-Rostoker
$h\nu$	Photon energy
μ_B	Bohr Magneton
$\rho(T)$	Electric Resistivity
σ	Electrical Conductivity
θ	Weiss constant
UV-VIS-NIR	Ultraviolet-Visible Near Infrared Spectroscopy
VT	Variable temperature
XANES	X-ray Absorption Near Edge Structure
PXRD	Powder X-ray Diffraction

List of Figures

List of Tables

Bibliography

[1] D. Kieven, A. Grimm, A. Beleanu, C. G. F. Blum, J. Schmidt, T. Rissom, I. Lauermann, T. Gruhn, C. Felser, and R. Klenk. *Thin Solid Films*, 519:1866, 2011.

[2] F. Heusler. *Verh. DPG*, 5:219, 1903.

[3] F. Heusler, W. Starck, and E. Haupt. *Verh. DPG*, 5:220, 1903.

[4] D. Bende, Y. Grin, and F. R. Wagner. *Covalence and Ionicity in MgAgAs-type compounds.* submitted to Chemistry - A European Journal, 2014.

[5] E. Zintl. *Angewandte Chemie*, 52:1, 1939.

[6] E. Zintl and W. Dullenkopf. *Z. Phys. Chem.*, B16:183, 1932.

[7] E. Zintl and G. Brauer. *Z. phys. Chem.*, B20:245, 1933.

[8] S. C. Sevov. *Zintl Phases, in Intermetallic Compounds - Principles and Practice: Progress*, volume 3. John Wiley & Sons, Ltd, Chichester, UK., 2002.

[9] Pauling file binaries edition, version 1.

[10] W. Klemm and E. Busmann. *Z. Anorg. Allg. Chemie*, 319:297, 1963.

[11] S. M. Kauzlarich. *Chemistry, Structure, and Bonding of Zintl Phases.* VCH Publisher, New York, 1996.

[12] J. Jiang, M. M. Olmstead, S. M. Kauzlarich, H.-O. Lee, P. Klavins, and Z. Fisk. *Inorg. Chemistry*, 44:5322, 2005.

[13] J. Jiang and S. M. Kauzlarich. *Chem. Mater.*, 18:435, 2006.

[14] G. J. Miller, C. S. Lee, and W. Choe. *Structure and Bonding Around the Zintl Border, Inorganic Chemistry Highlights.* Wiley, Band 1, 2002.

[15] R. Nesper. *Progr. Solid St. Chem.*, 20:1, 1990.

[16] F. Casper, T. Graf, S. Chadov, B. Balke, and C. Felser. *Semicond. Sci. Technol.*, 27:063001, 2012.

[17] H. C. Kandpal, C. Felser, and R. Seshadri. *J. Phys. D: Appl. Phys.*, 39:776, 2006.

[18] D. Kieven, R. Klenk, S. Naghavi, C. Felser, and T. Gruhn. *Phys. Rev. B*, 81:075208, 2010.

[19] D. M. Wood, A. Zunger, and R. de Groot. *Phys.Rev.B*, 31:2570, 1985.

[20] R. Bacewicz and T. F. Ciszek. *Appl. Phys. Lett.*, 52:1150, 1998.

[21] K. Kuriyama and T. Katoh. *Phys. Rev. B.*, 37:7140, 1988.

[22] K. Kuriyama, Y. Takahashi, and K. Tomizawa. *Phys. Rev. B.*, 47:13861, 1993.

[23] T. Gruhn. *Phys. Rev. B*, 82:125210, 2010.

[24] S. Chen and Z. Ren. *Materials Today*, 16:387, 2013.

[25] F. G. Aliev, V. V. Kozyrkov, V. V. Moshchalkov, R. V. Scolozdra, and K. Durczewshi. *Z. Phys. B - Condensed Matter*, 80:353, 1990.

[26] I. Galanakis, P. H. Dederichs, and N. Papanikolaou. *Phys. Rev. B*, 66:134428, 2002.

[27] B. J. Yang, H. Li, T. Wu, W. Zhang, L. Chen, and J. Yang. *Adv. Funct. Mater.*, 18:2880, 2008.

[28] J. W. Simonson and S. J. Poon. *J. Phys.:Condens. Matter*, 20:255220, 2008.

[29] S. Sakurada and N. Shutoh. *Appl. Phys. Lett.*, 86:082015, 2005.

[30] S. Bhattacharya, A. L . Pope, R. T. IV. Littleton, T. M. Tritt, V. Ponnambalam, Y. Xia, and S. J. Poon. *Appl. Phys. Lett.*, 77:2476, 2000.

[31] S. Sakurada and N. Shutoh. *Appl. Phys. Lett.*, 86:082105, 2005.

[32] S. Ouardi, G. H. Fecher, B. Balke, M. Schwall, X. Kozina, Stryganyuk. G., C. Felser, E. Ikenaga, Y. Yamashita, S. Ueda, and K. Kobayashi. *App. Phys. Lett.*, 97:252113, 2010.

[33] S. Ouardi, G. H. Fecher, B. Balke, X. Kozina, Stryganyuk. G., C. Felser, Lowitzer S., D. Ködderitzsch, H. Ebert, and E. Ikenaga. *Phys. Rev. B*, 82:085108, 2010.

[34] H. Hohl, A. P. Ramirez, C. Goldmann, G. Ernst, B. Wölfing, and E. Bucher. *J. Phys.: Condens. Matter*, 11:1697, 1999.

[35] S. Katsuyama, H. Matsushima, and M. Ito. *J. Alloys. Compd.*, 385:232, 2004.

[36] C. Uher, J. Yang, S. Hu, D. T. Morelli, and G. P. Meisner. *Phys. rev. B*, 59:8615, 1999.

[37] V. Ponnambalam, B. Zhang, T. M. Tritt, and S. J. Poon. *J. Electron. Mater.*, 36:732, 2007.

[38] C. Felser, G. H. Fecher, and B. Balke. *Angew. Chem. Int. Ed.*, 46:668, 2007.

[39] J. Kübler. *Physica B*, 127:257, 1984.

[40] B. Balke, G. H. Fecher, J. Gloskovskii, J. Barth, K. Kroth, C. Felser, R. Robert, and A. Weidenkaff. *Phys. Rev. B*, 77:045209, 2008.

[41] M. Hoelzel, A. Senyshyn, N. Juenke, H. Boysen, W. Schmahl, and H. Fuess. *High-resolution neutron powder diffractometer SPODI at research reactor FRM II, Nuclear Instruments & Methods in Physics Research, Section A: Accelerators, Spectrometers, Detectors, and Associated Equipment*, 667:32, 2012.

[42] L. J. van der Pauw. *Philips Tech. Rev*, 20:220, 1958.

[43] L. J. van der Pauw. *Philips Res. Repts*, 13:1, 1958.

[44] G. Kresse and J. Furthmüller. *Phys. Rev. B*, 54:11169, 1996.

[45] G. Kresse and J. Furthmüller. *Comput. Mater. Sci.*, 6:15, 1996.

[46] J. P. Perdew, K. Burke, and M. Ernzerhof. *Phys. Rev. Lett.*, 77:3865–3868, 1996.

[47] H. Ebert, D. Ködderitzsch, and J. Minár. *Rep. Prog. Phys.*, 74:096501, 2011.

[48] P. Soven. *Phys. Rev.*, 156:809–813, 1967.

[49] W. H. Butler. *Phys. Rev. B*, 31:3260–3277, 1985.

[50] T. Jungwirth, V. Novak, X. Marti, M. Cukr, F. Maca, A. B. Shick, J. Mašek, P. Horodyska, P. Nemec, V. Holy, J. Zemek, P. Kuzel, I. Nemec, B. L. Gallagher, R. P. Campion, C. T. Foxon, and J. Wunderlich. *Phys. Rev. B*, 83:035321, 2011.

[51] R. Vidya, P. Ravindran, H. Fjellvåg, B. G. Svensson, E. Monakhov, M. Ganchenkova, and R. M. Nieminen. *Phys. Rev. B*, 83:045206, 2011.

[52] I. V. Rogozin and A. V. Marakhovskii. *J. Appl. Spectrosc.*, 72:6, 2005.

[53] D. S. Kyser and V. Rehn. *Phys. Rev. Lett.*, 40:1038, 1978.

[54] A. E. Carlsson, A. Zunger, and D. M. Wood. *Phys. Rev. B*, 32:1386, 1985.

[55] K. Kuriyama and K. Kushida. *Journal of Applied Physics*, 87:2303, 2000.

[56] D. Kieven, R. Klenk, S. Naghavi, C. Felser, and T. Gruhn. *Phys. Rev. B*, 81:075208, 2010.

[57] K. Kuriyama, K. Kushida, and R. Taguchi. *Solid State Commun.*, 108:429, 1998.

[58] F. Kalarasse, B. Bennecer, and A. Mellouki. *J. Phys.: Condens. Matter*, 18:7237, 2006.

[59] K. Kuriyama, Y. Yamashita, Y. Suzuki, K. Matsumoto, and K. Kushida. *AIP Conference Proceedings*, 1199:67–68, 2010.

[60] T. Graf, C. Felser, and S. S. P. Parkin. *Progress in Solid State Chemistry*, 39:1, 2011.

[61] J. Rodriguez-Carvajal. *Physica B*, 192:55, 1993.

[62] P. Kubelka and F. Munk. *Z. Tech. Physik.*, 1:593, 1931.

[63] J. Smith, editor. *Optical Properties of Condensed Matter and Applications.* Willey., 2006.

[64] R. Beterman and M. Müller-Wartmuth. *Z. Naturforsch.*, 53:863, 1998.

[65] R. Böhmerand, K. R. Jeffrey, and M. Vogel. *Progress in Nuclear Magn. Res. Spectr.*, 50:87, 2007.

[66] C. Kittel. *Introduction to Solid State Physics, 4th Edition.* Wiley, New York, 1973.

[67] A. H. Macdonald, P. Schiffer, and N. Samarth. *Nature Materials.*, 4, 2005.

[68] Z. Deng, C. Q. Jin, Q. Q. Liu, X. C. Wang, J. L. Zhu, S. M. Feng, L. C. Chen, R. C. Yu, C. Arguello, T. Goko, F. Ning, J. Zhang, Wang. Y., A. A. Aczel, T. Munsie, T. J. Williams, G. M. Luke, T. Kakeshita, S. Uchida, W. Higemoto, T. U. Ito, B. Gu, S. Maekawa, G. D. Morris, and Y. J. Uemura. *Nature Comm.*, 2(422):1–5, 2011.

[69] J. Mašek, J. Kudrnovský, F. Máca, B. L. Gallagher, R. P. Campion, D. H. Gregory, and T. Jungwirth. *Phys. Rev. Lett.*, 98:067202, 2007.

[70] H. Nowotny and K. Bachmayer. *Monatshefte für Chemie / Chemical Monthly.*, 80(4), 1949.

[71] R. Juza and F. Hund. *Z. Anorg. Chemie.*, 257, 1948.

[72] A. R. Denton and N. W. Ashcroft. *Phys. Rev. A*, 43:3161, 1991.

[73] I. Žutić, J. Fabian, and S. Das Sarma. *Rev. Mod. Phys.*, 76:323–410, 2004.

[74] T. Dietl, H. Ohno, F. Matsukura, J. Cibert, and D. Ferrand. *Science*, 287:1019, 2000.

[75] T. Jungwirth, J. Sinova, J. Mašek, J. Kučera, and A. H. MacDonald. *Rev. Mod. Phys.*, 78:809, 2006.

[76] T. Jungwirth, V. Novak, X. Marti, M. Cukr, F. Maca, A. B. Shick, J. Mašek, P. Horodyska, P. Nemec, V. Holy, J. Zemek, P. Kuzel, I. Nemec, B. L. Gallagher, R. P. Campion, C. T. Foxon, and J. Wunderlich. *Phys. Rev. B*, 83:035321, 2011.

[77] V. Novak, M. Cukr, Z. Soban, T. Jungwirth, X. Marti, V. Holy, P. Horodyska, and P. Nemec. *J. Crys. Growth*, 323:348, 2011.

[78] A. P. Wijnheijmer, X. Marti, V. Holy, M. Cukr, V. Novak, T. Jungwirth, and P. M. Koenraad. *Appl. Phys. Lett.*, 100:112107, 2012.

[79] F. Máca, J. Mašek, O. Stelmakhovych, X. Martí, H. Reichlová, K. Uhlířová, P. Beran, P. Wadley, V. Novák, and T. Jungwirth. *J. Magn. Magn. Materials*, 324(8):1606–1612, 2012.

[80] J. Wunderlich, T. Jungwirth, B. Kaestner, A. C. Irvine, A. B. Shick, N. Stone, K. Y. Wang, U. Rana, A. D. Giddings, C. T. Foxon, R. P. Campion, D. A. Williams, and B. L. Gallagher. *Phys. Rev. Lett.*, 97:077201, 2006.

[81] J. H. Tapp, Z. Tang, B. Lv, K. Sasmal, B. Lorenz, P. C. W. Chu, and A. M. Guloy. *Phys. Rev. B*, 78:060505R, 2008.

[82] W. Bronger, P. Müller, R. Höppner, and H. U. Schuster. *Z. Anorg. Allg. Chem.*, 539:175, 1986.

[83] N. Emery, E.J. Wildman, J. M. S. Skakle, G. Giriat, R.I Smith, and A. C. Mclaughlin. *Chem. Comm.*, 46:6777, 2010.

[84] T. Graf, C. Felser, and S. S. P Parkin. *Prog. Solid. State Ch.*, 39:1, 2011.

[85] J. Kübler, A. R. Williams, and C. B. Sommers. *Phys. Rev. B*, 28:1745, 1983.

[86] F. Schucht, A. Dascoulidou, R. Müller, W. Jung, H.-U. Schuster, W. Bronger, and P. Müller. *Z. Anorg. Allg. Chem.*, 625:31, 1999.

[87] R. Müller, M. Kuckel, H. U. Schuster, P. Müller, and W. Bronger. *J. Alloy. Compd.*, 176:167, 1991.

[88] M. J. Otto, H. Feil, R. A. M. van Woerden, J. Wijngaard, P. J. Van Der Valk, C. F. van Bruggen, and C. Haas. *J. Magn. Magn. Materials*, 70:33, 1987.

[89] N. Emery, E. J. Wildman, J. M. S. Skakle, A. C. Mclaughlin, R. I Smith, and A. N. Fitch. *Phys. Rev. B*, 83:144429, 2011.

[90] V. A. Dinh, K. Sato, and H. Katayama-Yoshida. *J. Phys. Soc. Japan*, 77(1):014705, 2008.

[91] P. P. J. Van Engelen, D. B. De Mooij, J. H. Wijngaard, and K. H. J. Buschow. *J. Magn. Magn. Materials*, 130:247, 1994.

[92] F. Ishikawa, K. Koyama, K. Watanabe, T. Asano, and H. Wada. *J. Phys. Soc. Japan*, 75:084604–1, 2006.

[93] S. Haneda, N. Kazama, Y. Yamaguchi, and H. Watanabe. *J. Phys. Soc. Japan*, 42:1201, 1977.

[94] J. W. Simonson, Z. P. Yin, M. Pezzoli, J. Guo, J. Liu, K. Post, A. Efimenko, N. Hollmann, Z. Hu, H.-J. Lin, C.-T. Chen, C. Marques, V. Leyva, G. Smith, J. W. Lynn, L. L. Sun, G. Kotliar, D. N. Basov, L. H. Tjeng, and M. C. Aronson. *Proc. Natl. Acad. Sci.*, 109:10751, 2012.

[95] G. Achenbach and H. U. Schuster. *Z. Anorg. Allg. Chem.*, 9:475, 1981.

[96] V. Petricek, M. Dusek, and L. Palatinus. *Jana 2006. The crystallographic computing system.* Institut of Physics, Praha, Czech Republic, 2006.

[97] I. E. Dzyaloshinskii. *J. Chem. Solids*, 4:241, 1958.

[98] T. Moriya. *Phys. Rev. Lett.*, 4:228, 1960.

[99] F. Ishikawa, K. Koyama, K. Watanabe, T. Asano, and H. Wada. *J. Phys. Soc. Japan*, 75:084604, 2006.

[100] D. C. Konigsberger and R. Prins, editors. *X-Ray Absorption: Principles, applications and techniques of EXAFS, SEXAFS and XANES in Chemical Analysis*, volume 92. Wiley, New York, 1988.

[101] M. Newville. *J. Synchr. Rad.*, 8:322, 2001.

[102] S. I. Zabinsky, J. J. Rehr, A. Ankudinkov, R. C. Albers, and M. J. Eller. *Phys. Rev. B*, 52:2995, 1995.

[103] J. Wong, F. W. Lytle, R. P. Messmev, and D. H. Maylotte. *Phys. Rev. B*, 30:5596, 1984.

[104] J. A. Woollam and Co. *Spectroscopic Ellipsometry Data Acquisition and Analysis Software WVASE32®.* http://www.jawoollam.com.

[105] A. V. Boris, N. N. Kovalena, S. S. A Seo, J. S. Kim, P. Popovich, Y. Matiks, R. K. Kremer, and B. Keimer. *Phys. Rev. Lett.*, 102:027001, 2009.

[106] Y. Singh, M. A. Green, Q. Huang, A. Kreyssig, R. J. McQueeney, D. C. Johnston, and A.I. Goldman. *Phys. Rev. B*, 80:100403, 2009.

[107] B. G. Park, J. Wunderlich, X. Martí, V. Holý, Y. Kurosaki, M. Yamada, H. Yamamoto, A. Nishide, J. Hayakawa, H. Takahashi, A. B. Shick, and T. Jungwirth. *Nature Mat.*, 10:347, 2011.

[108] P. G. Bruce. *Chem. Commun.*, 19:1817, 1997.

[109] D. Guyomard and J. M. Tarascon. *Solid State Ionics*, 69:222, 1994.

[110] R. Koksbang, J. Barker, H. Shi, and M. Y. Saidi. *Solid State Ionics*, 84:1, 1996.

[111] M. Winter, J. O. Besenhard, M. E. Spahr, and P. Novak. *Adv. Mater.*, 10:725, 1998.

[112] J. M. Tarascon and M. Armand. *Nature*, 414:359, 2001.

[113] B. Ammundsen and J. Paulsen. *Adv. Mater.*, 13:943, 2001.

[114] M. Armand and J.-M. Tarascon. *Nature*, 451:652, 2008.

[115] F. Yongzhu and A. Manthiram. *Electrochimica Acta*, 109:716, 2013.

[116] F. Bonino, M. Lazzari, B. Rivolta, and B. Scrosati. *Journal of the Electrochemical Society*, 131:1498, 1984.

[117] H. Lee, S. W. Yoon, E. J. Kim, and J. Park. *J. Nano Lett.*, 7:778–784, 2007.

[118] N. S. Xu and S. E. Huq. *Mater Sci. Eng. R*, 48:47–189, 2005.

[119] J. Chen, S. Z. Deng, N. S. Xu, S. H. Wang, X. G. Wen, S. H. Yang, C. L. Yang, J. N. Wang, and W. K. Ge. *Appl. Phys. Lett.*, 80:3620–3622, 2002.

[120] K. Okamoto and S. Kawai. *Jpn. J. Appl. Phys.*, 12:1130, 1973.

[121] A. Etienne. *J. Electrochem. Soc.*, 117:870, 1970.

[122] N. Margalit, editor. *Proceedings of the Symposium on Battery Design and Optimization of the Electrochemical Society.* Princeton, New Jersey, 1979.

[123] N. Yamakawa, M. Jiang, and C. P. Grey. *Chem. Mater.*, 21:3162, 2009.

[124] A. Attewell and P. Tattershall, editors. *Proceedings of the 29th Power Sources Symposium of the Electrochemical Society.* Pennington, New Jersey, 1980.

[125] L. W. Langrish, editor. *Proceedings of the 29th Power Sources Symposium of the PSC Publication Committee.* Red Bank, New Jersey, 1969.

[126] D. Linden, N. Wilburn, and E. Brooks, editors. *Proceedings of the 8th International Power Sources Symposium, Paper No.20.* Brighton, 1972.

[127] R. J. Jasinski. *J. Electroanal. Chem. and Interf. Electrochem.*, 26:189–194, 1970.

[128] J. P. Gabano, V. L. Decheneaux, G. M. Gerbier, and J. Jammet. *J. Electrochem. Soc.*, 119:459–461, 1972.

[129] A. J. Cuesta and D. D. Bump, editors. *Proceedings of the Symposia on Power Sources on Biomedical Implantable Applications and Ambient Temperature Lithium Batteries, The Electrochemical Society.* Princeton, New Jersey, 1980.

[130] A. M. Bredland, T. G. Messing, and J. W. Paulson, editors. *Proceedings of the 29th Power Sources Symposium of the Electrochemical Society.* Pennington, New Jersey, 1980.

[131] *Treor, implemented in the software package WINXPOW.* STOE & CIE GmbH, 2007.

[132] A. Altomare, C. Cuocci, C. Giacovazzo, A. Moliterni, R. Rizzi, N. Corriero, and A. Falcicchio. *J. Appl. Cryst.*, 46:131–1235, 2013.

[133] P. Villars and K. Cenzual. *Pearsons's Crystal Data–Crystal Structure Data Base for Inorganic Compounds.* ASM International, Materials Park, Ohio, USA, 2012-2013.

[134] C. Lin, L. Calvez, B. Bureau, H. Tao, M. Allix, Z. Hao, V. Seznec, X. Zhang, and X. Zhao. *Phys. Chem. Chem. Phys.*, 12:3780, 2010.

[135] H. Nowotny and K. Bachmayer. *Monatsch. Chem.*, 81:488, 1950.

[136] H. Mehnane, B. Bekkouche, S. Kacimi, A. Hallouche, M. Djermouni, and A. Zaoui. *Superlattices and Microstructures*, 51:772–784, 2012.

[137] M. A. Contreras, B. Egaas, K. Ramanathan, J. Hiltner, A. Swartzlander, F. Hasoon, and R. Noufi. *Progress in Photovoltaics: Research and Applications*, 7:311, 1999.

[138] A. Yamada, H. Tampo, K. Matsubara, S. Niki, K. Sakurai, S. Ishizuka, and K. Iwata. http://www.google.com/patents/us20050284518, 2005.

[139] J. Poortmans and V. Arkhipov, editors. *Thin Film Solar Cells: Fabrication, Characterization and Applications.* John Wiley & Sons Ltd, The Atrium, Southern Gate, Chichester, West Sussex, England, 2006.